

Published in final edited form as:

Astrophys J. 2016 November 20; 832(1): . doi:10.3847/0004-637X/832/1/12.

Analysis of the Herschel/HEXOS Spectral Survey Towards Orion South: A massive protostellar envelope with strong external irradiation

K. Tahani, R. Plume

Department of Physics & Astronomy, University of Calgary, Calgary, AB, Canada T2N 1N4

E. A. Bergin,

Department of Astronomy, University of Michigan, 500 Church Street, Ann Arbor, MI 48109, USA

V. Tolls¹, T. G. Phillips², E. Caux^{3,4}, S. Cabrit⁵, J. R. Goicoechea⁶, P. F. Goldsmith⁷, D. Johnstone⁸, D. C. Lis^{5,2}, L. Pagani⁵, K. M. Menten⁹, H. S. P. Müller¹⁰, V. Ossenkopf-Okada¹⁰, J. C. Pearson⁷, F. F. S. van der Tak^{11,12}

¹Harvard-Smithsonian Center for Astrophysics, 60 Garden Street, Cambridge, MA 02138, USA

²California Institute of Technology, Cahill Center for Astronomy and Astrophysics 301-17, Pasadena, CA 91125, USA ³Université de Toulouse, UPS-OMP, IRAP, 31028 Toulouse, France

⁴CNRS, IRAP, 9 Av. Colonel Roche, BP 44346, 31028 Toulouse Cedex 4, France ⁵LERMA, Observatoire de Paris, PSL Research University, CNRS, Sorbonne Universités, UPMC Univ. Paris 06, F-75014, Paris, France ⁶Instituto de Ciencia de Materiales de Madrid (ICMM-CSIC). Sor Juana Ines de la Cruz 3, E-28049 Cantoblanco, Madrid, Spain ⁷Jet Propulsion Laboratory, Caltech, Pasadena, CA 91109, USA ⁸National Research Council Canada, Herzberg Institute of Astrophysics, 5071 West Saanich Road, Victoria, BC V9E 2E7, Canada ⁹Max-Planck-Institut für Radioastronomie, Auf dem Hügel 69, 53121 Bonn, Germany ¹⁰I. Physikalisches Institut, Universität zu Köln, Zùlpicher Str. 77, 50937 Köln, Germany ¹¹SRON Netherlands Institute for Space Research, PO Box 800, 9700 AV, Groningen, The Netherlands ¹²Kapteyn Astronomical Institute, Groningen, The Netherlands

Abstract

We present results from a comprehensive submillimeter spectral survey toward the source Orion South, based on data obtained with the HIFI instrument aboard the *Herschel Space Observatory*, covering the frequency range 480 to 1900 GHz. We detect 685 spectral lines with $S/N > 3\sigma$, originating from 52 different molecular and atomic species. We model each of the detected species assuming conditions of Local Thermodynamic Equilibrium. This analysis provides an estimate of the physical conditions of Orion South (column density, temperature, source size, & V_{LSR}). We find evidence for three different cloud components: a cool ($T_{ex} \sim 20 - 40$ K), spatially extended ($> 60''$), and quiescent ($V_{FWHM} \sim 4 \text{ km s}^{-1}$) component; a warmer ($T_{ex} \sim 80 - 100$ K), less

spatially extended ($\sim 30''$), and dynamic ($V_{FWHM} \sim 8 \text{ km s}^{-1}$) component, which is likely affected by embedded outflows; and a kinematically distinct region ($T_{ex} > 100 \text{ K}$; $V_{LSR} \sim 8 \text{ km s}^{-1}$), dominated by emission from species which trace ultraviolet irradiation, likely at the surface of the cloud. We find little evidence for the existence of a chemically distinct “hot core” component, likely due to the small filling factor of the hot core or hot cores within the *Herschel* beam. We find that the chemical composition of the gas in the cooler, quiescent component of Orion South more closely resembles that of the quiescent ridge in Orion-KL. The gas in the warmer, dynamic component, however, more closely resembles that of the Compact Ridge and Plateau regions of Orion-KL, suggesting that higher temperatures and shocks also have an influence on the overall chemistry of Orion South.

Subject headings

ISM: abundances; ISM: molecules; ISM: lines and bands; ISM: kinematics and dynamics; ISM: individual (Orion South)

1 Introduction

To date, about 200 different molecular species have been detected in the interstellar medium (Menten & Wyrowski 2011)¹. However, our understanding of the total molecular inventory of individual sources is poor, since few sources have been systematically surveyed in any frequency band due to the large amount of observing time required to perform unbiased spectral surveys (e.g. Blake et al. 1987; Schilke et al. 1997a; Nummelin et al. 1998; Schilke et al. 2001; Comito et al. 2005; Furlan et al. 2006; Tercero et al. 2010; Neill et al. 2014). Therefore, we do not truly understand the origin of the chemical complexity observed in interstellar space. Understanding this complexity is important to comprehend details of the formation of stars, planets and life.

Regardless of how complex chemistry arises in interstellar space, the chemical composition (and subsequent chemical evolution) can, in turn, affect the physical conditions (and subsequent dynamical evolution) of a star forming region (e.g. see Herbst & van Dishoeck 2009; Garrod & Herbst 2006; Garrod et al. 2008). For example, the overall molecular (and to some degree atomic) content can play an important role in regulating the gas pressure by changing the temperature of the gas via the process of heating and cooling through line-absorption and emission; (Ceccarelli et al. 1996; Goldsmith & Langer 1978). In addition, molecular ions can affect the strength of coupling between the gas and the magnetic fields (which is related to magnetic turbulent support, e.g. Williams et al. 1998). Thus, there is a complex feedback between the physical and chemical conditions in an interstellar gas cloud that either helps drive the star formation process, or hinders it, and which may help determine the masses of the newly formed stars.

In order to understand the origin of chemical complexity in interstellar space and how this chemistry evolves and affects the process of star formation in the Universe (as well as the

¹Also see: <http://www.astro.uni-koeln.de/cdms/molecules> and http://www.astrophys.org/astrochymist_ism.html

formation of planets and pre-biotic chemical species), we require unbiased and complete surveys of spectral lines that span a broad range of wavelengths. These types of datasets are needed so that we can sample a wide variety of molecular and atomic species, as well as obtain multiple emission lines from each of the species, in order to extract the physical conditions in the gas. Fortunately, with the advent of sensitive, high-resolution spectrometers for millimeter/submillimeter wavelengths, especially those developed for space-based observatories, it is now possible to obtain such surveys and to begin to address these issues (e.g. Crockett et al. 2014; Zernickel et al. 2012; Kama et al. 2013; Kamińczak-Barthel et al. 2015).

The key project *Herschel* observations of EXtraOrdinary Sources (HEXOS) (Bergin et al. 2010) was designed to address issues related to the chemical composition of massive star forming regions. HEXOS has obtained spectral line surveys of the Orion-KL, Orion South (hereafter Orion-S), and Orion Bar (Nagy et al. in prep.) regions within the Orion A Molecular Cloud, at high frequencies that are not easily accessible from ground based observatories (480–1900 GHz). Both Orion-KL and Orion-S are relatively nearby (420 pc; Menten et al. 2007) massive star forming regions close to the Orion Nebula. The nearby Trapezium OB stars are the source of high energy photons, which produce Photon Dominated Regions (PDRs) throughout the region. The UV flux ($6 < E < 13.6$ eV) in the vicinity of Orion-S is $\chi = 1.1 \times 10^5 \chi_0$ (Herrmann et al. 1997; Goicoechea et al. 2015), where $\chi_0 = 2.7 \times 10^{-4}$ ergs s⁻¹ cm⁻² sr⁻¹ (Draine & Bertoldi 1996). Observations of Goicoechea et al. (2015) and O'Dell & Harris (2010) suggest that the HII region lies mostly in front of the molecular material, but may wrap behind, at least part of, the Orion-S molecular cloud. That at least some of the Orion-S molecular gas is located in front of ionized material has been convincingly demonstrated by Very Large Array absorption measurements of the H₂CO 6 cm 1₁₀ – 1₁₁ transition (Mangum et al. 1993).

Despite the fact that the far-infrared luminosity of Orion-S ($8.5 \times 10^3 L_{\odot}$; Mezger et al. 1990) is more than an order of magnitude below that of KL, a number of energetic outflows associated with Orion-S suggest ongoing star formation. For example, CO J=2–1 SMA observations (Zapata et al. 2005) revealed a highly collimated bipolar outflow extending $\sim 30''$ over the velocity range ~ -80 to ~ -26 km s⁻¹ and ~ 22 to ~ 82 km s⁻¹ oriented NW-SE. The sub-millimeter continuum source with a deconvolved size $0.6''$ and an integrated flux of 116.2 ± 9.0 mJy at 1.3 mm is well centered on the bipolar outflow axis, $\alpha_{2000} = 05^h35^m13.550^s$, $\delta_{2000} = -05^{\circ}23'59.14''$. In addition, another quite extended, collimated, low-velocity (5 km s⁻¹) CO outflow has been observed, oriented NE-SW (Schmid-Burgk et al. 1990), and a low-velocity (10 km s⁻¹) bipolar SiO (5–4) outflow with a length $\sim 30''$ (oriented NE-SW) has been reported by Ziurys et al. (1990). Four other SiO outflows are also listed by Zapata et al. (2006).

Despite the presence of star formation activity, as indicated by the IR luminosity and molecular outflows, BIMA observations of a few selected species by McMullin et al. (1993) suggest that the chemistry of Orion-S resembles that of the Orion-KL quiescent ridge and has fewer, narrower and weaker lines than KL. These observations may imply that Orion-S is a more quiescent and younger star forming region, in which the star formation activity has not had time to significantly alter the dynamics and chemistry of the region. This idea is also

consistent with dynamical ages from outflow observations in Orion-S (i.e. Schmid-Burgk et al. 1990; Bally et al. 2000; Zapata et al. 2005). Assuming no projection effects, the maximum corresponding dynamical age for the largest outflow is found to be less than 45000 years which is still remarkably young (Schmid-Burgk et al. 1990). The dynamical age for all the other outflows can be shown to be less than 5000 years (Bally et al. 2000; Zapata et al. 2005). A more detailed comparison between Orion-S and Orion-KL is, therefore, of great interest, since the two regions presumably formed under similar conditions, but could have very different chemical abundances possibly based on differences in their ages, densities, temperatures, radiation fields, etc.

In this paper we present a comprehensive study of the *Herschel*/HIFI spectral survey toward Orion-S. The observations presented here were obtained as part of HEXOS and span over 1.2 THz of frequencies, mostly not accessible from the ground. In §2 we present our observations and data reduction methods, including the removal of off-position contamination, line identification, and Gaussian fitting of the spectral features. Our results (including LTE modeling of each individual species) together with a chemical comparison of Orion-S are presented in §3. The conclusions are provided in §4.

2 Observations & Data Reduction

The data presented in this paper were taken with the Heterodyne Instrument for the Far-Infrared (HIFI) (de Graauw et al. 2010), one of three instruments aboard the *Herschel Space Observatory* (Pilbratt et al. 2010). HIFI operated over the frequency range 480–1900 GHz (with two gaps: one at 1280–1430 GHz, due to the switch between SIS and HEB detectors (Roelfsema et al. 2012), and one at 1540–1570 GHz, which was an observational time saving strategy since this frequency range was expected to have few transitions). HIFI was separated into 14 different bands (1a, 1b, ..., 7b). Each receiver band had independent channels for horizontal (H) and vertical (V) polarizations, each with its dedicated Wide Band Spectrometer (WBS) having a native spectral resolution of 1.1 MHz (Roelfsema et al. 2012). Bands 1–5 were observed with a LO redundancy of 6, whereas Bands 6 and 7 used a redundancy of 2. Redundancy refers to the number of observations of each sky frequency with different LO settings. For example, redundancy of 6 means that each frequency in the band was observed with 6 different LO settings. This redundancy was necessary in order to distinguish lines originating from the upper and the lower sidebands (Comito & Schilke 2002). A redundancy of 2 was sufficient for bands 6 and 7 due to the relatively lower density of transitions at these high frequencies. The central position of Orion-S was $\alpha_{2000} = 5^h35^m13.44^s$, $\delta_{2000} = -5^\circ24'08.1''$. All observations were taken in Dual Beam Switch (DBS) mode using the Fast Chop option (>0.5 Hz chop frequency).

We used the hifiPipeline task in HIPE 9.0 for all data reduction. The hifiPipeline task is a pre-compiled script in HIPE used to process level 0 data to any higher level (e.g. 0.5, 1.0, etc.). See Ott (2010) for a description of the various data products. Spurious spectral features were removed and fully calibrated, double side band (DSB) spectra were deconvolved into single sideband (SSB) spectra (e.g. level 2.5). Additional details on data reduction and observational parameters can be found in Bergin et al. (2010) and Crockett et al. (2010). After processing by HIPE 9.0, the H and V polarizations were coadded (except for Band 4a

which, due to processing errors specific to this band, had much noisier V polarization data that were excluded) and then the spectra were Hanning smoothed by two to sixteen channels (see Table 1) to improve the signal to noise ratio. Results are provided in Table 1, which shows typical values for the 1σ rms noise, system temperature, velocity and frequency resolutions after smoothing, and the number of channels smoothed for each band. The 1σ rms noise is calculated from line-free regions of the spectrum immediately adjacent to the lines. A noise range is provided since the noise is not uniform across the bands.

All data in this paper are presented on the T_A temperature scale and, for subsequent analysis, were converted to T_{mb} using the main beam efficiencies in Müller et al. (2014)². The final data after deconvolution and spectral smoothing (bands 1a–7b) are shown in Figures 1–4, in which the T_A range is in Kelvin and frequency in MHz. The strongest lines are labeled in each band, and in order to make the residual noise recognizable and comparable from one band to another the intensity is fixed to 15 K for all bands. Note that certain broad features, like the one near 790 GHz, are most likely due to excess noise, since individual observations show quite a few noise spikes in these spectral ranges.

2.1 Removal of Off-Position Contamination

As described in the previous section, the HEXOS Orion-S spectral survey was observed in DBS mode. Since the observations used the chopper in this mode, the reference positions were fixed to ~ 3 arc minutes from the target position, with an angle set by observatory constraint. In a crowded field like the Orion Molecular Cloud region, it is very likely that the reference position is not free of emission or absorption for some or all molecular lines detected. Typically, emission (absorption) in the reference position appears as an absorption (emission) like feature in the final spectrum. Since the case of absorption in the reference beam is rare, due to a low continuum flux, we will consider only emission. Figure 5 an image of the dust emission at a wavelength of $250\ \mu\text{m}$ obtained with the *Herschel*/SPIRE instrument. The positions of the Orion-S observations and the two reference observations for each of the 14 HIFI bands are overlaid. The diameters of the circles shown represent the FWHM of the individual beams for the center frequencies of each HIFI band. It is apparent that a few of the reference observations (on the east side) were located near the Orion Bar region, making reference beam line contamination very likely. In addition, we even captured emission in the lower-J ^{12}CO transitions in the opposite chopping direction.

The identification of potentially contaminated lines was first performed after the deconvolution by checking the line profile of the detected lines. Once lines were identified, we performed additional tests by subtracting the Level 0.5 nod2 reference spectrum from the associated nod1 reference spectrum of the scans that cover the frequency ranges of these lines. If the resulting spectrum showed only noise we assumed no emission in the reference spectra (we never experienced the case that emission in both reference beams cancelled out perfectly, which would hide this problem). If the resulting spectrum showed an emission line, there was emission in the nod1 reference beam; and if the spectrum showed an absorption feature, there was emission in the nod2 reference beam.

²http://herschel.esac.esa.int/twiki/bin/view/Public/HifiCalibrationWeb#HIFI_performance_and_calibration.

In order to remove the emission in the reference beams, we used the *Herschel*/HIPE hifiPipeline task to create the Level 0.5 product, in which the reference observations are still separated from the target observations. A custom HIPE script then extracted all affected reference scans and the neighboring scans taken before and after the affected scans that have slightly changed LO-settings such that the contaminating emission is at sufficiently different intermediate frequencies (IF). The repair is based on the assumption that the bandpass of all observations changes only very little with small changes in the LO-setting. The primary change is in the amplitude, while the shape of the bandpass changes negligibly. Thus, we could use the neighboring reference scans to repair the contaminated reference flux.

The first step of the repair was to determine the IF-frequency interval $[f_l, f_h]$, covering the reference beam emission and two smaller, abutting intervals $[f_l - \Delta, f_l]$ and $[f_h, f_h + \Delta]$, indicated by the green areas in Fig 6, for scaling. The next step included extracting and averaging the flux of the neighboring scans over the frequency range $[f_l - \Delta, f_h + \Delta]$ (Ref 1 and Ref 2 in Figure 6). Then, to properly scale the averaged flux to replace the contaminated flux, we determined the ratios of the original reference flux to the averaged flux over the two green intervals, interpolated the corresponding values over the interval containing the contaminated flux (the white area in Figure 6), and calculated the new reference flux by multiplying the averaged flux with the just determined ratio over the entire frequency range $[f_l - \Delta, f_h + \Delta]$. This new reference flux (New Ref) now replaced the original reference flux (Orig Ref). From here on, we continued to use the *Herschel*/HIPE hifiPipeline task to create the Level 1.0 and higher products.

The lines that needed repairs are: B1a ([CI]), B2b (H_2S , C^{18}O , ^{13}CO , C^{17}O), B3a (CO , [CI], CH^+), B3b (C^{18}O , ^{13}CO , C^{17}O , CO), B4b (H_2S , C^{18}O , ^{13}CO), B5a (C^{17}O , CO , C^{18}O , ^{13}CO), B7a (CO), and B7b (CO , [CII]). Figure 7 shows an example of how the repair recovered the true line profile of the [CII] 158 μm line.

2.2 Line Identification

We used CASSIS³, a Java based software package designed to analyze astrophysical spectroscopic data to perform the line identification and modeling. Our line identification procedure involved two main steps. First we visually identified the strongest (well above 5σ signal-to-noise) and best known emission lines in the spectrum (e.g. from CO , CS , HCO^+ , HCN , H_2O , etc.) and some of their isotopologues utilizing the JPL⁴ (Pearson et al. 2005) and CDMS⁵ (Müller et al. 2005) spectral line databases. These databases include tabulated values of the central frequency error for each transition. Although in some cases, the difference between the listed centroid frequency of a particular transition from these two catalogues is larger than their given error bars, the observed line width of the transition usually compensates for this ambiguity and makes the identification robust. Many of the strongest identified species are shown in Figures 1-4. In these cases, line blending (e.g. the appearance of more than one transition/species at a single frequency) is not considered a

³CASSIS was developed by IRAP-UPS/CNRS. See: <http://cassis.irap.omp.eu>

⁴<http://spec.jpl.nasa.gov/ftp/pub/catalog/doc/catintro.pdf>

⁵<http://www.astro.uni-koeln.de/cdms/catalog>

problem since the emission from the well-known species will invariably overwhelm the weak emission from a less well-known and, presumably, lower abundance blended line.

Once the strongest emission lines were accounted for, we examined all other spectral lines in our data that had a signal-to-noise ratio above 3σ (in peak intensity). We first performed the line identification via visual inspection of each spectral feature in each HIFI band and compared the transition's frequency to those listed in the databases. From the possible database entries we investigated all species with transitions that fell within a Doppler velocity range of 5.5 to 8.5 km s⁻¹ (i.e. within ± 1.5 km s⁻¹ of the assumed central velocity of Orion-S). Within this velocity range we examined a smaller sub-sample of possible spectral lines with upper state excitation energies (E_{up}) less than 1500 K. If a single database entry from this sub-sample matched the observed spectral feature, we considered this to be a tentative identification. In order to confirm or reject this tentative identification, we then searched for other predicted transitions of the selected species in all of the HIFI bands. If we saw other spectral features in the data that matched the predicted frequencies, we accepted the initial line identification as likely correct. If we did not, then the initial line identification was still considered to be only tentative, since we realize that the absence of other predicted transitions may be due to special excitation conditions. Therefore, in both cases, in order to finally confirm or reject our initial line identifications, Local Thermodynamic Equilibrium (LTE) modeling was performed (described in detail in Section 3), which allowed us to determine if all the observed spectral features from the tentatively detected species could be theoretically reproduced under uniform excitation conditions.

Our LTE models explored excitation conditions with $T_{\text{ex}} = 1500$ K (where T_{ex} is the excitation temperature - equal to the kinetic temperature in LTE), $E_{\text{up}} = 1500$ K, and total species column density 10^{17} cm⁻². If the LTE model produced emission at the frequency of the spectral feature then the line identification was considered confirmed. If not, the species was assumed to have been incorrectly identified and a new identification for that spectral feature was sought. Note, at this stage we are simply trying to produce some visible model emission at the frequency of the spectral feature and not trying to fit or replicate the observed spectral line profile. This will be performed in a subsequent stage described in Section 3.1. If a spectral feature could not be reproduced by an LTE model of any species, or if there was no database entry at the frequency of the observed spectral feature, that feature was listed as an unidentified line (32 lines in total). Visual inspection of the original, DSB spectra indicates that all of these features are “ghosts” (i.e. artifacts of the deconvolution routine). A list of all identified species is given in Table 2. A frequency ordered list of all spectral features above 3σ in intensity (as well as their peak intensity) is given in Table 3. Ghost lines are identified as “ghost”. In total we identified 52 different species (including isotopologues) which are responsible for 685 transitions (including the blended lines) in the HIFI spectra. It is, of course, possible that additional species and transitions exist in Orion-S, but at intensities too weak to be detected. This will be addressed in Section 3.3.2.

In some cases, our LTE modeling resulted in a particular spectral feature being reasonably explained by a superposition of lines from more than one species/transition (i.e. blended lines). In order to account for the possible effects of line blending, we performed modeling of all transitions of the two species in all HIFI bands. After obtaining good fits to the

unblended transitions, we were able to determine how much each species contributed to the blended feature. An example of a blended line is shown in Figure 8, in which the data are shown by the black histogram, the solid red line indicates a C^{17}O transition, the solid blue line indicates an H_2CO transition and the solid green line is the superposition of these two model results. Note that the solid green line in Figure 8 does not represent a multicomponent Gaussian fit but rather the LTE modeling required to reproduce the line profiles (see Section 3.1). Given the relatively few spectral lines in Orion-S, significant blending was only a problem in 6 of 685 lines detected. These blended lines are indicated by a “b” superscript in Tables 3 and 4. In Table 3 both species are listed. Blended lines were excluded from the modeling analysis presented in Section 3.

2.3 Line Profiles

Although all lines above the 3σ S/N level in intensity were identified, Gaussian fitting and subsequent modeling was only performed on lines that were above the 5σ noise level (where the noise is calculated from line-free regions of the spectrum immediately adjacent to the line). Gaussian fits were obtained using the Levenberg-Marquardt algorithm as implemented in the CASSIS software package and was done independently from LTE modeling, the latter of which will be described in Section 3.1. A linear or a second order baseline was fit to the data prior to Gaussian fitting but was not removed so we could include the continuum in subsequent modeling (important for absorption lines).

In most cases, a single component Gaussian fit to a specific species could reasonably reproduce the observed lines. However, in some cases a two component Gaussian fit was needed, one component being narrow ($V_{FWHM} = 3\text{--}5 \text{ km s}^{-1}$) and the other broad ($V_{FWHM} = 7\text{--}14 \text{ km s}^{-1}$); the latter could be the effect of a hot core, an outflow, or a shock. Figure 9 provides an example of a species that needed only a single component fit (^{13}CO), whereas Figure 10 shows the spectra for HCN, a typical example of a species requiring a two component fit. In addition, $^{12}\text{C}^{16}\text{O}$ line profiles are the only ones among 52 identified species, which clearly had a non-Gaussian shape, probably due to self absorption. A few other transitions are seen in absorption rather than emission and are listed in Table 3 with negative intensities.

Table 4 shows the results of the Gaussian fitting for each species. The reported result for each individual line profile is the best Gaussian fit. We should note that, usually, the signal to noise ratio is lower, as we move to higher frequencies. In case of a two component fit the narrower component is referred as “main” and the broad component is referred to as “wing”. The first column in Table 4 is the transition quantum number (an explanation of the quantum numbers is provided on the CDMS and JPL websites). The centroid frequency of the fitted Gaussian profile is listed in the second column. T_A and V_{LSR} are respectively the observed antenna temperature and centroid velocity of the corresponding Gaussian fit. V_{FWHM} is the “Full Width Half Maximum”, and $\int T_A dV (\text{km s}^{-1})$ is the integrated line intensity.

Note that Gaussian fitting was performed on each line separately (i.e. we did not utilize a single set of Gaussian parameters to fit all transitions simultaneously). This implies that each transition of a given species can have slightly different V_{LSR} and V_{FWHM} . This effect is best demonstrated using methanol as an example, since it has the largest number of

transitions. The mean values of V_{LSR} and V_{FWHM} for methanol A & E combined is $6.6 \pm 0.3 \text{ km s}^{-1}$ and $4.7 \pm 0.9 \text{ km s}^{-1}$ respectively, where the errors are the 1σ standard deviations about the mean. The calculated scatter about the mean, however, is an intensity dependent parameter. Figures 11 and 12 plot V_{LSR} and V_{FWHM} vs T_A ($> 5\sigma$) for all the fitted methanol A & E transitions in Table 4, and clearly show that the scatter in both fitted parameters decreases with increasing T_A . For transitions with $T_A < 0.5 \text{ K}$, $\langle V_{LSR} \rangle = 6.59 \pm 0.39 \text{ km s}^{-1}$ and $\langle V_{FWHM} \rangle = 4.99 \pm 0.92 \text{ km s}^{-1}$. Whereas for transitions with $T_A > 0.5 \text{ K}$, $\langle V_{LSR} \rangle = 6.57 \pm 0.23 \text{ km s}^{-1}$ and $\langle V_{FWHM} \rangle = 4.39 \pm 0.67 \text{ km s}^{-1}$. This suggests that most of the observed scatter in these parameters is not due to the emission itself but it is due to our Gaussian fitting procedure, which clearly is subject to larger errors for weaker lines. This behaviour is predicted by Porter et al. (2004) who show that the error in V_{LSR} and V_{FWHM} from Gaussian fitting increases with decreasing signal to noise. The green and the blue lines on Figures 11 and 12 denote, respectively, the 1σ and 3σ theoretical error envelope. These were calculated from equation A.1 in Porter et al. (2004) assuming $\langle V_{FWHM} \rangle \sim 5 \text{ km s}^{-1}$ and $T_{ms} \sim 0.1 \text{ K}$ (typical values for methanol) and illustrate this effect quite clearly.

HIFI data obtained in beam switching mode generally provide quite a good measure of the continuum. Therefore, in each band, we have integrated the emission over the entire frequency range to obtain the line+continuum emission. Summation over the integrated intensities, listed in Table 4, of all the transitions in each band provides the corresponding total line emission. Comparing the two provides the line to continuum ratio, which is interesting for the interpretation of broadband continuum images of star forming regions. The advantage of our data is that the line and continuum emission are measured in the same beam with the same instrument and, therefore, there are no complications that arise from cross-calibration between different instruments or beam sizes. Figure 13 plots the band integrated continuum emission (red triangles), the integrated line emission in each band (blue triangles) and, on the right y-axis, the percentage line to continuum ratio (green circles). The figure shows that the line to continuum ratio is $\sim 3 - 1\%$ in bands 1a–2a and drops to less than $\sim 0.5\%$ in the higher bands. These are both smaller than the $\sim 10\%$ seen in Orion-S in the 300 GHz band (Groesbeck 1995) suggesting that the line to continuum ratio generally decreases with increasing frequency. The dramatic drop in the line to continuum ratio between Band 1a to 2b is due to two factors. Over this frequency range, the continuum emission rises by a factor of a few while, at the same time, the number of spectral lines and their corresponding intensity drops by a factor of a few. The red line is a power law fit to the red triangles using a modified black body in which the Planck function is multiplied by $\kappa_o(\nu/\nu_o)^\beta$, where κ_o is the dust mass opacity coefficient. The best fitted value for β is 1.0. This value is consistent with the behaviour of dust in other studies of star forming regions (e.g. Shetty et al. 2009).

3 Results & Discussion

3.1 LTE Modeling

LTE modeling assumes that the gas is in Local Thermodynamic Equilibrium, meaning that the density is sufficiently high that collisions dominate the excitation. The LTE modeling

capability implemented in CASSIS has 5 input variables, N_t , T_{ex} , V_{LSR} , V_{FWHM} , Ω , where N_t is the total column density, T_{ex} is temperature, and Ω is the size of the emitting region (which couples to the variable HIFI beam sizes to take into account beam dilution effects). Note that by definition, under LTE conditions, the excitation temperature that determines the relative populations of the upper and the lower level of a spectral line, the rotation temperature that describes the populations of all the rotational levels of one species and the gas kinetic temperature are all identical. Each combination of these variables produces a Gaussian model spectrum for each transition of the selected species. Note that, unlike the Gaussian fitting procedure which fits the V_{LSR} and V_{FWHM} to each line separately, for the LTE modeling we obtain a single average value of V_{LSR} and V_{FWHM} for all transitions of a given species.

In order to find the set of parameters which produce synthetic spectra that best fit the observed spectral line profiles, we used a Markov Chain Monte Carlo (MCMC) method implemented in CASSIS (e.g. Guan & Krone 2007). The MCMC method randomly picks a seed in the five dimensional parameter space (that we call the X_0 state). Then it randomly chooses one of the nearest neighbors (called the X_1 state), as specified by a variable step size, which is calculated for each iteration. The χ^2 of the new state is calculated and if $p = \chi^2(X_0)/\chi^2(X_1) > 1$ then the new state is accepted. If $p = \chi^2(X_0)/\chi^2(X_1) < 1$ this new state might still be accepted with a certain acceptance probability. If the new state is rejected the X_0 state will remain, and another random nearby state will be picked as the X_1 state. Having a finite probability to accept a new position even if the χ^2 is worse, ensures we do not converge directly to a local minimum, but instead forces better sampling of the full parameter space. The code runs with several initial random states and, usually, when the variance among different clusters of states is smaller than the variance of each cluster, it is assumed to have converged to the correct solution (Hastings 1970; Roberts et al. 1997). When the code approaches convergence, it calculates a number of models and χ^2 values in a tight cluster surrounding the “best” solution. This allows us to calculate a median value for each fitted parameter and its statistical standard deviation, which are listed in Table 5.

Despite the fact that we identify all transitions above 3σ , for our modeling we only utilize transitions above 5σ , while neglecting the blended lines. However, when exploring the validity of our models we also investigate frequency regions where potential transitions of the selected species exist in the molecular line databases, but were not detected above 3σ . This ensures that our models do not produce synthetic spectra where no transitions are actually observed. At the beginning of the procedure we usually let all five parameters vary. However, frequently we were able to find good solutions for the V_{LSR} and FWHM after the first convergence of the code. Therefore, on subsequent runs, we fixed the V_{LSR} and FWHM and allowed the other three parameters to vary. This significantly speeds up the computational time of subsequent runs. Once we obtain a good fit, we run the code five to ten more times to ensure that different runs converge to the same solution within the error bars. In some cases, after running the code five to ten times, the scatter of the converged solutions is larger than the standard deviation of any of the individual solutions. In this case, in Tables 5 and 6 we report the average of the multiple runs (i.e. we take the median value of each run and compute the average between runs) and the standard deviation of the solutions about this new average. In all cases we let the source size (Ω) vary up to $90''$ twice that of

the largest HIFI beam ($\sim 45''$). However, if the source size is larger than the largest beam it is essentially unconstrained (although there is some sensitivity to source sizes that are larger than the beam since the beam is Gaussian in shape and not a tophat profile). In such cases, the source is simply considered to be extended in nature. Table 5 provides the results of our MCMC χ^2 fitting of the spectral lines listed in Table 4 (i.e. those with $S/N > 5\sigma$). Column 1 is the species, column 2 lists the median total column density of the species and the standard deviation, column 3 is the excitation temperature, column 4 the FWHM line width, column 5 is the source size (Ω), and column 6 is the median LSR velocity. In cases where the error is not listed, the parameter was fixed in the MCMC fitting routine. Table 5 shows that the column density uncertainties range from 10–50%. To ensure that our assumption of LTE is valid, we ran the same MCMC fitting procedure using the non-LTE (RADEX) models implemented in CASSIS for a handful of species (N_2H^+ , SO_2 , ^{13}CO , and DCO^+). In all cases, the non-LTE column densities are consistent and within the reported error bars of the LTE models, as shown in Table 5. Given that the errors in Table 5 are the statistical uncertainties on the LTE solutions, to account for the possibility that LTE is not always a good approximation, we suggest that uncertainties on the high side of this range are probably appropriate.

Figure 9 provides an example of one component modeling for ^{13}CO . The apparent shift in centroid velocity between the data (black histogram) and the LTE model (red Gaussian curve) is seen in a number of species and can also be seen by comparing the tabulated V_{LSR} listed in Tables 4 and 5. These apparent shifts of a few tenths of a $km\ s^{-1}$ are caused by the fact that the spectral lines are not perfectly Gaussian in shape; in some cases possibly due to optical depth effects. In addition, the MCMC routine optimizes a number of free parameters to obtain the best overall physical model which fits all spectral lines simultaneously; as opposed to the Gaussian fitting routine, which simply fits a mathematical Gaussian profile to each spectral line separately. Thus, the median V_{LSR} and V_{FWHM} determined from the LTE modeling may not perfectly match the actual V_{LSR} and V_{FWHM} of any individual transition.

Although one component modeling usually results in a remarkably good fit to the observations (e.g $C^{18}O$, CH, CCH, etc), there are some cases in which a second (broad) component is necessary to properly reproduce the observations. This is independent of the broad line wings seen in the transitions of some species that required a two component Gaussian fitting as mentioned in Section 2.3. In some cases, even species that were well fit by a single Gaussian component required two component LTE modeling, one with a narrow line width, and the other with a broad line. This is because, in these cases, there is no single combination of model parameters (notably T_{ex} and N_{tot}) that could reproduce the intensities of all transitions simultaneously. The two component LTE modeling implementation in CASSIS uses a two slab model; from the perspective of the observer, component 1 is the front slab and component 2 is the slab located behind it. The code allows component 1 to absorb emission from component 2. The results of the two component MCMC LTE modeling are listed in Table 6. Figure 10 provides an example of a species for which two component modeling was required. To see if this could be the result of non-LTE effects, we also attempted to model these species using the RADEX code (van der Tak et al. 2007) as implemented in CASSIS. For the RADEX modeling we used the identical parameter range

as for the LTE modeling. RADEX, however, invokes one additional free parameter, namely the H_2 volume density which we allowed to range from 10^2 to 10^{10} cm^{-3} . In all cases, the RADEX modeling was unable to produce a good fit to all transitions unless a second physical component was included.

Note that ^{12}CO is not presented in either Table 5 or Table 6 due to the presence of self-absorption from foreground material which complicated the modeling procedure. We do, however, model the broad shock/outflow component separately for the analysis presented in Section 3.3.2.

3.2 Comments on Individual Species

The detected species listed in Table 2 can be related to a variety of physical processes that exist in the ISM such as: shocks, UV irradiation by nearby OB stars, and hot core chemistry. In this section we discuss some specific molecules in the context of these physical processes.

3.2.1 Tracers of UV Irradiation—Given the high UV flux in the Orion-S region ($\chi = 1.1 \times 10^5 \chi_0$; Herrmann et al. 1997), it is not surprising that we detect a wide variety of UV tracers.

[CI] & [CII]: [CI] and [CII] are the fine structure lines of neutral atomic and singly ionized carbon. Both have been seen over large regions of the ISM. [CI] is known to trace PDRs at the UV illuminated surfaces of GMCs (Papadopoulos et al. 2004; Plume et al. 1999; Tielens & Hollenbach 1985), and [CII] is a tracer of the interface between the diffuse warm ionized medium and the outermost surface of GMCs (Velusamy et al. 2012). [CII] is also thought to be a tracer of CO “dark gas” (Langer et al. 2010). We have detected all [CI] and [CII] transitions accessible to HIFI, i.e. both of the [CI] ground-state fine-structure transitions: $^3P_1 \rightarrow ^3P_0$ and $^3P_2 \rightarrow ^3P_1$ ($V_{\text{LSR}} \sim 7.5 \text{ km s}^{-1}$), and the single [CII] transition: $^2P_{3/2} \rightarrow ^2P_{1/2}$ ($V_{\text{LSR}} \sim 8.6 \text{ km s}^{-1}$), toward Orion-S. With only one transition of [CII], we modeled the column density assuming that the excitation temperature in the PDR was between 200–500 K. The velocity of [CII] is considerably different from the velocity of the dense, quiescent cloud component of Orion-S as traced by C^{18}O , CS, DCO^+ , HCO^+ , etc. (e.g. $\sim 7 \text{ km s}^{-1}$; see Figure 14). This suggests that [CII] is tracing a kinematically distinct component of Orion-S; most probably photoevaporating material moving away from the molecular clump surfaces (e.g. Goicoechea et al. 2015). [CI], however, does not have a velocity that is dramatically different from the quiescent cloud component and is, in fact, similar to that of C^{18}O (Figure 14). This is probably due to the fact that neutral atomic carbon exists slightly deeper in the cloud ($A_V > 3 - 4$) where it is still mixed with molecular material (see e.g. Hollenbach & Tielens 1997; Mookerjee et al. 2012).

CH^+ , CH & CCH: CH^+ , CH & CCH are often associated with PDRs, with the former two also being tracers of “CO-dark molecular gas” (Nagy et al. 2013; Gerin et al. 2010). In addition, CH^+ and SH^+ can also form via turbulent chemistry in the diffuse ISM (Godard et al. 2012). Transitions above 5σ detected toward Orion-S for these species are listed in Table 4. Enough transitions of CH and CCH were detected above 5σ that we could model the emission from these species (Table 5), both of which were well fit by 1 component models.

For CH^+ , we provide a range of column densities for a range of excitation temperatures between 30–200 K. From the Gaussian fits in Table 4, both CH and CH^+ have similar kinematics ($V_{\text{LSR}} > 8.0 \text{ km s}^{-1}$), whereas the CCH has $V_{\text{LSR}} \sim 7.2 \text{ km s}^{-1}$ (see Figure 14). This suggests that CH and CH^+ trace the same region as the [CII] emission i.e. the UV illuminated surface of the cloud, although possibly a deeper and denser region of the PDR as suggested by Pan et al. (2001). CCH, which has a velocity closer to that of the quiescent gas, likely arises from deeper layers in the cloud (Nagy et al. 2015). The formation pathways for these species may help clarify these velocity differences. For example, CH^+ forms by an endothermic reaction: $\text{C}^+ + \text{H}_2 \rightarrow \text{CH}^+ + \text{H}$ (Federman et al. 1996). The formation of CH follows after a hydrogen abstraction reaction with CH^+ to form CH_2^+ and a subsequent dissociative recombination. Since these two species are closely linked to the C^+ abundance, through one or two steps in the reaction network, it makes sense that they would be linked physically and, therefore, kinematically. The formation of CCH, however, involves additional steps in the reaction chain, starting with the formation of C_2H_2^+ followed by dissociative recombination to form CCH (e.g. Wootten et al. 1980). Since this requires additional reactions involving molecular material, this species is probably more closely linked to the denser molecular gas.

SH⁺ & CO⁺: SH^+ & CO^+ are also species thought to trace regions with enhanced UV fields (Nagy et al. 2013). We detect two weak ($< 5\sigma$) hyperfine components of SH^+ in Orion-S, which are too weak to be fitted or modeled but which, interestingly, are seen in emission rather than the usual absorption line profiles seen in the diffuse ISM (Godard et al. 2012). Although we do not report the Gaussian fit parameters of SH^+ or CO^+ due to the weakness of the transitions, inspection of their lines suggests V_{LSR} of $\sim 8.5 \text{ km s}^{-1}$ which is virtually identical to the [CII] velocity. Although SH^+ can form via turbulent chemistry in the diffuse ISM, given the strength of the UV field in Orion-S, it is likely that the main formation pathway is $\text{S}^+ + \text{H}_2 \rightarrow \text{SH}^+ + \text{H}$. Therefore, like [CII], SH^+ probably also originates in the PDR at the surface of the cloud. The same is true of CO^+ which has a similar V_{LSR} (8.5 km s^{-1}) as SH^+ and [CII], and like CH^+ forms directly from C^+ via the reaction $\text{OH} + \text{C}^+ \rightarrow \text{CO}^+ + \text{H}$.

CN & HCN: CN & HCN have both been detected in Orion-S. While both molecules are good tracers of warm dense gas, the CN/HCN abundance ratio is suggested to be an indirect measure of the UV field (e.g. Fuente et al. 1993); i.e. if the ratio is significantly larger than 1, then the UV field is thought to be enhanced. We have identified the $N = 5-4$, $N = 6-5$ and $N = 7-6$ transitions of CN above the 5σ noise level toward Orion-S and have modeled these transitions using a narrow component (see Table 5). The transitions of HCN ($J = 6-5$ to $13-12$), however, exhibit the characteristic broad line wings that required two component Gaussian fitting and LTE modeling (see Table 6). Figure 10 shows the LTE model fit to our HCN observations. Since the fits are constrained by the rms noise in each spectrum, the higher frequency transitions (which tend to have much larger noise) appear to be less well fit than the lower frequency/lower noise transitions. They are, however, still acceptable fits to the data within the given noise levels. Comparing the CN column density with the narrow component of HCN, we obtain a CN/HCN abundance ratio of 1.2 ± 0.6 indicating a

moderately enhanced UV field. Given the high critical densities of these transitions ($\sim 10^8 \text{ cm}^{-3}$) it is unlikely that they originate at the UV illuminated cloud surface. Instead, both their critical densities and the CN/HCN abundance ratio of 1.2 suggest that they arise deeper in the cloud (around $A_V > 5$; Fuente et al. 1993) and, therefore, are more closely associated with the dense molecular gas. This is also borne out by their velocities, which are similar to the dense, quiescent cloud component (Figure 14).

3.2.2 Complex Organic Molecules and precursors—Complex organic molecules are often associated with hot core chemistry. Unlike Orion-KL in which a plethora of complex organic molecules were detected (Crockett et al. 2014), in Orion-S we only detect a handful of molecules that might be considered complex.

CH₃OH: Methanol is an asymmetric top molecule, whose internal rotation results in two distinct symmetry species A-CH₃OH and E-CH₃OH. In total we observed 359 methanol transitions above 3σ toward Orion-S, 170 A-CH₃OH and 189 E-CH₃OH. 198 of the lines were above the 5σ noise level, 111 A-CH₃OH and 87 E-CH₃OH. While methanol is known to be a good temperature probe (e.g. Beuther et al. 2005; Wang et al. 2011), detailed modeling of methanol is beyond the scope of this paper and will be the subject of future work.

H₂CO: Formaldehyde is another commonly used tracer of gas temperature (e.g. Mangum & Wootten 1993), in which the two hydrogen atom spins separate the molecule into distinct ortho and para species. Transitions of H₂CO above the 5σ noise level are listed in Table 4. We needed two component LTE modeling for both the ortho and para H₂CO molecules since one component models could not simultaneously reproduce all observed transitions. The modeling (Table 6) results in low temperatures for the narrow component ($T_{\text{ex}} \sim 45 - 50 \text{ K}$) and higher temperatures ($T_{\text{ex}} \sim 150 - 165 \text{ K}$) for the broad component. The large linewidths and the fact that the estimated source sizes are quite large ($> 45''$) may indicate that the high temperature H₂CO emission arises from shocks in the outflows rather than from a “hot core” region. Ortho to para ratios in the narrow and broad components are 0.8 ± 0.1 and 0.6 ± 0.1 respectively. These low values are also consistent with our results for H₂S (see below). The spin temperatures associated with the ortho and para species are $7 \pm 1 \text{ K}$ and $6 \pm 1 \text{ K}$ respectively, suggesting that if formaldehyde formed under LTE conditions that the formation temperature was very low.

CH₃OCH₃: Dimethyl ether is a complex molecule detected toward Orion-S. Since this molecule has no transition above 5σ , we only report it as a detection in Table 2.

The lack of complex organic molecules suggests that if hot cores exist in Orion-S they are still in their infancy and have not had time to either expand dynamically or develop chemically. This is not surprising given the very small size of the embedded submillimeter continuum sources detected in the region (Zapata et al. 2005). In addition, if these submillimeter continuum sources are indeed hot cores they are approximately 10 times smaller than the Orion-KL hot core. Therefore, the beam dilution in Orion-S would be a 100 times worse. Thus, any transitions arising from the Orion-KL hot core that have an intensity less than a few K in the survey of Crockett et al. (2014) would be undetectable in our survey

if they originate from the considerably smaller region in Orion-S. Alternatively, it is possible that Orion-S is not a massive star forming region at all and, therefore, there are no hot cores in this region. Observations with higher spatial resolution or at lower frequencies (with associated lower excitation temperatures) would help address this issue by revealing the presence of more complex organics.

3.2.3 Pure Shock Tracers

SiO: SiO abundances can be enhanced by more than two order of magnitudes in hot and shocked regions (e.g. Iglesias & Silk 1978; Martin-Pintado et al. 1992a) and SiO emission is often used as a tracer of molecular outflows since the SiO emission traces the outflow material itself, rather than the dense protostellar core (Martin-Pintado et al. 1992b). This is believed to be due to Si-bearing dust grains being shattered by the outflow, followed by a rapid gas-phase reaction with free oxygen to produce SiO (e.g. Schilke et al. 1997b; Gusdorf et al. 2008a,b). A number of outflows have already been identified in Orion-S by Zapata et al. (2006). In our data, although we could not identify any SiO emission above the 5σ level, we have identified three SiO transitions above the 3σ level ($J=12-11$, $13-12$, $14-13$, $v=0$) at the velocity of 6.2 km s^{-1} (similar to the quiescent gas). With additional spectral smoothing (to a velocity resolution of $\sim 4 \text{ km s}^{-1}$) it is clear that these transitions are real, with $S/N > 5\sigma$. These transitions are quite broad ($\Delta V \sim 20-30 \text{ km s}^{-1}$), which is reasonable considering the observed characteristics of the SiO outflows as seen by Zapata et al. (2006). Given the existence of such high- J transitions with excitation energies above $\sim 150 \text{ K}$, this indicates the presence of at least a small amount of hot shocked SiO in Orion-S.

3.2.4 Tracers of Quiescent Gas

CO, ^{13}CO , C^{18}O , C^{17}O , & $^{13}\text{C}^{18}\text{O}$: For all carbon monoxide isotopologues, excluding $^{12}\text{C}^{16}\text{O}$ itself, one component Gaussian fitting and LTE modeling match the observations remarkably well. $^{12}\text{C}^{16}\text{O}$ itself, however, exhibits a broad line wing (clearly tracing an outflow/shock) and, due to the presence of self-absorption, was not modeled. The existence of an outflow is not visible in any of the $^{12}\text{C}^{16}\text{O}$ isotopologue transitions due to their lower abundances. The LTE modeling of ^{13}CO is shown in Figure 9. For all $^{12}\text{C}^{16}\text{O}$ isotopologues (except $^{13}\text{C}^{18}\text{O}$) we see transitions from $J=5-4$ to $11-10$ above the 3σ level. For $^{13}\text{C}^{18}\text{O}$ the highest transition we detect above 3σ is $J=7-6$. The higher J transitions are buried in the larger noise of the higher frequency HIFI bands. For $^{12}\text{C}^{16}\text{O}$, however, we detect lines up to $J = 16-15$. For the isotopologues, the typical V_{LSR} is approximately 7 km s^{-1} , indicating that these species trace the quiescent gas in the cloud. The V_{LSR} of the main isotopologue, however, is often a bit higher than this, probably due to the Gaussian fits being skewed by the presence of self-absorption in the spectra, or due to the fact that with its high opacity $^{12}\text{C}^{16}\text{O}$ may be tracing a different physical region of the cloud. Interestingly, in Table 5, a correlation can be seen between the CO isotopologues and the derived excitation temperature; with the more optically thick species, which trace the cloud surface (e.g. ^{13}CO) having a higher temperature than the optically thin ones which preferentially trace the interior (e.g. $^{13}\text{C}^{18}\text{O}$). This suggests that the external UV field is responsible for much of the heating in Orion-S (see also Tauber & Goldsmith 1990). This is different than the usual case of isolated star formation, in which the gas is predominantly heated internally by the process of gravitational collapse and the formation of an embedded protostar.

Deuterium-Bearing Molecules: Deuterated species are subject of considerable interest in the ISM, since the D/H ratio in molecular clouds can be considerably enhanced over the cosmic value of $\sim 10^{-5}$. In Orion-S we detect only a few deuterated species: DCN, DCO⁺, and HDO, which all have velocities similar to that of the quiescent gas. Enhanced deuteration can occur because fractionation reactions involving deuterium are favoured in low-temperature environments associated with pre-stellar cores, the resultant deuterated molecules can freeze onto grains, and then be released back into the gas phase when star formation activity begins to heat the natal gas (e.g. Ceccarelli et al. 2007). Thus, deuterated species such as DCN and HDO can trace the chemical history of the gas. In Orion-S we found the DCN/HCN column density ratio to be 0.02 ± 0.01 , suggesting considerable enhancement in cold gas. The DCO⁺/HCO⁺ column density ratio is 0.03 ± 0.02 . While the DCO⁺ abundance can be enhanced in cold gas via H₂D⁺, Parise et al. (2009) have shown that deuteration can also occur in the gas phase of warm regions like the Orion Bar via the CH₂D⁺ ion. Although we detected three HDO transitions, it was the only species for which we were not able to find any models that converged to a good solution. Therefore, there is no way to give even a rough estimate for the D/H ratio in water.

N₂H⁺: While N₂H⁺, J = 1–0, is often associated with cold, dense gas, we detect N₂H⁺ transitions from J = 6–5 to 10–9. LTE modeling indicates excitation temperatures of ~ 47 K, suggesting that even the dense gas in Orion-S is quite warm. Previous observations of CH₃C₂H in Orion-S (Bergin et al. 1994) confirm this idea. The V_{LSR} of N₂H⁺ (Figure 14) also suggests that it originates from the quiescent gas. The upper limit for the column density of N₂D⁺ with the same excitation condition as found for N₂H⁺ is $5 \times 10^{11} \text{ cm}^{-2}$. This provides a rough estimate of the D/H ratio of < 0.03 .

3.2.5 Tracers of Both Shocked and Quiescent Gas—As previously mentioned, there are a number of species, for which we had to invoke two component LTE modeling in order to fit the observed transitions (see Table 6). Narrow spectral components are usually associated with quiescent gas, whereas broader spectral components trace more dynamic gas that is often associated with shocks. This suggests that species listed in Table 6 can simultaneously exist in both quiescent and shocked gas components. This is not surprising, since Bachiller & Pérez Gutiérrez (1997) show that, in the bipolar outflow L1157, while some species are clearly quiescent gas tracers, many species exist in both components. Of these latter species, their abundances in the shocked gas are often an order of magnitude or more higher than their abundances in the quiescent gas. We will explore the issue of abundances further in Section 3.3.2. Here, however, we will briefly discuss some of the species listed in Table 6 as possible tracers of both shocked and quiescent gas.

H₂O: While H₂O is not listed in Table 6, it is an important molecule in the ISM and has been the subject of a number of important studies using the *Herschel Space Observatory* in both shocked and unshocked gas. Both the ortho and para forms of H₂O were detected in Orion-S, as well as one transition of o-H₂¹⁸O. The H₂O transitions required two component Gaussian fitting due to the presence of a broad line wing in the spectra (Table 4). The modeling of water is a complex affair and is beyond the scope of this paper. However, Choi

et al. (2014) modeled the ortho and para H_2^{18}O in Orion-S and found LTE column densities of $2 \times 10^{11} \text{ cm}^{-2}$ and $2 \times 10^{12} \text{ cm}^{-2}$ respectively, which suggests an ortho to para ratio of 0.1, indicating that it is unlikely that water formed under LTE conditions. Their non-LTE analysis of the data, however, brings the ratio up to a factor of 2. Choi et al. (2014) also show that the ortho to para ratio is ~ 0.3 in the nearby Orion Bar. Both values are well below the usual value of 3, which indicates non-LTE formation mechanism for water in both Orion-S and the Bar, possibly due to photodesorption from dust grains.

H_2S & H_2^{34}S : H_2S is an asymmetric rotor which has ortho and para spin modifications. It is considered to be a tracer of high temperature grain surface chemistry (e.g. Watson & Walmsley 1982). Similar to SO , despite the fact that we fit the H_2S transitions with a single Gaussian in Table 4, H_2S also required a second physical component in order to obtain a good χ^2 fit from the LTE modeling process. As Table 6 shows, we modeled the H_2S emission from the ortho and para spin modifications separately. In both cases, the narrow component has a linewidth of $\sim 3.6 \text{ km s}^{-1}$, a low excitation temperature (24 K), and is fairly extended (emission extending beyond the *Herschel* beam) whereas the broad component has a larger linewidth ($\sim 8 \text{ km s}^{-1}$), is warmer ($\sim 80 \text{ K}$), and yet is still fairly extended ($> 35''$). The ortho to para ratio in the narrow component is 1.1 ± 0.3 and in the broad component is 0.9 ± 0.1 indicating a spin temperature of $9 \pm 2 \text{ K}$. These values are consistent with those determined for H_2O in Orion-S by Choi et al. (2014) and for Formaldehyde (above). Similarly, this low ortho to para ratio suggests either a very low formation temperature for H_2S or that non-LTE effects had an important role in its formation. To model H_2^{34}S , we coupled its single ortho transition with those of the common isotopologue. The isotopic ratio is another possible free parameter in CASSIS, which assumes that the other parameters of both isotopologues are identical. The isotopic ratio converged to 31 ± 9 . Note, however, that there is only one weak transition of H_2^{34}S that we used to determine this ratio. For comparison, typical values for the $^{32}\text{S}/^{34}\text{S}$ ratio in galactic molecular clouds are $\sim 19 \pm 8$ (Lucas & Liszt 1998) which is consistent with the solar value of 23 (Anders & Grevesse 1989).

CS : CS is a well-known tracer of dense gas due to its high critical density (Plume et al. 1992). We observe many transitions of CS , from $J = 10-9$ to $J = 19-18$. Like CO , CS requires two components to be successfully fit by a Gaussian profile and modeled; one narrow ($V_{\text{FWHM}} \sim 4.1 \text{ km s}^{-1}$), extended ($\Omega = 67''$), and cool ($T = 37 \text{ K}$), and the other broader ($V_{\text{FWHM}} \sim 10 \text{ km s}^{-1}$), moderately extended ($\Omega = 35''$), and warm ($T = 108 \text{ K}$). The broad component is not seen in the spectra of the CS isotopologues but was needed to successfully model the transitions. ^{13}CS and C^{34}S were modeled in a fashion similar to that of H_2^{34}S (i.e. the transitions of the isotopologues modeled simultaneously with those of the common isotope, and found to have isotopic ratio of 46 ± 17 and 14 ± 5 respectively). The Gaussian fitted (Table 5) and modeled velocity (Table 6) of both components is $\sim 7 \text{ km s}^{-1}$, suggesting that both components originate in the same material (Figure 14).

HCN: The transitions of HCN ($J = 6-5$ to $13-12$) exhibit the characteristic broad line wing that required both two component Gaussian fitting and LTE modeling (see Table 6). As is usual for other species, the broad component is hotter (67 K vs 34 K), broader (13.4 km s^{-1} vs 4.4 km s^{-1}), and less spatially extended ($41''$ vs $64''$) than the narrow component. While the broad component's V_{LSR} is lower than that of narrow component (6.6 km s^{-1} vs 7.2 km s^{-1}) both are consistent with the systemic velocity of Orion-S (Figure 14).

HCO⁺: HCO⁺ is another well-known tracer of both dense molecular gas and outflows. We detected the $J = 6-5$ to $J = 13-12$ transitions of HCO⁺ in Orion-S, which span a wide range of physical conditions ($E_{up} = 90 \text{ K}$, $n_{crit} \sim 3.2 \times 10^7 \text{ cm}^{-3}$ to $E_{up} = 389 \text{ K}$, $n_{crit} \sim 6.0 \times 10^8 \text{ cm}^{-3}$). HCO⁺ has some of the strongest lines seen in our survey of Orion-S. Despite the fact that we fit the HCO⁺ transitions with a single Gaussian in Table 4, HCO⁺ required a second physical component in order to obtain a good χ^2 fit from the LTE modeling process (see Table 6). Both components have a velocity of $\sim 7 \text{ km s}^{-1}$ and are fairly warm ($\sim 69 \text{ K}$), suggesting a common origin.

NH₃: We detect two transitions above the 5σ level in Orion-S: one in emission ($1_{0,0} - 0_{0,1}$) and one in absorption ($2_{1,1} - 1_{1,0}$). In fact, we detect 3 additional transitions of NH₃ (all in absorption) but since they were just below the 5σ level, we do not report them in Table 4. Modeling these transitions simultaneously requires two components: a cold ($T \sim 20 \text{ K}$), quiescent ($V \sim 4.2 \text{ km s}^{-1}$) layer of gas in front of a warmer ($T \sim 36 \text{ K}$), broader ($V = 10 \text{ km s}^{-1}$) component. The V_{LSR} values of both NH₃ components are consistent with the systemic velocity of the cloud (Figure 14). The presence of absorption lines provides additional evidence for the existence of two components in Orion-S (one warm and one cool). The fact that the low energy transition is seen in emission, whereas the higher energy transition is seen in absorption may be related to the beam size and the strength of the continuum. At 572 GHz the continuum is weaker than it is at 1215 GHz (see Figure 13) and may be too beam-diluted to see absorption. However, at higher frequencies, the beam couples better to the source and absorption may become more prevalent. This suggests that NH₃ may not come from a high density, hot region which is consistent with our conclusion that there are no hot cores in Orion-S.

SO₂: SO₂ is also often a tracer of shocks, since it can freeze onto grain mantles at early evolutionary times when the gas is cold and dense, and later be returned to the gas phase by shocks (e.g. Millar & Herbst 1990; Esplugues et al. 2013). Toward Orion-S we detected a number of SO₂ transitions above the 5σ level (see Table 4). Given the fact that all the observed SO₂ lines are relatively weak, one component modeling matches the observations remarkably well. LTE modeling for this species (Table 5) shows that the SO₂ is fairly warm ($T_{ex} \sim 150 \text{ K}$), broad ($V \sim 6.7 \text{ km s}^{-1}$), and extended ($\sim 65''$). The velocity of SO₂ is also similar to the velocity of the quiescent gas (Figure 14).

SO: In contrast with SO₂, and despite the fact that we fit the SO transitions with a single Gaussian in Table 4, SO required a second physical component in order to obtain a good χ^2 fit from the LTE modeling process (see Table 6). The narrow component has a line width of 3.8 km s^{-1} , a moderately low temperature (34 K), and is extended beyond the Herschel

beam. Despite the fact that the broad component ($V_{FWHM} = 11 \text{ km s}^{-1}$) is much warmer (122 K), it is still quite extended in size ($35''$).

The large linewidths ($7\text{--}13 \text{ km s}^{-1}$), high temperatures ($70\text{--}150 \text{ K}$), and extended size ($> 30''$) determined for the second physical components of these species suggest that the embedded outflows seen in Orion-S (Zapata et al. 2005; Schmid-Burgk et al. 1990; Ziurys et al. 1990) have affected a large volume of the region both thermally and dynamically. Whether or not these shocks have affected the chemistry of the gas will be examined in Section 3.3.

3.3 Chemical Comparison with Orion-KL

One of the main goals of this project is to explore the chemical differences and similarities between Orion-S and Orion-KL. As mentioned in Section 1, a detailed comparison between the chemical abundances in Orion-S and Orion-KL is useful, since both regions presumably formed under similar conditions, but could have developed very different chemical abundances based on differences in their ages, densities, temperatures, radiation fields etc. As part of the HEXOS survey, and in a direct analogue to our study, Crockett et al. (2014) have observed the same frequency range in Orion-KL using the same instrument. Therefore, we have a perfectly matched database, with which to compare our results. In this section we will compare the chemistries of these two regions. All of the Orion-KL data are taken from the HEXOS survey of this region as listed in Crockett et al. (2014) using the column densities derived from their XCLASS LTE modeling of the data.

3.3.1 Chemical Abundances in Orion-S—Our LTE modeling produces column densities but, to obtain chemical abundances, we must scale each column density by the H_2 column density, which is not known directly. Therefore, we use C^{18}O as a proxy for the H_2 column density. The C^{18}O transitions we observe in Orion-S are optically thin and have only a single narrow component (Table 4) that is well fit by a column density of $3.5 \times 10^{16} \text{ cm}^{-2}$ (Table 5). To convert this to an H_2 column density we use a $\text{C}^{18}\text{O}:\text{H}_2$ conversion factor of 1.7×10^{-7} (Goldsmith et al. 1997) to obtain $N_{\text{H}_2} = 2.1 \times 10^{23} \text{ cm}^{-2}$.

Other species have been modeled using both a narrow and broad component (Table 6), the latter possibly indicative of gas affected by shock. To compute the chemical abundances in the broad component of species listed in Table 6, we need an estimate of the C^{18}O column density specifically present in this broad component. Since the broad component is too optically thin to be detected in C^{18}O or even ^{13}CO , we rely on ^{12}CO instead for this purpose. In this case, we attempt to model the broad (i.e. line wing) component of our observed ^{12}CO lines by fitting three Gaussian components to each transition. The first two Gaussians fit the “main” component of the asymmetric CO profile (see Table 4) and the third fits the outflow ($V \sim 18 \text{ km s}^{-1}$). This third component is then modeled via our LTE procedure to estimate the physical parameters of the ^{12}CO outflow ($T_{\text{ex}} \sim 200 \text{ K}$; $N(\text{CO}) \sim 7.1 \times 10^{16} \text{ cm}^{-2}$; $\Omega > 30''$). Dividing this column density by the canonical $^{12}\text{CO}:\text{C}^{18}\text{O}$ abundance ratio of 500:1 provides a C^{18}O column density of $1.4 \times 10^{14} \text{ cm}^{-2}$ for the broad component in Orion-S; a factor of ~ 250 smaller than the C^{18}O column density in the narrow

component as measured by directly modeling our $C^{18}O$ observations. Using the same $C^{18}O:H_2$ scaling relationship as above we obtain $N_{H_2} = 8.2 \times 10^{20} \text{ cm}^{-2}$

Therefore, dividing the modeled column densities of the broad components of the species in Table 6 by $8.2 \times 10^{20} \text{ cm}^{-2}$ gives the abundance (with respect to H_2) of all species in Orion-S that are possibly affected by shocks. Dividing the modeled column densities of the rest of the species in Table 5, as well as the narrow component of the species in Table 6, by $2.1 \times 10^{23} \text{ cm}^{-2}$ gives the abundance (with respect to H_2) of all species in Orion-S that likely originate in quiescent gas. The results are provided in Table 7 and illustrated in Figure 15, which clearly show that in the broad component (green squares) the abundances are enhanced by a factor of 10–100 with respect to the narrow component (red triangles). Abundance enhancements of this magnitude indicate classic shock behavior (Bachiller & Pérez Gutiérrez 1997). This suggests that shock chemistry is playing an important role in Orion-S.

3.3.2 Species Common to Both Orion-KL and Orion-S—Crockett et al. (2014) detected ~ 13,000 lines from 39 different molecules (79 species if one includes all the isotopologues). This is considerably more than the 685 lines from 52 species (including isotopologues) that we have detected in Orion-S. In addition, the lines in Orion-KL are typically an order of magnitude stronger than those seen in Orion-S. A more interesting comparison, however, is to examine the abundances of species common to the two sources.

Crockett et al. (2014) produce column densities for many of the detected species in Orion-KL. To compare with the chemical abundances in Orion-S (Section 3.3.1), we must also scale by the H_2 column density in Orion-KL. For Orion-KL we use the $C^{18}O$ column densities derived by Plume et al. (2012) as a proxy, which breaks down the results for each of the four known kinematic components: the Hot Core ($V_{LSR} \sim 4 - 6$ and $V \sim 7 - 12 \text{ km s}^{-1}$), the Plateau ($V_{LSR} \sim 7 - 11$ and $V_{LSR} \sim 20 \text{ km s}^{-1}$), the Compact Ridge ($V_{LSR} \sim 7 - 9$ and $V \sim 3 - 6 \text{ km s}^{-1}$), and the Extended Ridge ($V_{LSR} \sim 8 - 10$ and $V \sim 2 - 4 \text{ km s}^{-1}$) (Blake et al. 1987). The H_2 column density can then be produced using the same $C^{18}O:H_2$ conversion factor of 1.7×10^{-7} .

Producing abundances in this way does depend on the assumptions regarding the $C^{18}O:H_2$ abundance ratio. However, by dividing the abundance of a given species in Orion-KL by the abundance of the same species in Orion-S, we eliminate the $C^{18}O:H_2$ abundance ratio altogether and are essentially normalizing to the $C^{18}O$ column density in each region. This does, of course, assume that $C^{18}O$ abundances are the same in both sources, which may be reasonable based upon similarities between the observed $C^{18}O:C^{17}O$ ratios (e.g. 2.5 in Orion-S, 3.0 in the Hot Core, 6.5 in the Compact Ridge, 3.5 in the Plateau, and 2.3 in the Extended Ridge). These ratios are also consistent with those found by Ladd (2004).

Therefore, we are essentially creating the following ratio:

$$\frac{X_{KL}}{X_S} = \frac{\left(\frac{N_i}{N_{C^{18}O}} \right)_{KL}}{\left(\frac{N_i}{N_{C^{18}O}} \right)_S} \quad (1)$$

where N_i is the column density of species i and $N_{C^{18}O}$ is the column density of $C^{18}O$. The subscripts KL and S refer to this ratio in Orion-KL and Orion-S respectively. Given the four distinct kinematic components of Orion-KL, we create this ratio for the Hot Core (HC), the Plateau (P), the Compact Ridge (CR), and the Extended Ridge (ER) separately and, again, use different values for the $C^{18}O$ abundance in Orion-S depending on whether the species in question has a narrow or broad spectral line profile.

Figure 16 shows the comparison between Orion-S and the Orion-KL Hot Core. Note that, by common use, the term “hot core” refers to a dense, warm region surrounding a central high mass protostellar object that dominates its energetics (Kurtz et al. 2000). It has been argued that the eponymous hot core in the Orion-KL region does not fulfil this criterion Zapata et al. (2011). Rather, these authors suggest that this region is rather powered by the aftermath of the explosion caused by a stellar merger event (Bally & Zinnecker 2005). Regardless of this, in the present paper we are comparing the chemical abundances of Orion-S with those in what is traditionally referred to as the “hot core” component of Orion KL. The x-axis indicates the species and the y-axis shows the ratio as calculated from Equation 1. Open red triangles indicate molecules for which one component LTE models in Orion-S were sufficient. In cases where we required two components to model the Orion-S data, the solid red triangles indicate the ratio for the narrow component and the solid green squares indicates the ratio for the broad component. The dotted line connects species/components that likely trace quiescent gas, whereas the dashed line connects species that have a broad component. Not all species detected and modeled in Orion-S are represented in this figure. This is due to the fact that Crockett et al. (2014) did not model all their detected species (notably the atomic species), nor did they provide column densities for species in which the lines were optically thick (e.g. CO, ^{13}CO , HCO^+ , CS) in Orion-KL. Note also that not every species listed in Figure 16 has a symbol associated with it (e.g. CN, HCl, SO, etc.). This is because emission from these species were not attributed to the HC, but to one or more of the other kinematic components in Orion-KL. Error bars are calculated from the statistical uncertainties determined from our LTE modeling of Orion-S (~ 10 – 50% ; see Table 5 and 6) and with the assumption of 10% error bars of the reported column densities in Orion-KL Crockett et al. (2014) which includes the effects of calibration errors, pointing errors, etc. However, to account for the possibility that LTE is not a good approximation in either Orion-S or Orion-KL we add an additional 40% error to the column densities. This value is based on a comparison of LTE versus non-LTE column density calculations for the Orion-KL Extended Ridge (Crockett et al. 2014).

Inspection of Figure 16 clearly shows that the abundances of species in the Orion-KL HC are significantly higher than those in the narrow component of Orion-S (dotted line in Figure 16). Except for CCH, $C^{17}O$, and $H^{13}CO^+$, the abundances in the HC are ≥ 10 times larger

than those in Orion-S. Examining the abundance ratios in the narrow component, we obtain $\left\langle \frac{X_{KL}}{X_S} \right\rangle = 135(\text{SD} = 260)$ where SD is the standard deviation about the mean. The large standard deviation simply reflects the enormous scatter in the ratios (note that the y-axis in Figure 16 is on the log scale). Although still not a good match, the disagreement is smaller for species that have a broad component, (dashed line in Figure 16). In this case we obtain $\left\langle \frac{X_{KL}}{X_S} \right\rangle = 6(\text{SD} = 12)$. Given the lack of complex molecules noted in Section 3.2.2 and the poor match in the abundances between the Orion-KL HC and Orion-S, this suggests that the gas detected in this study of Orion-S does not originate in a hot core.

Figure 17 shows that the abundances of species in the Orion-KL CR are also higher than those in the narrow component of Orion-S ($\left\langle \frac{X_{KL}}{X_S} \right\rangle = 23$; $\text{SD} = 45$) but the agreement is better than it is for the HC. Again, the match is better to the broad component ($\left\langle \frac{X_{KL}}{X_S} \right\rangle = 1$; $\text{SD} = 2$) of the two component fits in Orion-S (dashed line) than it is to the narrow component.

Figure 18 shows the comparison between Orion-S and the Orion-KL Plateau region. The match between abundances here is clearly better than it is for the HC or the CR with $\left\langle \frac{X_{KL}}{X_S} \right\rangle = 14$; ($\text{SD} = 22$) for the narrow component (dotted line) and 1 ($\text{SD} = 2$) for the broad component (dashed line). Note that although SO and SO₂ are often associated with shocked gas they do not appear in Figure 18. This is because these molecules were optically thick and Crockett et al. (2014) did not provide column densities.

The best agreement with molecular abundances in the narrow component of Orion-S is with the Extended Ridge of Orion-KL (Figure 19) where we obtain $\left\langle \frac{X_{KL}}{X_S} \right\rangle = 7(\text{SD} = 14)$. For the broad component (dashed line) we obtain $\left\langle \frac{X_{KL}}{X_S} \right\rangle = 0.3(\text{SD} = 0.5)$.

Given that the best match to the abundances in the narrow component of Orion-S is the ER of Orion-KL, it seems as though these species/components do indeed trace quiescent gas. In particular, it probably is the same gas out of which both star forming regions have been formed. The broad component of Orion-S, however, seems better matched to the CR and Plateau of Orion-KL. Figures 16 to 19 only have a few broad component points and, therefore, it is difficult to make any strong statistical arguments based on these data alone. However, this evidence along with the chemical abundance analysis presented in Section 3.3.1 provide fairly strong support for the idea that shocks have also had an influence on the chemistry of Orion-S.

3.3.3 Species Detected in Orion-KL but not in Orion-S—It is well known that Orion-KL has an incredibly rich molecular chemistry (e.g. Schilke et al. 1997a; Comito et al. 2005; Olofsson et al. 2007; Persson et al. 2007; Leurini et al. 2006; Tercero et al. 2005).

However, it is possible that the species that were detected in Orion-KL, but not in Orion-S, exist in the latter source, but at levels too weak to be detected. Some of these species might be observable with ALMA at lower frequencies. In this Section, we explore this possibility by providing upper limits for the abundances of all the species detected in Orion-KL by Crockett et al. (2014) but not detected in Orion-S.

Modeling was accomplished by fixing T_{ex} , V_{FWHM} , Ω , and V_{LSR} and finding the column density that produced transitions whose intensities were $< 3\sigma$ across all the HEXOS bands. Since we were able to model all of our species using, at most, two components, we determine two different column density upper limits: one assuming that the undetected emission arises from the narrow component and assuming that it originates in the broad component. For the narrow component, we used fixed values of $T_{ex} = 40\text{K}$, $V_{FWHM} = 4\text{ km s}^{-1}$, $\Omega = 60''$, and $V_{LSR} = 7.1$, which were found to be typical for the narrow component (see Tables 5 and 6). For the broad component, we used fixed values of $T_{ex} = 80\text{K}$, $V_{FWHM} = 8\text{ km s}^{-1}$, $\Omega = 40''$, and $V_{LSR} = 7.1$, which were found to be typical for the broad component (see Table 6). Results are listed in Table 8. Column 1 is the species name, column 2 the upper limit total column density assuming the gas arises in the narrow component, column 3 the upper limit total column density assuming the gas originates in the broad component, and column 4 lists the maximum upper state energy for the model (i.e. no transitions with $E > E_{up}$ were modeled). Different values of E_{up} were used for different molecules to keep the number of modeled transitions to a reasonable value.

There are also a number of species that we detected ($S/N > 3\sigma$), but did not model, since their S/N was $< 5\sigma$. Using the same assumptions as for the undetected species we provide upper limits for the abundances for these species in Table 9. The column density limits listed in Table 9 are approximately an order of magnitude or more smaller than the column densities of the same species detected in Orion-KL (Crockett et al. 2014).

A possible question is whether the species listed in Table 8 could actually exist in Orion-S even though they are undetected. We inspect the excitation conditions of these species, examining E_{up} of all possible transitions, to determine whether they are detectable given the reported noise of the HIFI bands. A portion of these species have E_{up} much greater than 500 K (e.g. $\text{H}_2\text{O } v_2$, $\text{H}^{13}\text{CN } v_2 = 1$, HC_3N , $\text{HC}_3\text{N } v=0$, $\text{HCN } v_2 = 1$, $\text{HCN } v_2 = 2$, OCS , etc.). Based on the analysis done in this paper, Orion-S can barely excite species with $E_{up} > 500\text{ K}$. Therefore, transitions of these species would not be observed above the noise, even if they were present. In addition, there are some complex organic species with transition of $E_{up} < 100\text{ K}$ which we also did not detect (e.g. CH_2NH , CH_2DOH , CH_2NH , CH_3OCHO , etc.). This is not surprising given the absence of hot core chemistry in Orion-S.

4 Summary and Conclusion

We have presented results from a comprehensive spectral survey toward Orion South, taken with the HIFI instrument aboard the *Herschel Space Observatory* covering the frequency range 480 to 1900 GHz with a resolution of 1.1 MHz. We detected 685 spectral lines with $S/N > 3\sigma$ originating from 52 different molecular and atomic species. Using the CASSIS spectral line analysis software package, we modeled each of the detected species assuming

conditions of Local Thermodynamic Equilibrium. Based on this modeling, we found evidence for three different cloud components: a cool ($T_{ex} \sim 20 - 40$ K), spatially extended ($> 60''$), and quiescent ($V_{FWHM} \sim 4 \text{ km s}^{-1}$) component; a warmer ($T_{ex} \sim 80 - 100$ K), less spatially extended ($\sim 30''$), and more dynamic ($V_{FWHM} \sim 8 \text{ km s}^{-1}$) component, which is likely affected by embedded outflows; and a kinematically distinct region dominated by emission from species which trace UV irradiation. Indirect evidence to support the existence of the first two components can be inferred from McMullin et al. (1993) who mapped the region in a few spectral lines (SiO, H^{13}CO^+ , SO_2 , CH_3OH , and HC_3N) with the BIMA array. Their H^{13}CO^+ and HC_3N data confirm the existence of a fairly extended ($\sim 1'$) quiescent ($\text{FWHM} \sim 3 \text{ km s}^{-1}$) component, whereas the SO_2 and CH_3OH data reveal a smaller emitting region ($\sim 20''$) of warm gas (~ 75 K). While the spectra for the latter two species are too weak to determine line widths, their SiO data reveal a similarly small region (offset by only a few arc seconds from the SO_2 and CH_3OH emission peaks) with broad line widths ($\sim 7 \text{ km s}^{-1}$). In addition, McMullin et al. (1993) reports column densities of SO_2 and H^{13}CO^+ of $< 2 \times 10^{-10}$ and 4×10^{-11} respectively which compare favourably to the values reported in Table 7. Finally, while there are no higher resolution observations to confirm the existence of the third component (i.e. the UV irradiated region), since CO^+ is only ever detected in PDRs, its presence in our data strongly suggests that such a component must exist.

We also presented a comprehensive chemical abundance comparison between Orion-KL and Orion-S; two star forming regions that potentially formed from the same natal molecular gas but are at different evolutionary stages. Based on a paucity of complex molecules in Orion-S, we found little chemical evidence for the existence of a significant “hot core” component. This is likely due to the fact that either the hot cores associated with the embedded star formation have either not had sufficient time to develop chemically, or that they are simply too small for their line emission to be detected in the large Herschel beam, or that Orion-S is not a massive star forming region and hot cores massive enough to produce their characteristic rich spectra simply do not exist. The presence of a number of UV tracers such as $[\text{CII}]$, $[\text{CI}]$, CH , CH^+ , SH^+ , CO^+ , and the fact that transitions of these species have velocities that are $1\text{--}1.5 \text{ km s}^{-1}$, higher than those of the quiescent gas, suggest that these species arise from a kinematically distinct PDR; most likely the UV illuminated surface of the cloud. The best match to the chemical abundances in the cooler, quiescent gas in Orion-S is with the quiescent extended ridge of Orion-KL, indicating that most of the gas in Orion-S is still quiescent as well, and relatively unaffected by higher temperature or UV driven chemistry. The best agreement with the warmer, broad component of Orion-S is with the Orion-KL Plateau and Compact Ridge regions, suggesting that shocks have had an influence on the overall chemistry in Orion-S.

Acknowledgements

HIFI was designed and built by a consortium of institutes and university departments from across Europe, Canada and the United States under the leadership of SRON Netherlands Institute for Space Research, Groningen, The Netherlands and with major contributions from Germany, France and the US. Consortium members are: Canada: CSA, U. Waterloo; France: CESR, LAB, LERMA, IRAM; Germany: KOSMA, MPIfR, MPS; Ireland, NUI Maynooth; Italy: ASI, IFSI-INAF, Osservatorio Astrofisico di Arcetri-INAF; Netherlands: SRON, TUD; Poland: CAMK, CBK; Spain: Observatorio Astronómico Nacional (IGN), Centro de Astrobiología (CSIC-INTA). Sweden: Chalmers University of Technology - MC2, RSS & GARD; Onsala Space Observatory; Swedish National Space

Board, Stockholm University - Stockholm Observatory; Switzerland: ETH Zurich, FHNW; USA: Caltech, JPL, NHSC. We also need to acknowledge the support by the Deutsche Forschungs-gemeinschaft (DFG) via the collaborative research grant SFB 956, project C1 & C3, as well as the ERC and the Spanish MINECO for funding support under grants ERC-2013-Syg-610256 and AYA2012-32032. Support for this work was provided, in part, by a National Sciences and Engineering Research Council of Canada (NSERC) grant to R. Plume and K. Tahani and by NASA through an award issued by JPL/Caltech. This work was carried out in part at the Jet Propulsion Laboratory, which is operated for NASA by the California Institute of Technology.

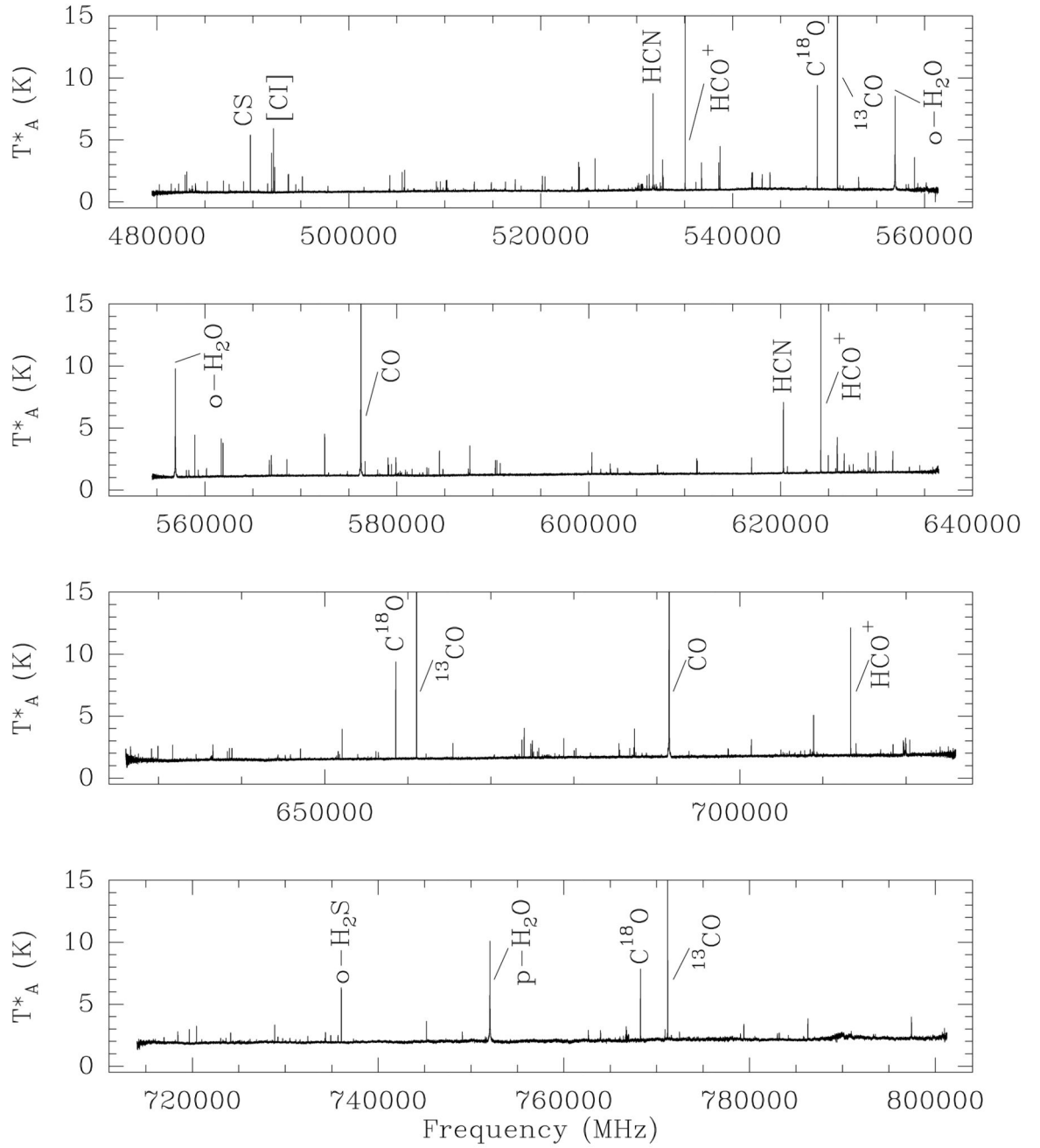
Facilities: Herschel.

References

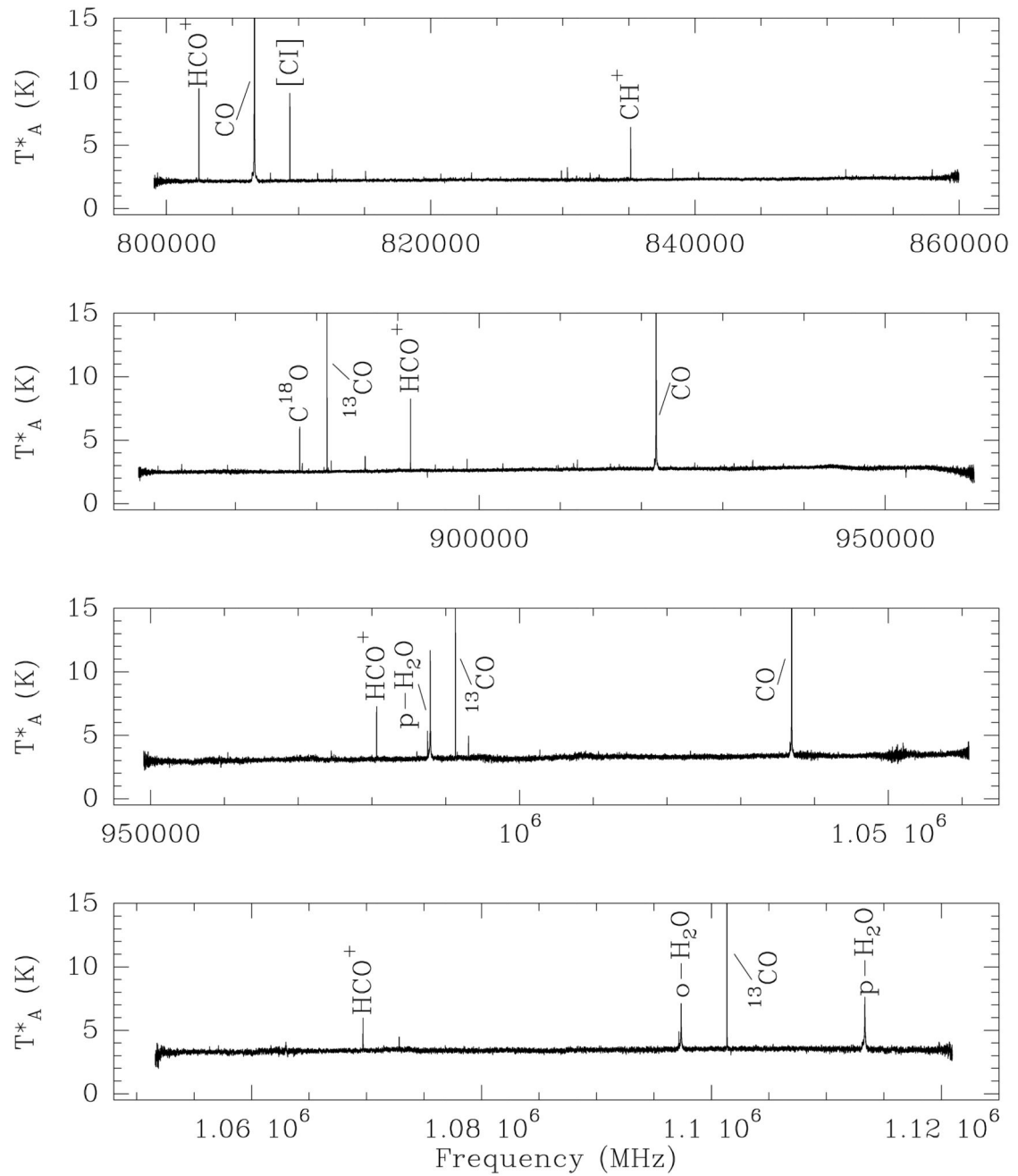
- Anders E, Grevesse N. *Geochim Cosmochim Acta*. 1989; 53:197.
- Bachiller R, Pérez Gutiérrez M. *ApJ*. 1997; 487:L93.
- Bally J, O'Dell CR, McCaughrean MJ. *AJ*. 2000; 119:2919.
- Bally J, Zinnecker H. *AJ*. 2005; 129:2281.
- Bergin EA, Goldsmith PF, Snell RL, Ungerechts H. *ApJ*. 1994; 431:674.
- Bergin EA, Phillips TG, Comito C, Crockett NR, Lis DC, Schilke P, Wang S, Bell TA, Blake GA, Bumble B, Caux E, et al. *A&A*. 2010; 521:L20.
- Beuther H, Zhang Q, Greenhill LJ, Reid MJ, Wilner D, Keto E, Shinnaga H, Ho PTP, Moran JM, Liu S-Y, Chang C-M. *ApJ*. 2005; 632:355.
- Blake GA, Sutton EC, Masson CR, Phillips TG. *ApJ*. 1987; 315:621.
- Ceccarelli C, Caselli P, Herbst E, Tielens AGGM, Caux E. *Protostars and Planets V*. 2007:47.
- Ceccarelli C, Hollenbach DJ, Tielens AGGM. *ApJ*. 1996; 471:400.
- Choi Y, van der Tak FFS, Bergin EA, Plume R. *A&A*. 2014; 572:L10.
- Comito C, Schilke P. *A&A*. 2002; 395:357.
- Comito C, Schilke P, Phillips TG, Lis DC, Motte F, Mehringer D. *ApJS*. 2005; 156:127.
- Crockett NR, Bergin EA, Neill JL, Favre C, Schilke P, Lis DC, Bell TA, Blake G, Cernicharo J, Emprechtinger M, Esplugues GB, et al. *ApJ*. 2014; 787:112.
- Crockett NR, Bergin EA, Wang S, Lis DC, Bell TA, Blake GA, Boogert A, Bumble B, Cabrit S, Caux E, Ceccarelli C, et al. *A&A*. 2010; 521:L21.
- de Graauw T, Helmich FP, Phillips TG, Stutzki J, Caux E, Whyborn ND, Dieleman P, Roelfsema PR, Aarts H, Assendorp R, Bachiller R, et al. *A&A*. 2010; 518:L6.
- Draine BT, Bertoldi F. *ApJ*. 1996; 468:269.
- Esplugues GB, Tercero B, Cernicharo J, Goicoechea JR, Palau A, Marcelino N, Bell TA. *A&A*. 2013; 556:A143.
- Federman SR, Rawlings JMC, Taylor SD, Williams DA. *MNRAS*. 1996; 279:L41.
- Fuente A, Martín-Pintado J, Cernicharo J, Bachiller R. *A&A*. 1993; 276:473.
- Furlan E, Hartmann L, Calvet N, D'Alessio P, Franco-Hernández R, Forrest WJ, Watson DM, Uchida KI, Sargent B, Green JD, Keller LD, et al. *ApJS*. 2006; 165:568.
- Garrod RT, Herbst E. *A&A*. 2006; 457:927.
- Garrod RT, Weaver SLW, Herbst E. *ApJ*. 2008; 682:283.
- Gerin M, de Luca M, Goicoechea JR, Herbst E, Falgarone E, Godard B, Bell TA, Coutens A, Kąmierzak M, Sonnentrucker P, Black JH, et al. *A&A*. 2010; 521:L16.
- Godard B, Falgarone E, Gerin M, Lis DC, De Luca M, Black JH, Goicoechea JR, Cernicharo J, Neufeld DA, Menten KM, Emprechtinger M. *A&A*. 2012; 540:A87.
- Goicoechea JR, Teyssier D, Etzaluze M, Goldsmith PF, Ossenkopf V, Gerin M, Bergin EA, Black JH, Cernicharo J, Cuadrado S, Encrenaz P, et al. *ApJ*. 2015; 812:75.
- Goldsmith PF, Langer WD. *ApJ*. 1978; 222:881.
- Goldsmith PF, Bergin EA, Lis DC. *ApJ*. 1997; 491:615.
- Groesbeck, TD. PhD thesis, CALIFORNIA INSTITUTE OF TECHNOLOGY; 1995.
- Guan Y, Krone SM. 2007
- Gusdorf A, Cabrit S, Flower DR, Pineau Des Forêts G. *A&A*. 2008a; 482:809.

- Gusdorf A, Pineau Des Forêts G, Cabrit S, Flower DR. A&A. 2008b; 490:695.
- Hastings WK. Biometrika. 1970; 57:97.
- Herbst E, van Dishoeck EF. ARA&A. 2009; 47:427.
- Herrmann F, Madden SC, Nikola T, Poglitsch A, Timmermann R, Geis N, Townes CH, Stacey GJ. ApJ. 1997; 481:343.
- Hollenbach DJ, Tielens AGGM. ARA&A. 1997; 35:179.
- Iglesias ER, Silk J. ApJ. 1978; 226:851.
- Kama M, López-Sepulcre A, Dominik C, Ceccarelli C, Fuente A, Caux E, Higgins R, Tielens AGGM, Alonso-Albi T. A&A. 2013; 556:A57.
- Ka mierzczak-Barthel M, Semenov DA, van der Tak FFS, Chavarría L, van der Wiel MHD. A&A. 2015; 574:A71.
- Kurtz S, Cesaroni R, Churchwell E, Hofner P, Walmsley CM. Protostars and Planets IV. 2000; 299.
- Ladd EF. ApJ. 2004; 610:320.
- Langer WD, Velusamy T, Pineda JL, et al. A&A. 2010; 521:L17.
- Leurini S, Rolffs R, Thorwirth S, Parise B, Schilke P, Comito C, Wyrowski F, Güsten R, Bergman P, Menten KM, Nyman L-Å. A&A. 2006; 454:L47.
- Lucas R, Liszt H. A&A. 1998; 337:246.
- Mangum JG, Wootten A. ApJS. 1993; 89:123.
- Mangum JG, Wootten A, Plambeck RL. ApJ. 1993; 409:282.
- Martin-Pintado J, Bachiller R, Fuente A. A&A. 1992a; 254:315.
- Martin-Pintado J, Bachiller R, Fuente A. A&A. 1992b; 254:315.
- McMullin JP, Mundy LG, Blake GA. ApJ. 1993; 405:599.
- Menten KM, Reid MJ, Forbrich J, Brunthaler A. A&A. 2007; 474:515.
- Menten KM, Wyrowski F. Springer Tracts in Modern Physics. 2011; 241:27.
- Mezger PG, Zylka R, Wink JE. A&A. 1990; 228:95.
- Millar TJ, Herbst E. A&A. 1990; 231:466.
- Mookerjee B, Ossenkopf V, Ricken O, et al. A&A. 2012; 542:L17.
- Müller M, Jellema W, Olberg M, Moreno R, Teyssier D. The HIFI Beam: Release #1 Release Note for Astronomers. 2014; 1.1:1.
- Müller HSP, Schlöder F, Stutzki J, Winnewisser G. Journal of Molecular Structure. 2005; 742:215.
- Nagy Z, Ossenkopf V, Van der Tak FFS, Faure A, Makai Z, Bergin EA. A&A. 2015; 578:A124.
- Nagy Z, Van der Tak FFS, Ossenkopf V, Gerin M, Le Petit F, Le Bourlot J, Black JH, Goicoechea JR, Joblin C, Röllig M, Bergin EA. A&A. 2013; 550:A96.
- Neill JL, Bergin EA, Lis DC, Schilke P, Crockett NR, Favre C, Emprechtinger M, Comito C, Qin S-L, Anderson DE, Burkhardt AM, et al. ApJ. 2014; 789:8.
- Nummelin A, Bergman P, Hjalmarson Å, Friberg P, Irvine WM, Millar TJ, Ohishi M, Saito S. ApJS. 1998; 117:427.
- O'Dell CR, Harris JA. AJ. 2010; 140:985.
- Olofsson AOH, Persson CM, Koning N, Bergman P, Bernath PF, Black JH, Frisk U, Geppert W, Hasegawa TI, Hjalmarson Å, Kwok S, et al. A&A. 2007; 476:791.
- Ott, S. Astronomical Society of the Pacific Conference Series, Vol. 434, Astronomical Data Analysis Software and Systems XIX. Mizumoto, Y, Morita, K-I, Ohishi, M, editors. 2010. 139.
- Pan K, Federman SR, Welty DE. ApJ. 2001; 558:L105.
- Papadopoulos PP, Thi W-F, Viti S. MNRAS. 2004; 351:147.
- Parise B, Leurini S, Schilke P, Roueff E, Thorwirth S, Lis DC. A&A. 2009; 508:737.
- Pearson, JC; Drouin, BJ; Pickett, HM. IAU Symposium; IAU Symposium; 2005. 270.
- Persson CM, Olofsson AOH, Koning N, Bergman P, Bernath P, Black JH, Frisk U, Geppert W, Hasegawa TI, Hjalmarson Å, Kwok S, et al. A&A. 2007; 476:807.
- Pilbratt GL, Riedinger JR, Passvogel T, Crone G, Doyle D, Gageur U, Heras AM, Jewell C, Metcalfe L, Ott S, Schmidt M. A&A. 2010; 518:L1.

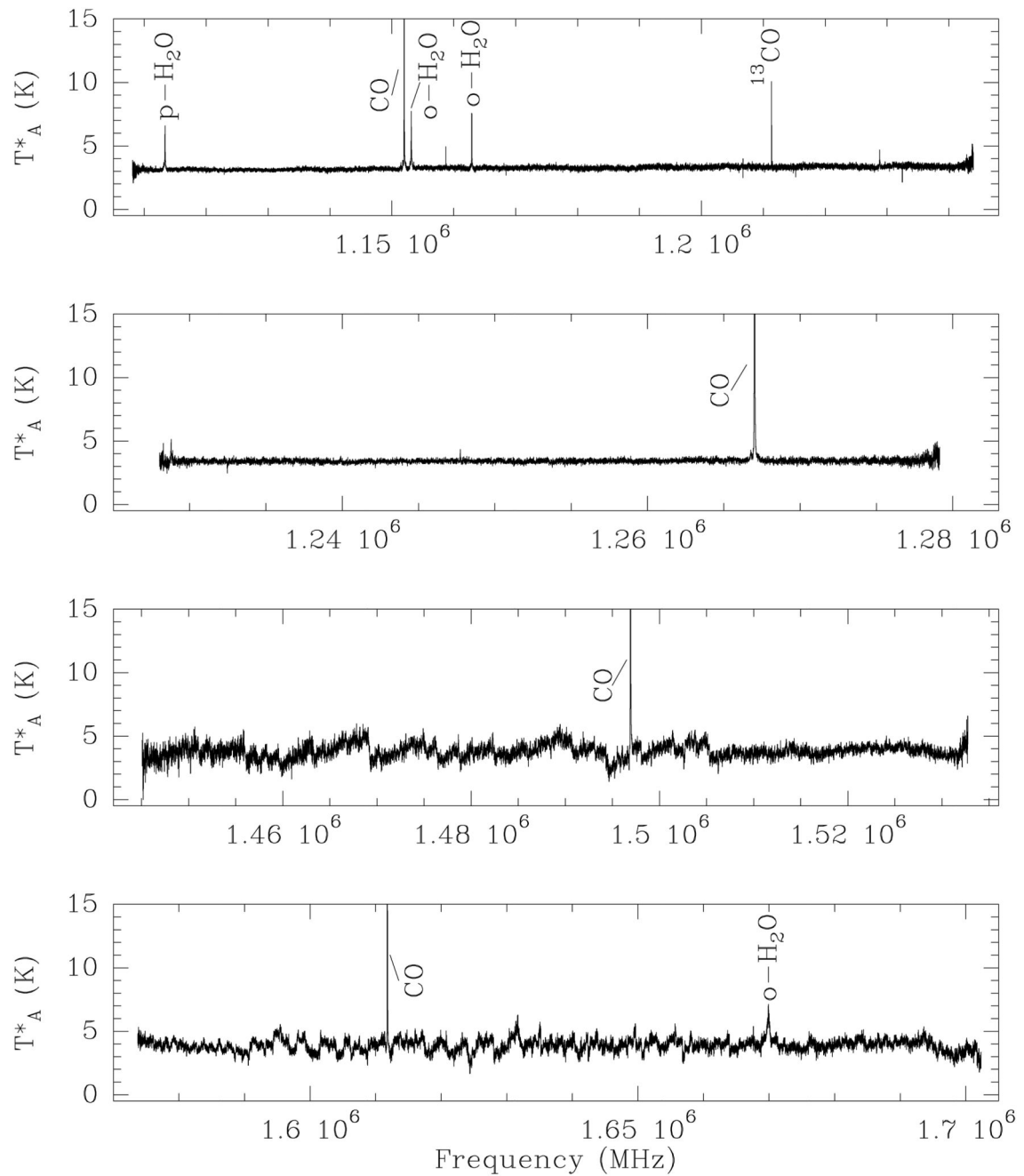
- Plume R, Bergin EA, Phillips TG, Lis DC, Wang S, Crockett NR, Caux E, Comito C, Goldsmith PF, Schilke P. *ApJ*. 2012; 744:28.
- Plume R, Jaffe DT, Evans NJ II. *ApJS*. 1992; 78:505.
- Plume R, Jaffe DT, Tatematsu K, Evans NJ II, Keene J. *ApJ*. 1999; 512:768.
- Porter JM, Oudmaijer RD, Baines D. *A&A*. 2004; 428:327.
- Roberts GO, Gelman A, Gilks WR. *The Annals of Applied Probability*. 1997; 7:110.
- Roelfsema PR, Helmich FP, Teyssier D, Ossenkopf V, Morris P, Olberg M, Shipman R, Risacher C, Akyilmaz M, Assendorp R, Avruch IM, et al. *A&A*. 2012; 537:17.
- Schilke P, Benford DJ, Hunter TR, Lis DC, Phillips TG. *ApJS*. 2001; 132:281.
- Schilke P, Groesbeck TD, Blake GA, Phillips TG. *ApJS*. 1997a; 108:301.
- Schilke P, Walmsley CM, Pineau des Forets G, Flower DR. *A&A*. 1997b; 321:293.
- Schmid-Burgk J, Guesten R, Mauersberger R, Schulz A, Wilson TL. *ApJ*. 1990; 362:L25.
- Shetty R, Kauffmann J, Schnee S, Goodman AA, Ercolano B. *ApJ*. 2009; 696:2234.
- Tauber JA, Goldsmith PF. *ApJ*. 1990; 356:L63.
- Tercero B, Cernicharo J, Pardo JR. *IAU Symposium*; *IAU Symposium*; 2005. 203
- Tercero B, Cernicharo J, Pardo JR, Goicoechea JR. *A&A*. 2010; 517:A96.
- Tielens AGGM, Hollenbach D. *Icarus*. 1985; 61:40.
- Thayer MR. *ApJ*. 1997; 482:792.
- van der Tak FFS, Black JH, Schöier FL, Jansen DJ, van Dishoeck EF. *A&A*. 2007; 468:627.
- Velusamy T, Langer WD, Pineda JL, Goldsmith PF. *A&A*. 2012; 541:L10.
- Wang S, Bergin EA, Crockett NR, Goldsmith PF, Lis DC, Pearson JC, Schilke P, Bell TA, Comito C, Blake GA, Caux E, et al. *A&A*. 2011; 527:95.
- Watson, WD, Walmsley, CM. *Astrophysics and Space Science Library* Regions of Recent Star Formation. Roger, RS, Dewdney, PE, editors. Vol. 93. 1982. 357–376.
- Williams JP, Bergin EA, Caselli P, Myers PC, Plume R. *ApJ*. 1998; 503:689.
- Wootten A, Bozyan EP, Garrett DB, Loren RB, Snell RL. *ApJ*. 1980; 239:844.
- Zapata LA, Rodríguez LF, Ho PTP, Zhang Q, Qi C, Kurtz SE. *The Astrophysical Journal*. 2005; 630:L85.
- Zapata LA, Ho PTP, Rodríguez LF, O'Dell CR, Zhang Q, Muench A. *ApJ*. 2006; 653:398.
- Zapata LA, Schmid-Burgk J, Menten KM. *A&A*. 2011; 529:A24.
- Zernickel A, Schilke P, Schmiedeke A, Lis DC, Brogan CL, Ceccarelli C, Comito C, Emprechtinger M, Hunter TR, Möller T. *A&A*. 2012; 546:A87.
- Ziurys LM, Wilson TL, Mauersberger R. *ApJ*. 1990; 356:L25.

**Fig. 1.**

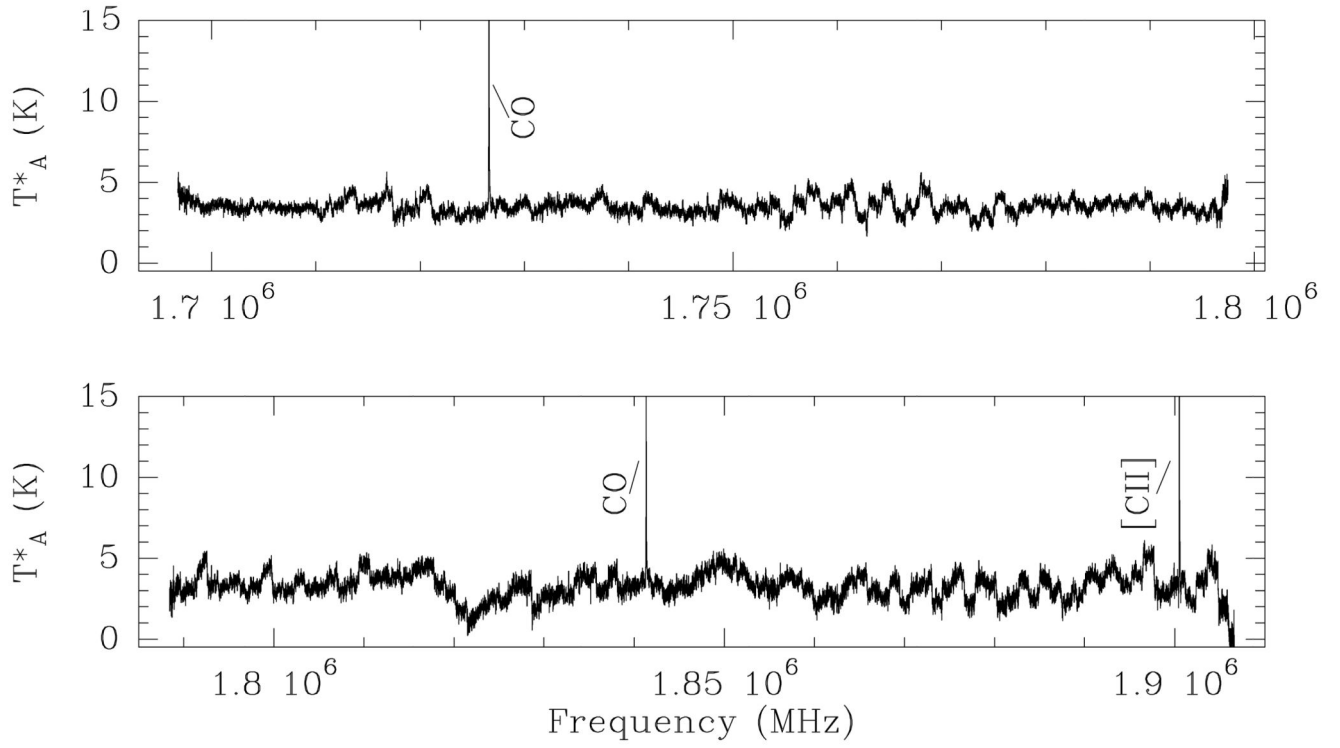
HEXOS/HIFI spectral scans of (from top to bottom) band 1a, band 1b, band 2a and band 2b after Hanning smoothing. Resolutions, noise levels, and smoothing factors for each band are listed in Table 1. Baselines are not subtracted and some of the strongest lines are labelled.

**Fig. 2.**

Same as Figure 1 except for band 3a, band 3b, band 4a and band 4b.

**Fig. 3.**

Same as Figure 1 except for band 5a, band 5b, band 6a and band 6b. The higher noise level in band 6 is due to the HEB mixers which produce higher noise in comparison with the SIS mixers used in the first five bands.

**Fig. 4.**

Same as Figure 1 except for band 7a, and band 7b. The higher noise level in band 7 is due to the HEB mixers which produce higher noise in comparison with the SIS mixers used in the first five bands.

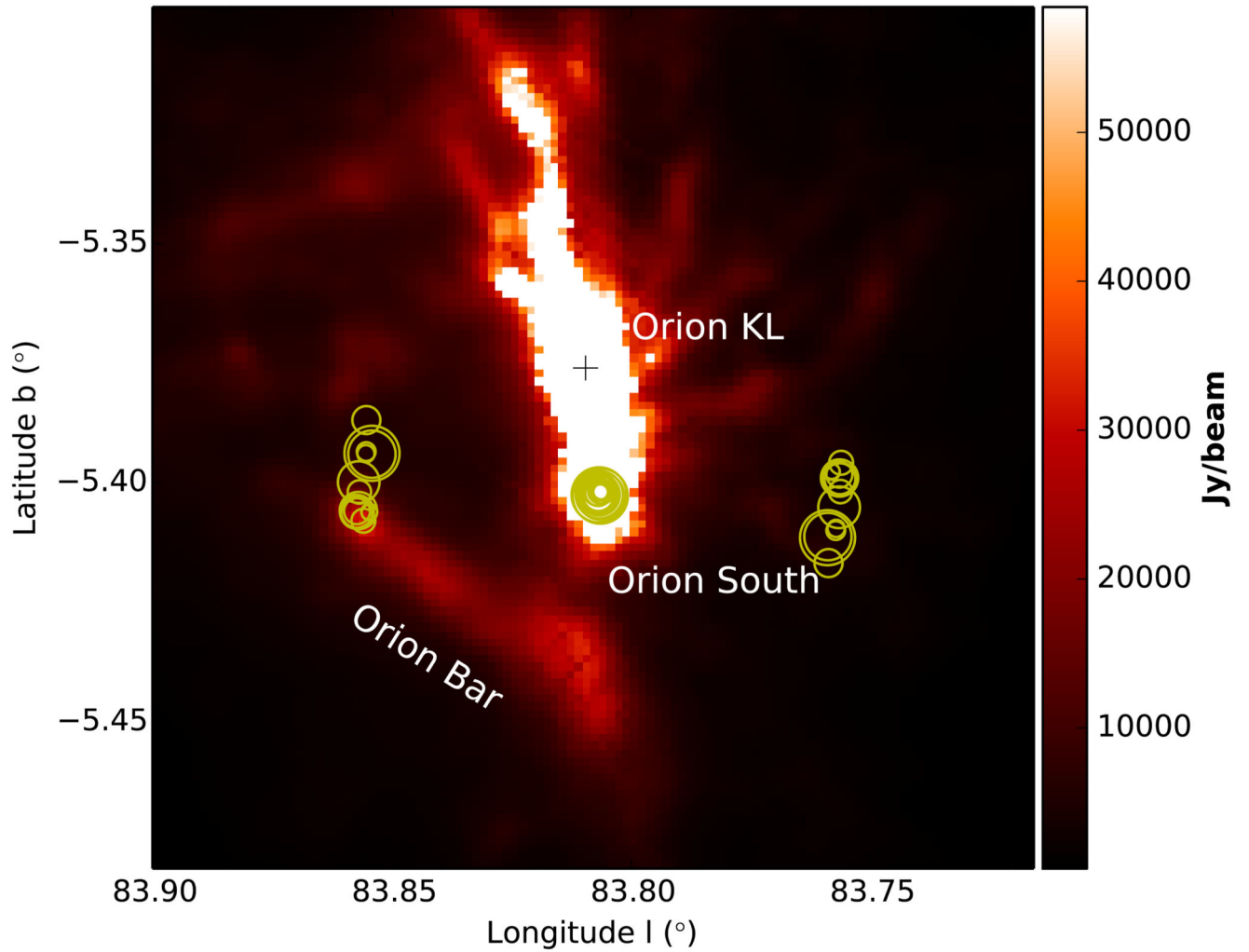


Fig. 5.

HEXOS Orion-S Observations: The circles indicate the beam positions with diameters corresponding to the FWHM at the center frequency of the HIFI bands. Circles near the center of the image (at $l \sim 83.81^\circ$) indicate the position of the spectral scan observations of Orion-S. Circles to the left and to the right (at $l \sim 83.86^\circ$ and 83.76° respectively) indicate the off position observations. The background shows the *Herschel*/SPIRE $250 \mu\text{m}$ dust emission in the Orion-KL region (white regions indicate saturated pixels). From the location of the beam circles near the Orion Bar, it is apparent that some of the observations see emission in at least one reference beam.

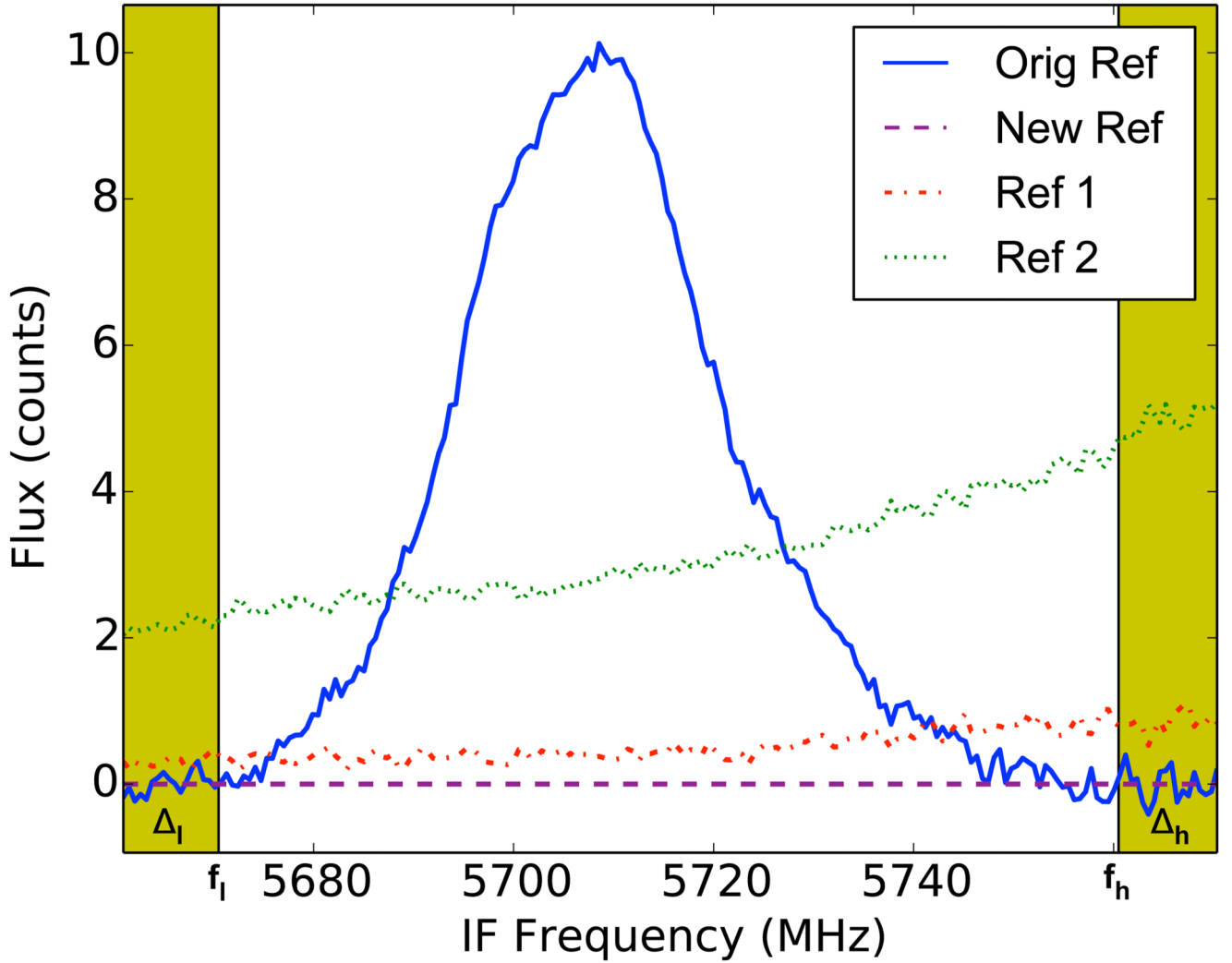


Fig. 6.

Removing the reference beam emission in the HEXOS Orion-S spectral scan: The blue solid line shows the emission in a reference beam. The red dashed and the green dotted lines show the references for an earlier scan and a later scan with slightly changed LO-settings, but covering the same IF interval. Averaging and scaling these reference scans using just the frequency ranges marked with green background results in the new reference spectrum, which replaces the old reference spectrum only in the frequency range shown (the total spectrum is still 4 GHz wide or ~ 1 GHz for each of the 4 HIFI WBS sub-bands). For display purposes we subtracted the new reference from all scans causing it to appear as a straight line.

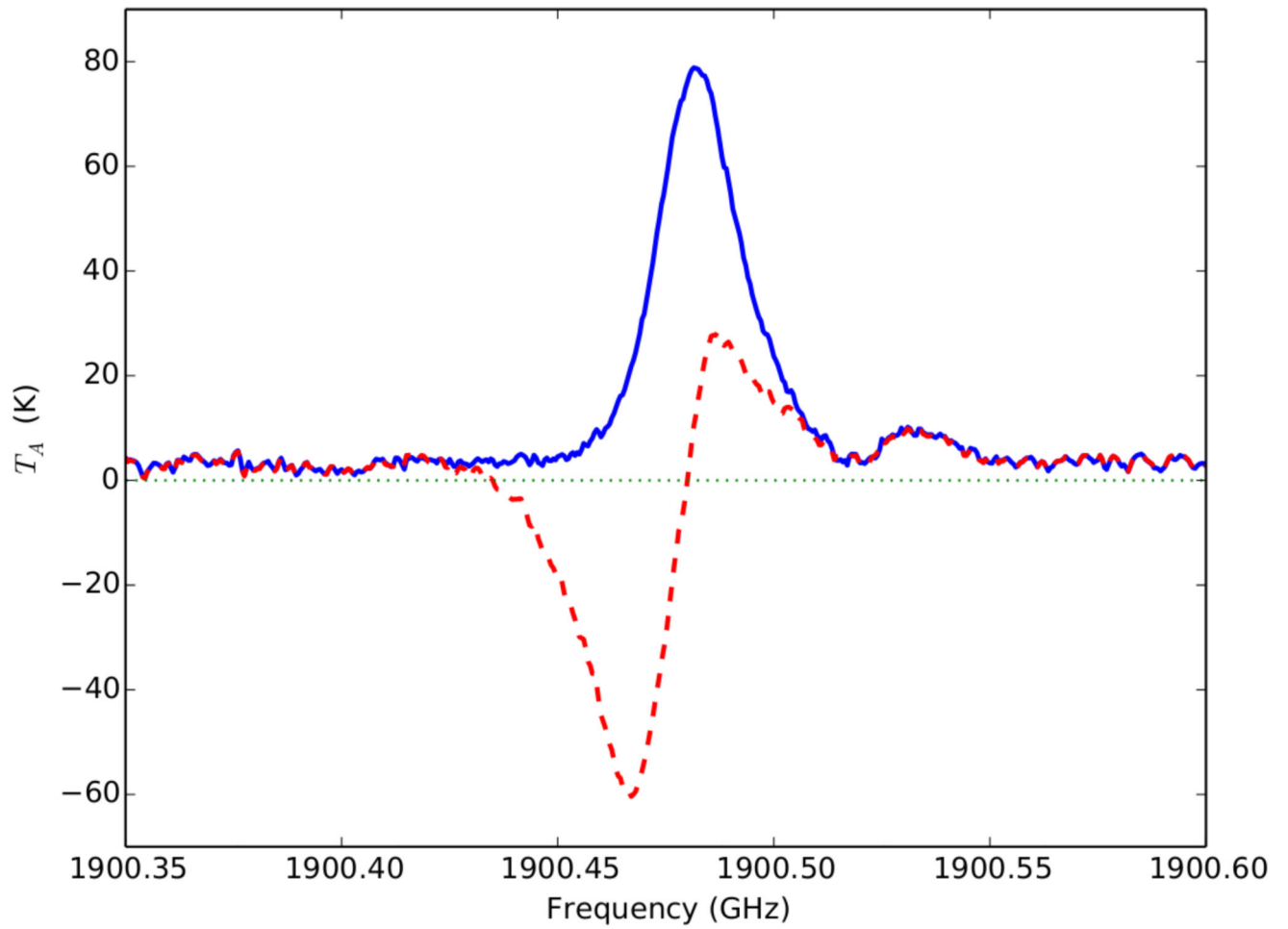
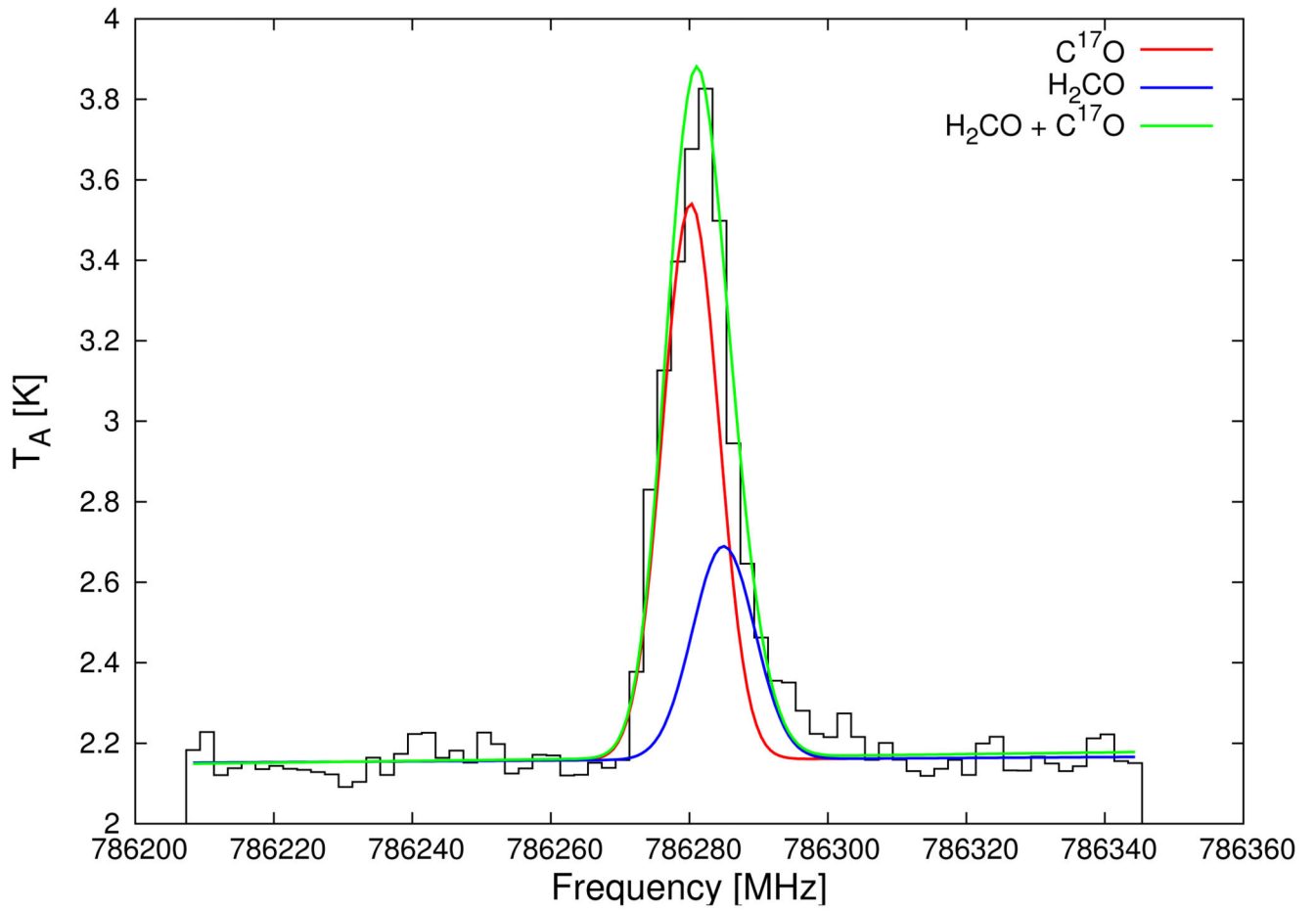
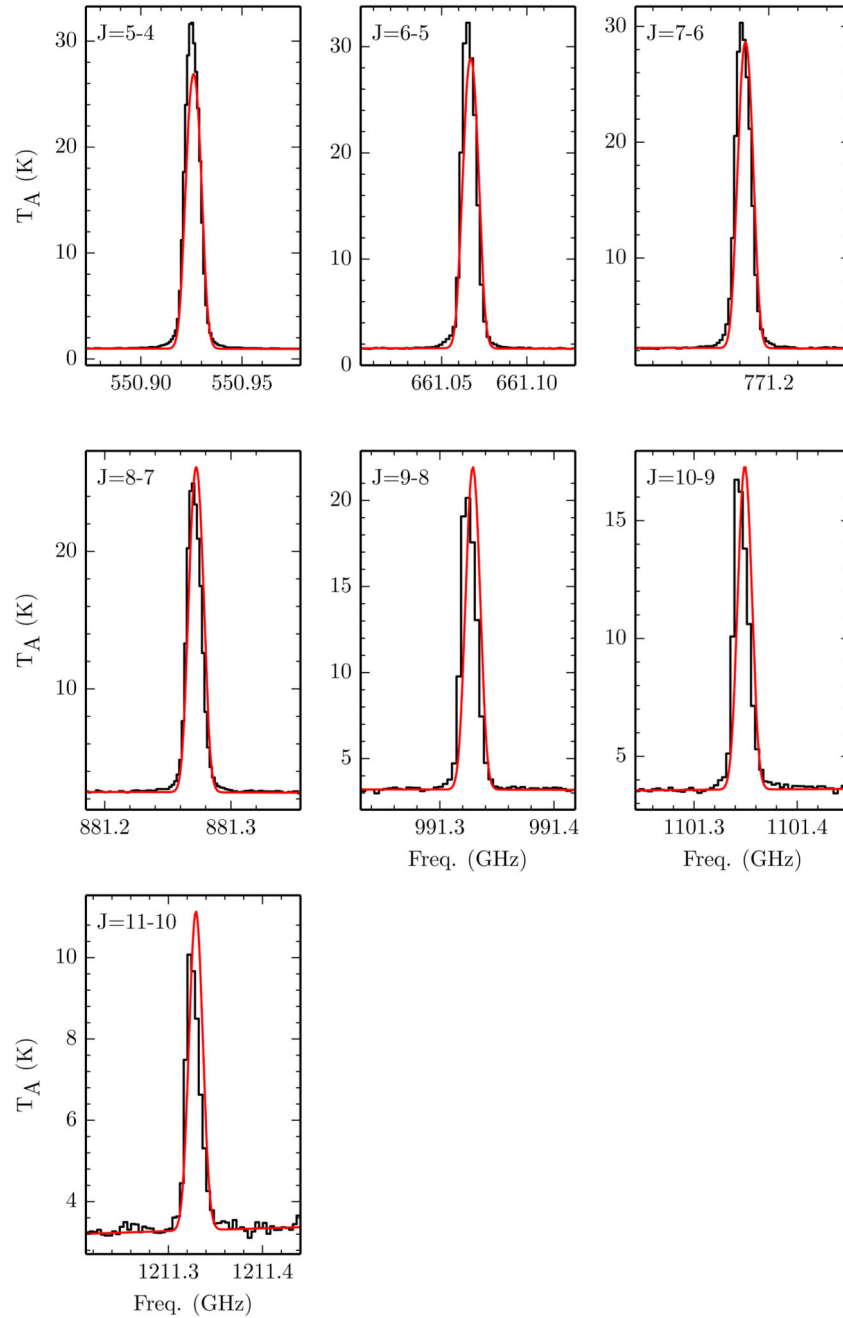


Fig. 7.

Example of the repaired [CII] line at 1900.526 GHz. The red dashed line shows the original result with emission in both reference beams and the blue solid line shows the result with the emission in the reference beams removed.

**Fig. 8.**

Example of a blended line at 786.3 GHz, produced by $C^{17}O$ and H_2CO . The red line shows the LTE modeled synthetic spectrum for $C^{17}O$ and the blue line shows that for H_2CO (Table 5 and 6). The green line is the superposition of these two components. Data are shown by the black histogram.

**Fig. 9.**

One component LTE modeling for ^{13}CO . Black histogram shows the data. Resulting model spectra are shown in red. LTE model parameters are provided in Table 5.

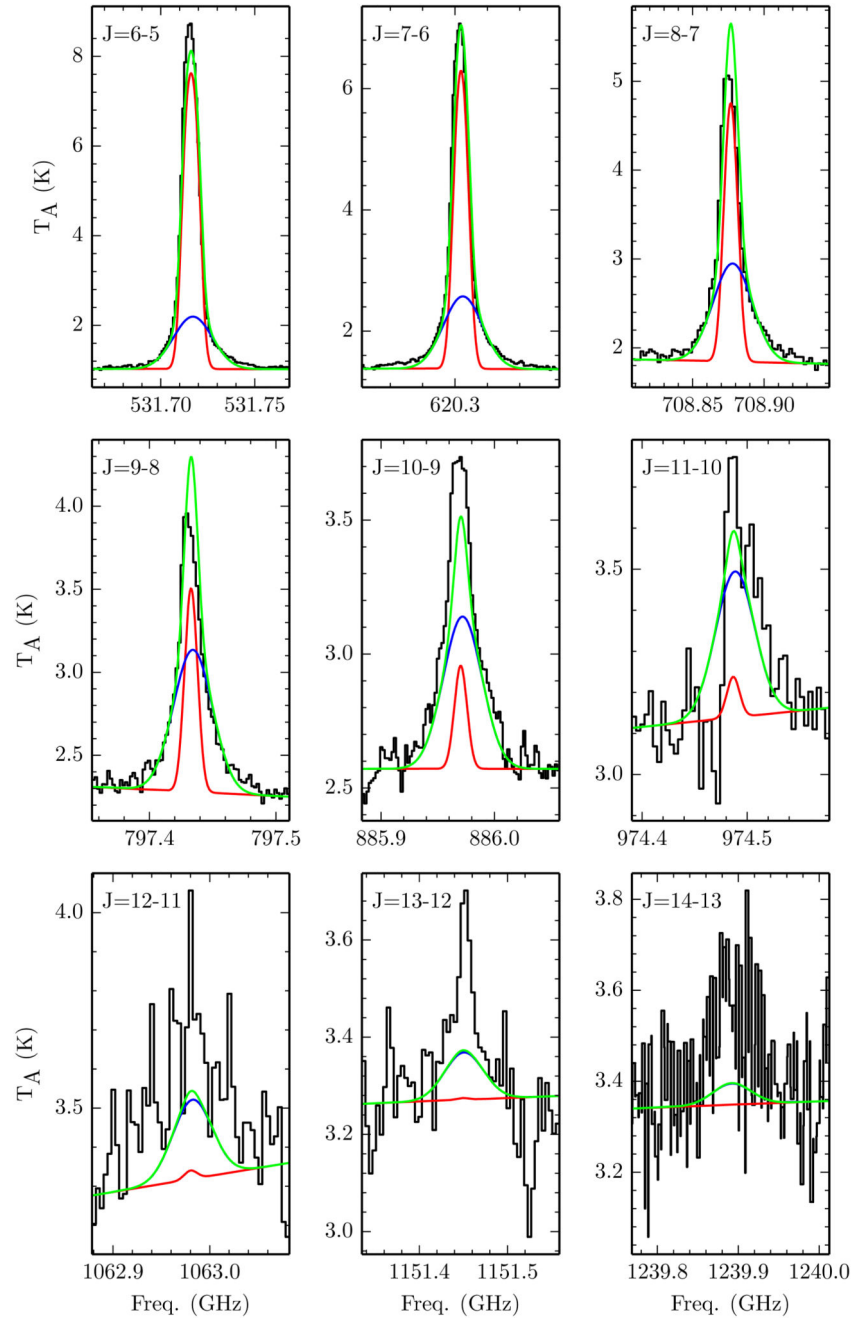


Fig. 10.

Two component LTE modeling for HCN. Black histogram shows the data. Models of the narrow and the broad components are shown by the red and blue lines respectively. The superposition of the two components is shown in green. LTE model parameters are provided in Table 6.

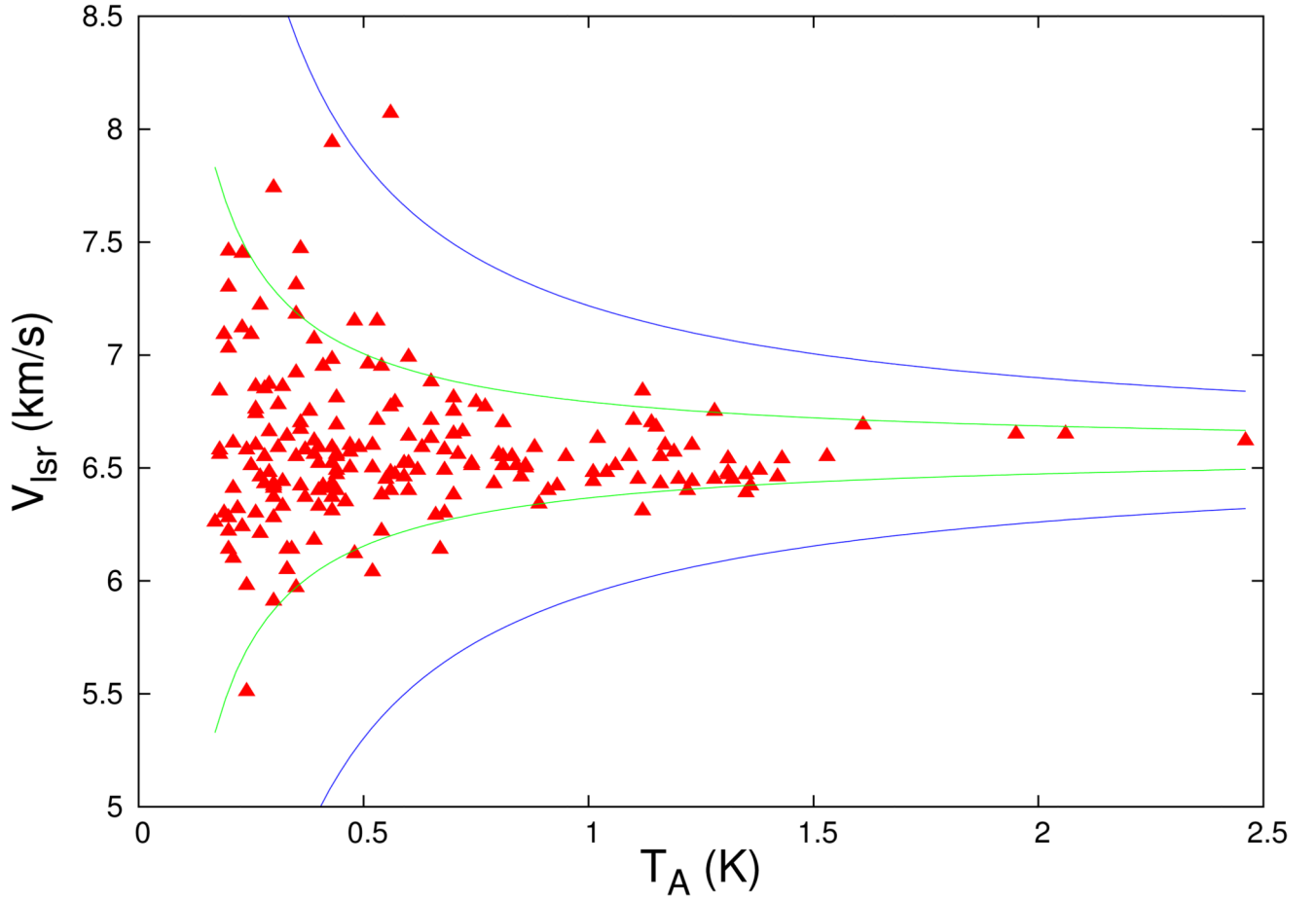


Fig. 11.

Plot of the measured V_{LSR} vs T_A derived from independent Gaussian fits to each of the A-CH₃OH and E-CH₃OH transitions listed in Table 4. The green and blue lines are the 1σ and 3σ (respectively) theoretical error envelope for the V_{LSR} determined from Gaussian fitting of noisy lines predicted by Porter et al. (2004). Curves are calculated assuming $\langle FWHM \rangle \sim 5 \text{ km s}^{-1}$ and $T_{rms} \sim 0.1 \text{ K}$ (typical values for methanol).

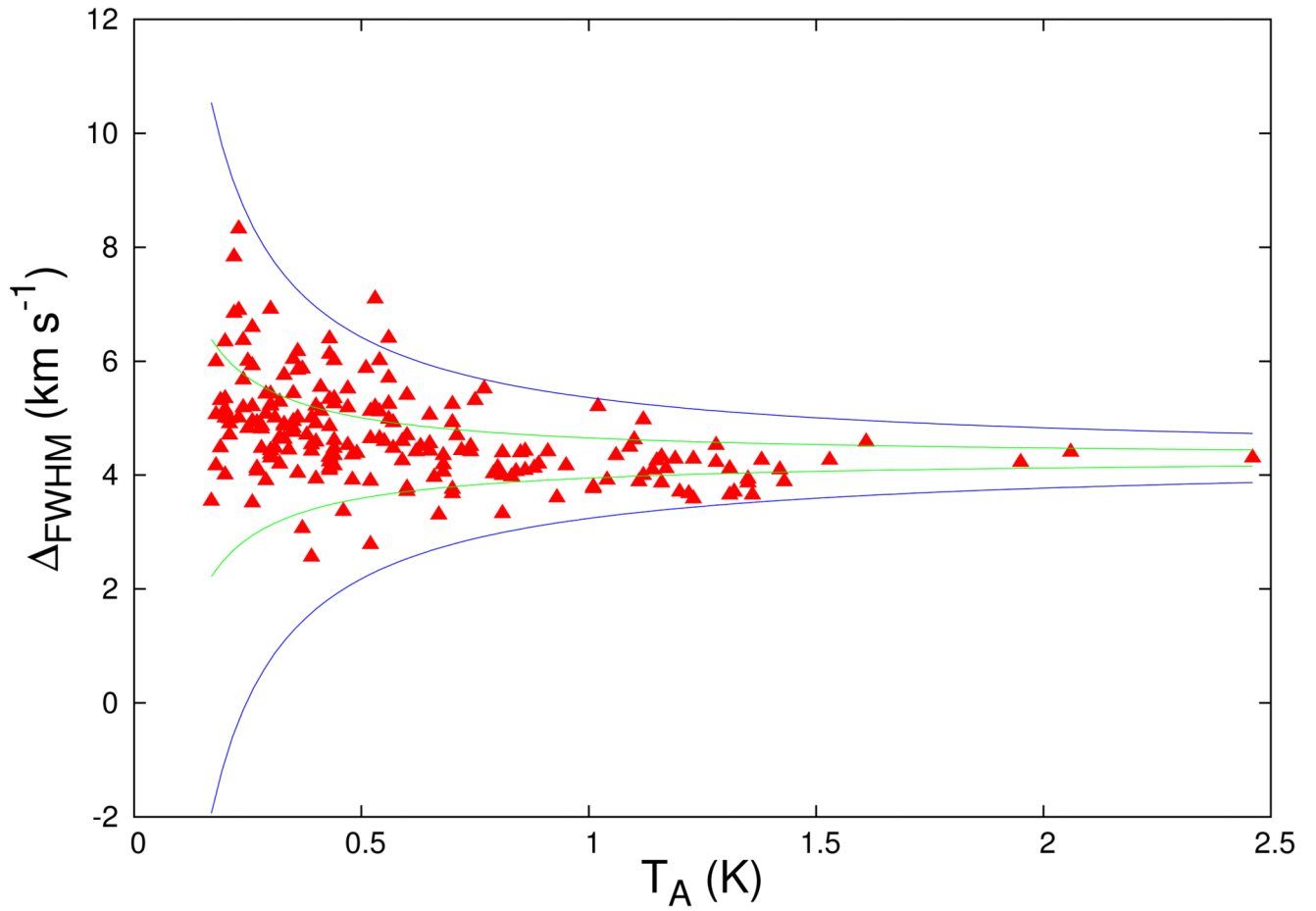
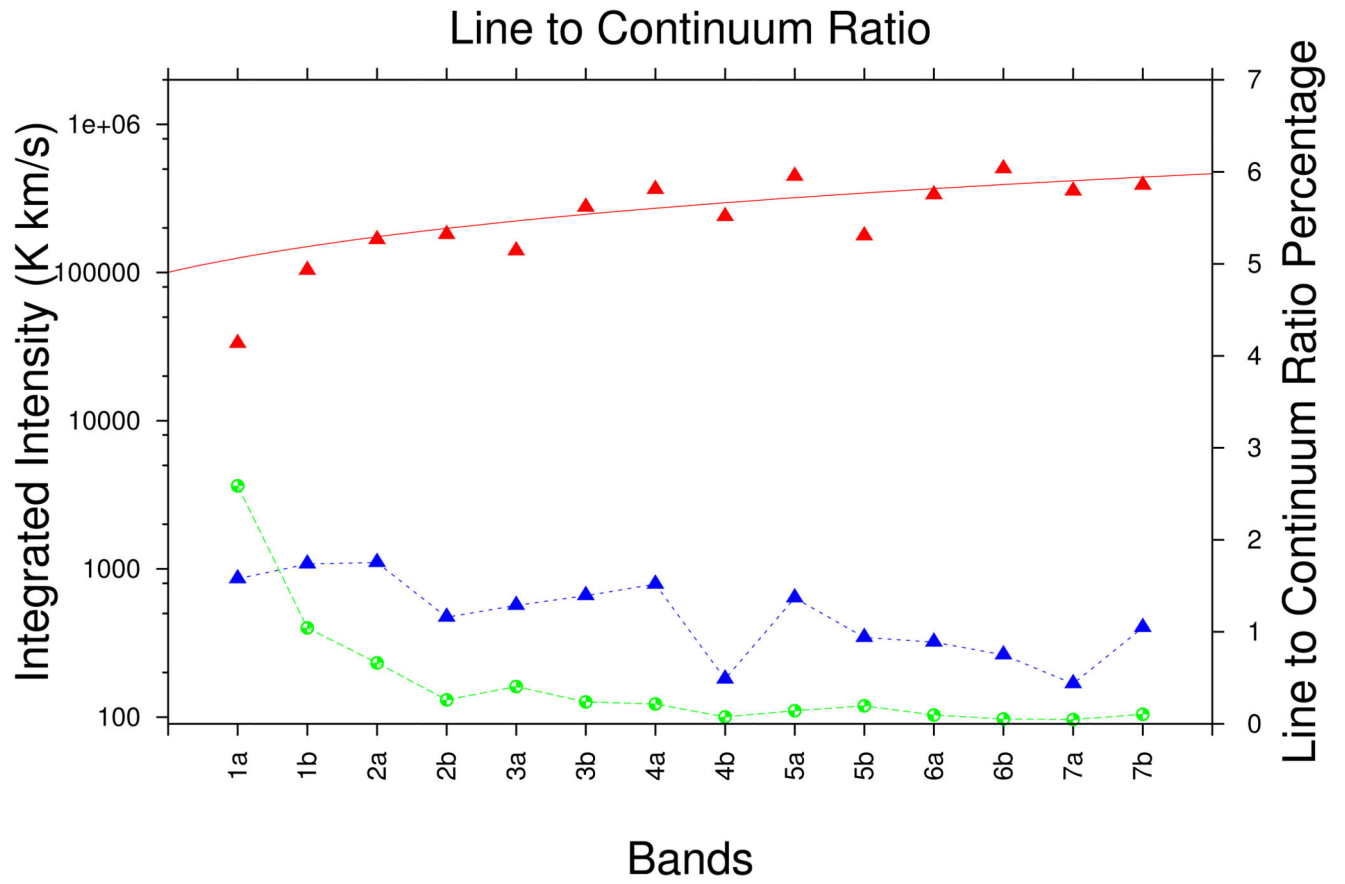
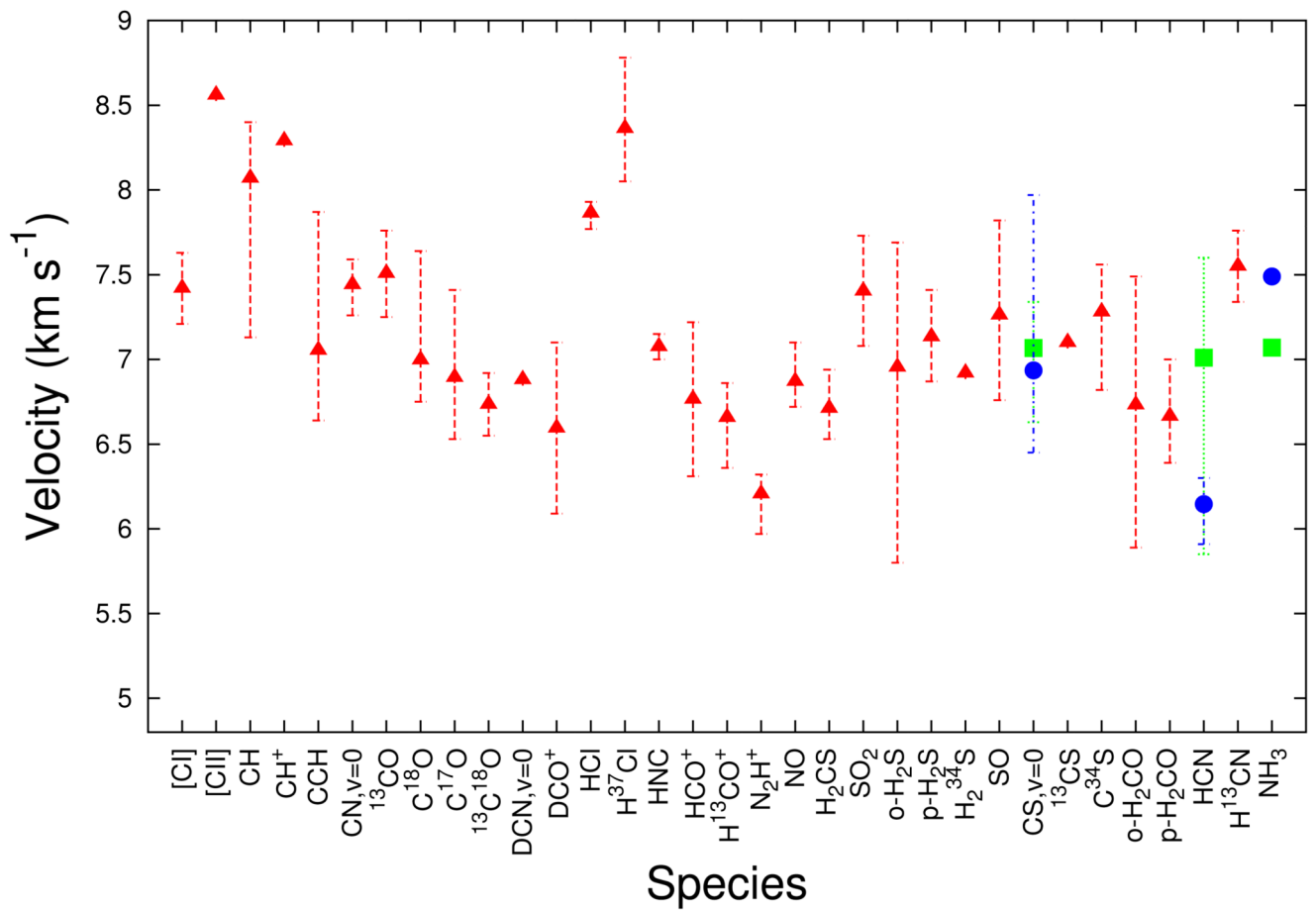


Fig. 12.

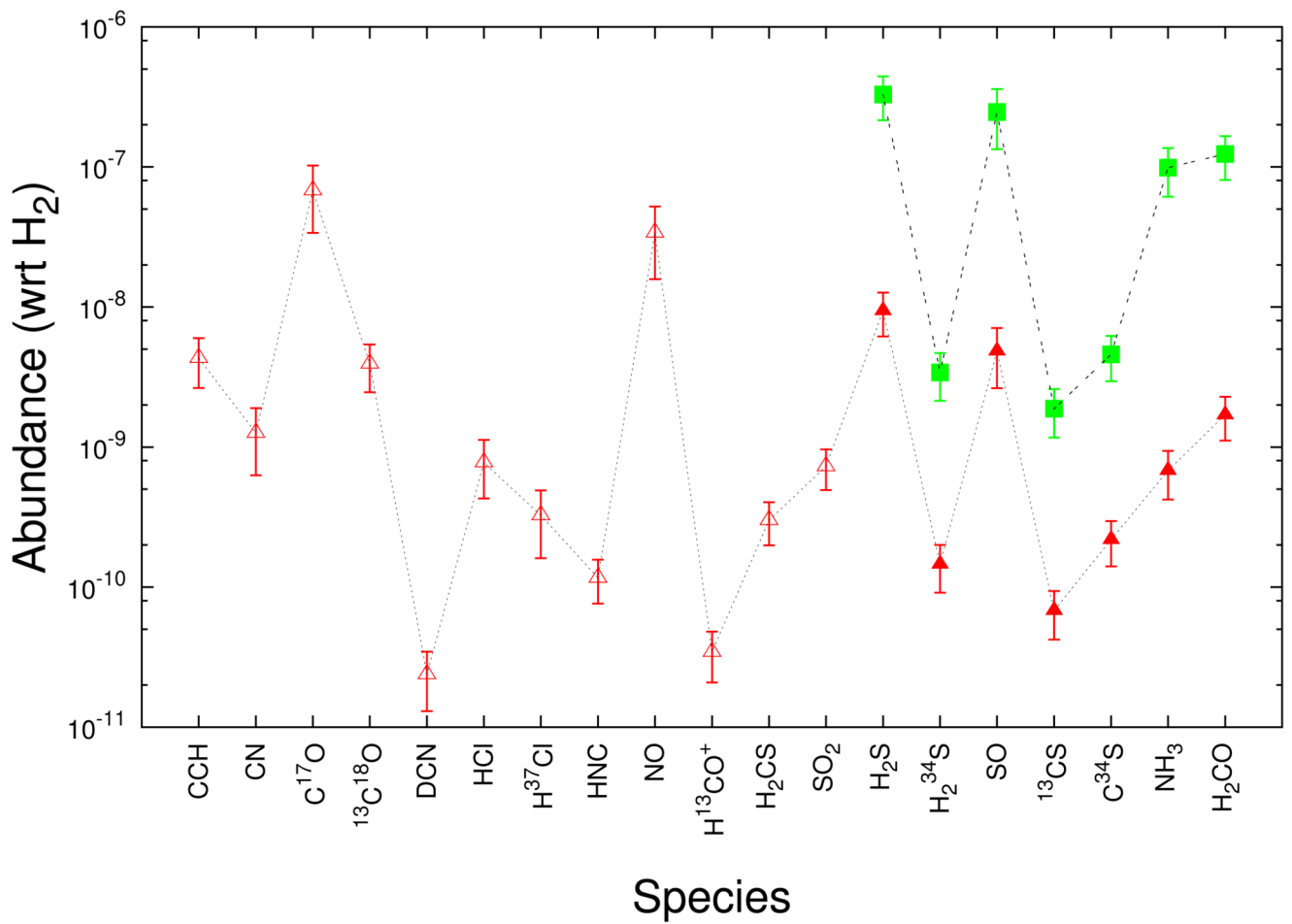
Plot of the measured $\Delta FWHM$ vs T_A derived from independent Gaussian fits to each of the A-CH₃OH and E-CH₃OH transitions listed in Table 4. The green and blue lines are the 1σ and 3σ (respectively) theoretical error envelope for the $\Delta FWHM$ determined from Gaussian fitting of noisy lines predicted by Porter et al. (2004). Curves are calculated assuming $\langle FWHM \rangle \sim 5 \text{ km s}^{-1}$ and $T_{rms} \sim 0.1 \text{ K}$ (typical values for methanol)

**Fig. 13.**

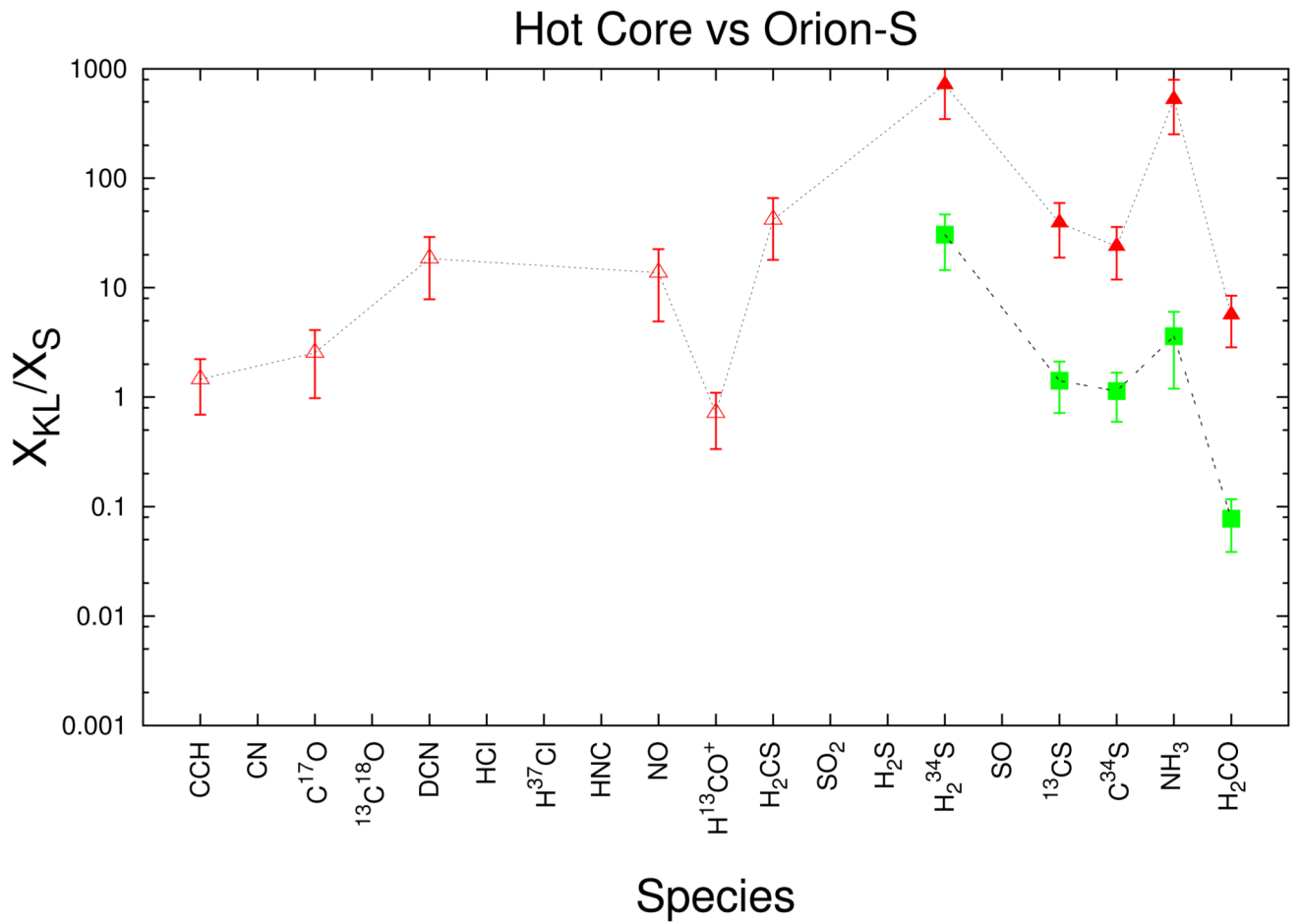
Plot of the continuum emission integrated over each band (red triangles), integrated line emission in each band (blue triangles), and the line to continuum ratio percentage (green circles). The red line is a power law fit to the continuum emission using a modified black body function (see text for details).

**Fig. 14.**

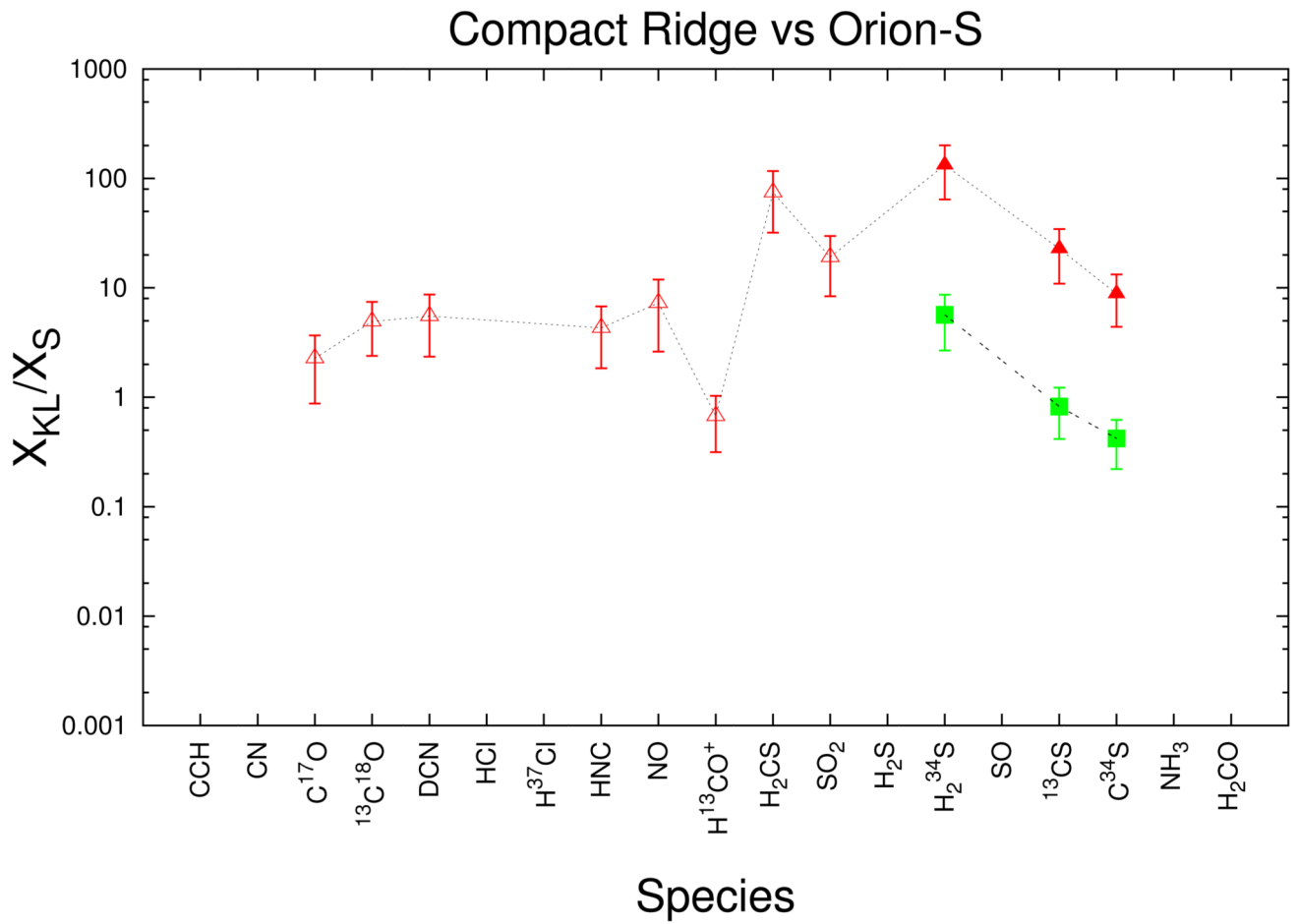
Mean V_{LSR} for each species derived from the Gaussian fits (Table 4). Red triangles indicate the mean V_{LSR} for species fit by a single Gaussian component. In cases requiring two component Gaussian fits, the narrow component is indicated by blue circle and the broad component is indicated by a green square. Error bars reflect the range in fitted V_{LSR} values provided in Table 4.

**Fig. 15.**

The abundance (with respect to H₂) of species listed in Tables 5 & 6. Open red triangles indicate the abundance ratio for species fitted by a single component LTE model in Orion-S. In cases requiring two component LTE models for the Orion-S data, the abundance ratio for the narrow component is indicated by solid red triangles and that for the broad component is indicated by solid green squares. Therefore, the dotted line connects species/components that likely trace quiescent gas, whereas the dashed line connects species/components that may trace shocked gas.

**Fig. 16.**

Comparison of the abundances of species detected in the Orion-KL Hot Core to those in Orion-S as given by equation 1 in Section 3.3.2. Symbols are the same as described in Figure 15.

**Fig. 17.**

Same as for Figure 16 except for the Orion-KL Compact Ridge

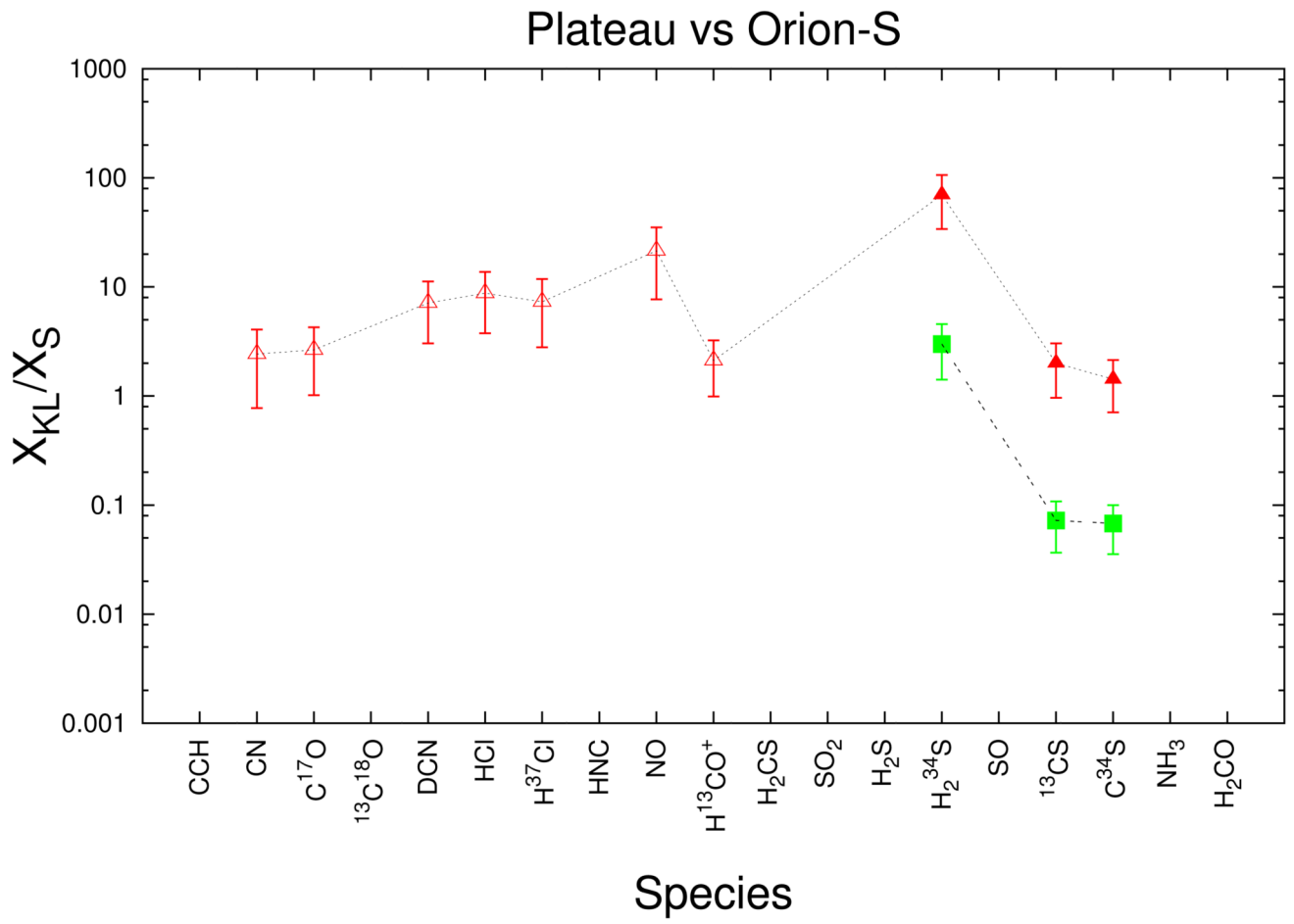


Fig. 18.
Same as for Figure 16 except for the Orion-KL Plateau.

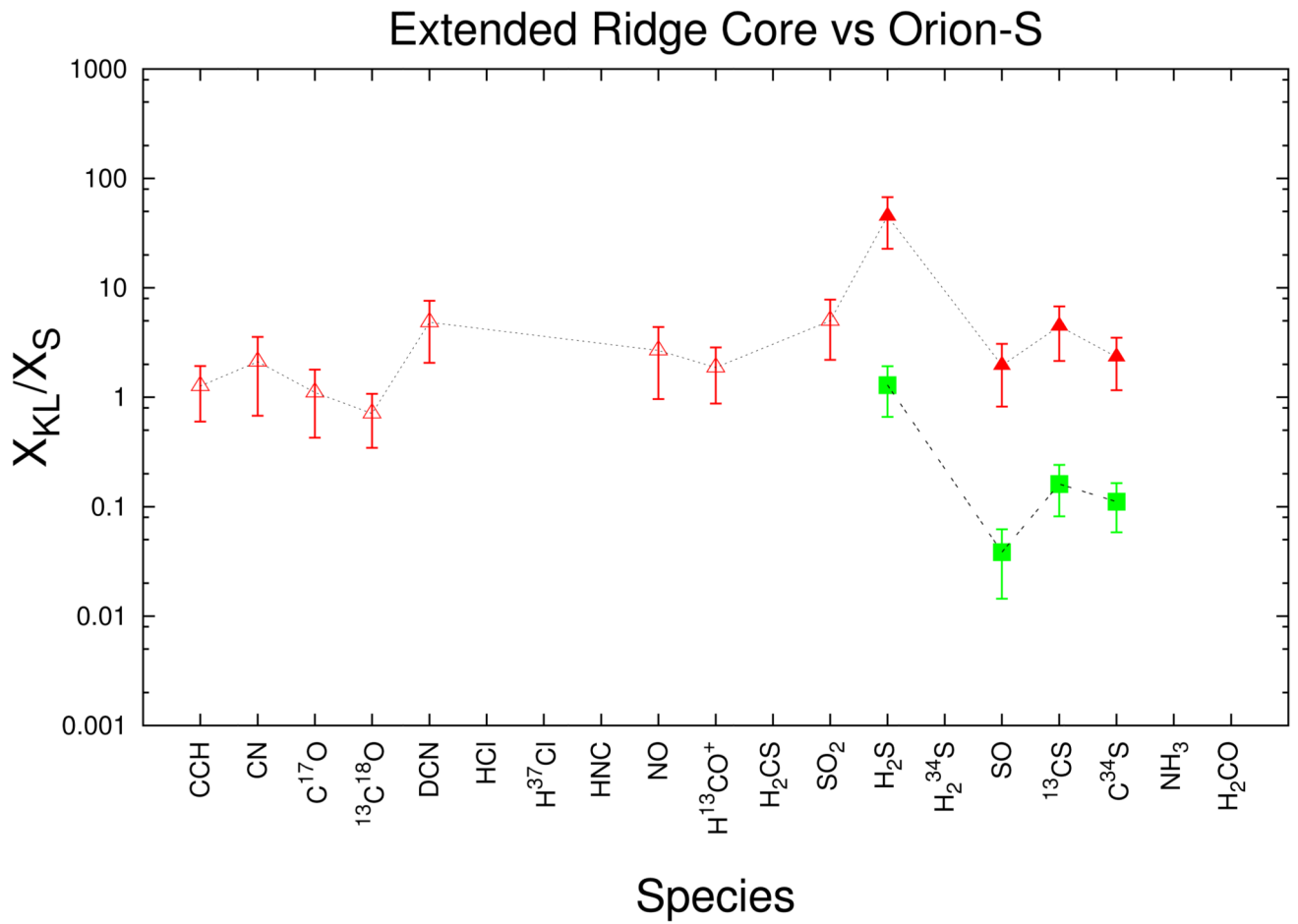


Fig. 19.
Same as for Figure 16 except for the Orion-KL Extended Ridge.

Table 1
Data Smoothing and Noise Characteristics

	Smoothing Channels	Freq. Res. (MHz)	Vel. Res. (km s ⁻¹)	T _{sys} (K)	1 σ rms (K)
band 1	2	2.2	1.0–1.4	~ 100	~ 0.02 – 0.05
band 2	4	4.4	1.6–2.1	~ 150	~ 0.03 – 0.07
band 3	4	4.4	1.4–1.7	~ 200	~ 0.04 – 0.09
band 4	8	8.8	2.4–2.8	~ 400	~ 0.1 – 0.2
band 5	8	8.8	2.1–2.4	~ 1000	~ 0.1 – 0.3
band 6	16	17.6	3.1–3.7	~ 1300	~ 0.3 – 2.0
band 7	16	17.6	2.8–3.1	~ 1300	~ 0.4 – 4.0

Table 2
Identified species in Orion-S

atoms	di-atomic molecules	multi-atomic molecules	Ionized species
C-atom	CO	CCH	C ⁺
	¹³ CO	DCN	CH ⁺
	¹³ C ¹⁸ O	HNC	CO ⁺
	C ¹⁸ O	HCN	DCO ⁺
	C ¹⁷ O	H ¹³ CN	H ¹³ CO ⁺
	CS	HC ¹⁵ N	HC ¹⁸ O ⁺
	¹³ CS	HDO ^a	HCO ⁺
	C ³⁴ S	o-H ₂ O	HCS ⁺
	CH	p-H ₂ O	N ₂ H ⁺
	CN	o-H ₂ ¹⁸ O ^a	SH ⁺
	HCl ^a	p-H ₂ ¹⁸ O ^a	
	H ³⁷ Cl ^a	o-H ₂ S	
	HF ^a	p-H ₂ S	
	NO ^a	H ₂ ³³ S	
	SiO	H ₂ ³⁴ S	
	SO	H ₂ CS	
		o-H ₂ CO	
		p-H ₂ CO	
		o-NH ₃	
		p-NH ₃	
		A-CH ₃ OH	
		E-CH ₃ OH	
		CH ₃ OCH ₃	
		NH ₂	
		SO ₂	

^aJPL database used for these species. For all other species CDMS database is used.

Table 3
All observed lines above the 3σ noise level in order of increasing frequency.

Band 1a		
Frequency (GHz)	T_A (K)	Species
480.2699	0.7	A-CH ₃ OH
481.5056	0.7	A-CH ₃ OH
481.9167	0.3	C ³⁴ S
482.2179	0.1	A-CH ₃ OH
482.2833	0.8	E-CH ₃ OH
482.9598	1.4	E-CH ₃ OH
483.0808	0.2	A-CH ₃ OH
483.1418	1.7	E-CH ₃ OH
483.3898	0.3	E-CH ₃ OH
483.3983	0.1	A-CH ₃ OH
483.4623	0.2	A-CH ₃ OH
483.4728	0.2	E-CH ₃ OH
483.5393	0.2	A-CH ₃ OH
483.5533	0.3	A-CH ₃ OH
483.5668	0.3	E-CH ₃ OH
483.5818	0.1	A-CH ₃ OH
483.6868	0.6	E-CH ₃ OH
483.7633	0.3	A-CH ₃ OH
484.0058	0.8	A-CH ₃ OH
484.0238	0.7	E-CH ₃ OH
484.0718	0.4	E-CH ₃ OH
484.2703	0.2	SO ₂
485.2638	0.9	A-CH ₃ OH
486.9419	0.9	A-CH ₃ OH
487.5319	0.6	A-CH ₃ OH
487.6639	0.2	H ₂ CS
489.0379	0.9	A-CH ₃ OH
489.7509	4.5	CS
490.5970	0.2	HDO
491.5520	0.7	A-CH ₃ OH
491.9335	0.2	SO ₂
491.9690	3.1	o-H ₂ CO
492.1615	4.7	[CI]
492.2795	2.0	A-CH ₃ OH

492.7841	0.1	CH ₃ OCH ₃
493.7000	1.4	A-CH ₃ OH
493.7350	1.4	A-CH ₃ OH
494.4820	0.6	A-CH ₃ OH
494.7781	0.2	SO ₂
495.1741	1.2	E-CH ₃ OH
496.9226	0.1	E-CH ₃ OH
497.8296	0.4	A-CH ₃ OH
501.5897	0.4	A-CH ₃ OH
503.0142	0.1	H ₂ ³⁴ S
504.2008	0.2	DCO ⁺
504.2948	1.3	E-CH ₃ OH
504.6783	0.1	SO
505.5658	1.5	o-H ₂ S
505.7633	0.3	A-CH ₃ OH
505.8343	1.7	p-H ₂ CO
506.1548	0.2	E-CH ₃ OH
506.7728	0.2	H ₂ CS
506.8273	0.2	DCN
508.5369	0.1	¹³ CS
508.7069	0.1	SO ₂
509.0924	0.1	A-CH ₃ OH
509.1469	0.8	p-H ₂ CO
509.2939	0.3	HDO
509.5654 ^b	0.8	E-CH ₃ OH + o-H ₂ CO
509.8314	0.3	p-H ₂ CO
510.1559	0.9	o-H ₂ CO
510.2389	0.9	o-H ₂ CO
510.3459	0.3	A-CH ₃ OH
510.9114	0.1	HC ¹⁸ O ⁺
511.0904	0.2	SO ₂
511.5024	0.1	SO ₂
511.7166	0.1	CH ₃ OCH ₃
511.9455	0.2	HCS ⁺
513.0775	0.7	p-H ₂ CO
513.3610	0.1	H ₂ CS
513.3698	0.1	CH ₃ OCH ₃
514.8535	0.7	SO
515.1700	0.2	A-CH ₃ OH

515.3335	0.2	A-CH ₃ OH
515.8230	0.1	Ghost
516.2616	0.2	HC ¹⁵ N
516.3361 ^b	0.7	SO
		+ H ₂ CS
517.3551	0.9	SO
517.9706	0.4	H ¹³ CN
520.1801	1.2	E-CH ₃ OH
520.4612	1.1	H ¹³ CO ⁺
520.7297	0.1	A-CH ₃ OH
520.8817	0.1	SiO
522.4057	0.1	H ₂ CS
523.1002	0.0	E-CH ₃ OH
523.2752	0.3	E-CH ₃ OH
523.4827	0.1	¹³ C ¹⁸ O
523.9727	2.2	CCH
524.0352	1.8	CCH
524.2682	0.1	E-CH ₃ OH
524.5847	0.1	E-CH ₃ OH
524.6673	0.1	E-CH ₃ OH
524.7418	0.2	E-CH ₃ OH
524.8053	0.2	E-CH ₃ OH
524.8628	0.2	E-CH ₃ OH
524.9098	0.2	E-CH ₃ OH
524.9483	0.1	E-CH ₃ OH
525.0548	0.1	E-CH ₃ OH
525.6663	2.5	o-H ₂ CO
526.0363	0.1	SH ⁺
526.0453	0.1	SH ⁺
526.5233	0.1	A-CH ₃ OH
526.5483	0.1	E-CH ₃ OH
526.7878	0.1	E-CH ₃ OH
527.0548	0.4	A-CH ₃ OH
527.1738	0.1	E-CH ₃ OH
527.6608	0.1	E-CH ₃ OH
528.1813	0.1	E-CH ₃ OH
528.6833	0.1	E-CH ₃ OH
529.1419	0.2	E-CH ₃ OH
529.2904	0.1	SO ₂
529.5409	0.2	E-CH ₃ OH



529.8679	0.2	E-CH ₃ OH
529.9739	0.2	SO ₂
530.0699	0.2	A-CH ₃ OH
530.1234	0.3	C ³⁴ S
530.1849	0.6	E-CH ₃ OH
530.0244	0.1	E-CH ₃ OH
530.3174	0.4	E-CH ₃ OH
530.4559	0.5	E-CH ₃ OH
530.5499	0.5	E-CH ₃ OH
530.6124	0.5	E-CH ₃ OH
530.6484	0.5	E-CH ₃ OH
530.8244	0.2	E-CH ₃ OH
531.0804	1.2	E-CH ₃ OH
531.3199	1.3	A-CH ₃ OH
531.6384	0.2	A-CH ₃ OH
531.7159	7.5	HCN
531.8709	0.4	A-CH ₃ OH
531.8924	0.3	A-CH ₃ OH
532.0334	0.4	E-CH ₃ OH
532.0709	0.2	E-CH ₃ OH
532.1349	0.3	A-CH ₃ OH
532.3239	0.1	CH ₃ OCH ₃
532.4669	0.6	E-CH ₃ OH
532.5684	0.4	E-CH ₃ OH
532.7214	2.4	CH
532.7909	1.0	CH
533.3810	0.1	Ghost
535.0610	14. 6	HCO ⁺
536.1925	0.6	A-CH ₃ OH
536.7585	2.1	CH
536.7805	0.5	CH
536.7925	0.9	CH
538.5716	2.2	A-CH ₃ OH
538.6891	3.4	CS
539.2806	0.1	E-CH ₃ OH
540.4656	0.2	H ₂ CS
540.9236	0.1	E-CH ₃ OH
541.7536	0.2	SO ₂
541.8162	0.1	SO ₂
542.0022	1.3	A-CH ₃ OH

542.0832	1.4	A-CH ₃ OH
543.0777	1.2	E-CH ₃ OH
543.8987	0.1	HNC
545.0437 ^b	0.2	E-CH ₃ OH + A -CH ₃ OH
545.1032	0.2	Ghost
545.8872	0.2	Ghost
546.2488	0.2	A-CH ₃ OH
547.3003	0.2	Ghost
547.6768	0.3	H ₂ ¹⁸ O
548.8313	8.1	C ¹⁸ O
549.2998	0.1	SO ₂
549.5506	0.1	CH ₃ OCH ₃
549.5533	0.1	NO
550.6564	0.0	A-CH ₃ OH
550.9254	29. 4	¹³ CO
551.1874	0.3	NO
551.5159	0.1	Ghost
551.5344	0.3	NO
553.1474	1.0	E-CH ₃ OH
554.0569	0.2	E-CH ₃ OH
554.5784	0.1	HCS ⁺
555.6670	0.1	SO ₂
556.9370	7.2	o-H ₂ O
557.1260	0.1	H ₂ CS
558.0870	0.3	SO
558.3465	0.4	E-CH ₃ OH
558.9681	2.5	N ₂ H ⁺
559.3216	0.4	SO
560.1781	0.5	SO
560.2496	0.2	E-CH ₃ OH
560.2716	0.2	E-CH ₃ OH
560.3001	0.2	Ghost

Band 1b

Frequency (GHz)	T _A (K)	Species
556.9370	8.4	o-H ₂ O
558.0875	0.5	SO

558.3460	0.5	E-CH ₃ OH
558.9681	3.4	N ₂ H ⁺
559.3206	0.5	SO
560.1781	0.6	SO
561.7136	3.0	C ¹⁷ O
561.9001	2.7	o-H ₂ CO
564.2522	0.1	SiO
566.7312	1.3	CN
566.9477	1.6	CN
567.2612	0.2	Ghost
567.5953	0.1	SO ₂
568.2358	0.2	E-CH ₃ OH
568.4353	0.2	CH ₃ OCH ₃
568.5673	1.3	E-CH ₃ OH
568.7853	0.2	A-CH ₃ OH
570.2434	0.1	CH ₃ OCH ₃
572.4974	3.3	o-NH ₃
572.8984	0.2	E-CH ₃ OH
574.1399	0.1	H ₂ CS
574.8084	0.1	SO ₂
574.8694	0.3	A-CH ₃ OH
576.2050 ^b	0.4	DCO ⁺
576.2660	62.0	CO
576.3835	0.2	Ghost
576.7095	1.1	p-H ₂ CO
578.0080	0.4	E-CH ₃ OH
578.2165	0.2	C ³⁴ S
579.0860	1.4	A-CH ₃ OH
579.1520	0.8	E-CH ₃ OH
579.1995	0.1	DCN
579.4605	0.9	A-CH ₃ OH
579.8590	0.2	A-CH ₃ OH
579.9225	1.4	A-CH ₃ OH
580.0600	0.1	A-CH ₃ OH
580.1760	0.2	A-CH ₃ OH
580.2135	0.2	A-CH ₃ OH
580.3696	0.3	E-CH ₃ OH
580.4446	0.2	E-CH ₃ OH
580.5026	0.2	A-CH ₃ OH
580.9036	0.4	E-CH ₃ OH
581.0916	0.3	E-CH ₃ OH

581.6131	0.5	p-H ₂ CO
582.3841	0.2	o-H ₂ CO
582.7246	0.2	p-H ₂ CO
583.1456	0.6	o-H ₂ CO
583.3096	0.5	o-H ₂ CO
584.4511	1.9	A-CH ₃ OH
584.8227	0.5	A-CH ₃ OH
587.4537	0.4	p-H ₂ CO
587.5702	0.2	SO ₂
587.6167	2.3	CS
589.1653	0.1	CH ₃ OCH ₃
589.8703	0.1	CO ⁺
590.2793	1.2	A-CH ₃ OH
590.4418	1.1	A-CH ₃ OH
590.7522	0.1	CH ₃ OCH ₃
590.7923	0.9	E-CH ₃ OH
591.8218	0.1	H ₂ CS
593.9424	0.1	SO ₂
593.9624	0.1	SO ₂
597.2084	0.1	HCS ⁺
598.5485	-0.1	Ghost
599.9280	0.3	HDO
600.3320	1.7	o-H ₂ CO
600.9065	0.1	¹³ CS
601.2570	0.4	SO
601.8521	0.1	E-CH ₃ OH
602.2346	0.8	E-CH ₃ OH
602.2750		HC ¹⁵ N
602.2916	0.4	SO
603.0236	0.5	SO
604.2641	0.2	H ¹³ CN
604.3696	0.2	SO ₂
605.8801	0.1	E-CH ₃ OH
607.1762	0.8	H ¹³ CO ⁺
607.2167	0.3	E-CH ₃ OH
607.6112	0.1	SiO
607.7982	0.2	H ₂ CS
608.0984	0.1	CH ₃ OCH ₃
609.7087	0.1	CH ₃ OCH ₃
611.2688	1.2	CCH
611.3308	1.0	CCH
611.5518	0.1	SO

613.0798	0.1	SO ₂
616.9814	1.2	E-CH ₃ OH
620.3035	5.6	HCN
620.7045	0.6	o-H ₂ O
622.5705	0.1	A-CH ₃ OH
622.6605	0.3	A-CH ₃ OH
622.7755	0.2	E-CH ₃ OH
624.1801	0.2	E-CH ₃ OH
624.2081	13.3	HCO ⁺
624.9616	1.0	H ³⁷ Cl
624.9751	1.4	H ³⁷ Cl
624.9856	0.6	H ³⁷ Cl
625.7521	0.4	E-CH ₃ OH
625.7601	0.1	A-CH ₃ OH
625.8996	2.1	HCl
625.9166	2.8	HCl
625.9296	1.5	HCl
626.0896	0.2	SO ₂
626.3521	0.1	C ³⁴ S
626.4996	0.2	H ₂ CS
626.5141	0.1	A-CH ₃ OH
626.5566	0.2	E-CH ₃ OH
626.6271	1.5	A-CH ₃ OH
627.0203	0.1	CH ₃ OCH ₃
627.1036	0.1	Ghost
627.1721	0.6	E-CH ₃ OH
627.5602	0.7	A-CH ₃ OH
628.0522	0.2	A-CH ₃ OH
628.1422	0.2	¹³ C ¹⁸ O
628.3302	0.2	E-CH ₃ OH
628.4482	0.2	E-CH ₃ OH
628.4717	0.3	A-CH ₃ OH
628.5142	0.2	A-CH ₃ OH
628.5272	0.2	A-CH ₃ OH
628.6627	0.1	CH ₃ OCH ₃
628.6982	0.3	E-CH ₃ OH
628.8182	0.2	E-CH ₃ OH
628.8682	0.2	A-CH ₃ OH
629.1417	1.6	A-CH ₃ OH
629.3232	0.4	E-CH ₃ OH
629.6517	0.3	E-CH ₃ OH

629.9222	1.7	A-CH ₃ OH
631.2847	0.2	Ghost
631.7038	1.7	o-H ₂ CO
632.1918	0.2	SO ₂
633.4248	0.4	A-CH ₃ OH
634.5118	0.6	HNC
635.8673	0.3	A-CH ₃ OH
636.3394	0.5	A-CH ₃ OH
636.3979	0.4	A-CH ₃ OH
636.4209	0.6	A-CH ₃ OH

Band 2a

Frequency (GHz)	T _A (K)	Species
626.5191	0.7	A-CH ₃ OH
626.6271	1.3	A-CH ₃ OH
627.1711	0.6	E-CH ₃ OH
627.5607	0.5	A-CH ₃ OH
629.1417	1.0	A-CH ₃ OH
629.3242	0.3	E-CH ₃ OH
629.6482	0.3	E-CH ₃ OH
629.9232	1.2	A-CH ₃ OH
631.7038	1.3	o-H ₂ CO
633.4233	0.3	A-CH ₃ OH
634.5113	0.5	HNC
636.2514	0.2	A-CH ₃ OH
636.2749	0.3	A-CH ₃ OH
636.3059	0.3	A-CH ₃ OH
636.3349	0.3	A-CH ₃ OH
636.3669	0.4	A-CH ₃ OH
636.3949	0.4	A-CH ₃ OH
636.4209	0.3	A-CH ₃ OH
636.5199	0.3	A-CH ₃ OH
636.5339	1.3	CS
638.2804	0.7	E-CH ₃ OH
638.5259	1.0	A-CH ₃ OH
638.8194	0.9	A-CH ₃ OH
644.3252	0.2	NH ₂
644.3790	0.4	SO
645.2576	0.4	SO

645.8756	0.4	SO
645.9282	0.1	CH ₃ OCH ₃
647.0831	0.2	p-H ₂ CO
647.6130	0.2	CH ₃ OCH ₃
648.1956	0.2	DCO ⁺
649.5402	0.2	E-CH ₃ OH
651.2997	0.1	SO ₂
651.4352	0.3	NO
651.6177	0.6	E-CH ₃ OH
651.7742	0.4	NO
652.0972	2.8	N ₂ H ⁺
653.9703	0.4	p-H ₂ CO
655.2128	0.2	o-H ₂ CO
655.6353	0.2	p-H ₂ CO
656.1653	0.6	o-H ₂ CO
656.1723	0.4	E-CH ₃ OH
656.4663	0.5	o-H ₂ CO
658.5544	7.7	C ¹⁸ O
661.0659	30.3	¹³ CO
662.2105	0.4	p-H ₂ CO
664.8193	0.1	CH ₃ OCH ₃
665.2485	0.2	SO ₂
665.4440	1.3	E-CH ₃ OH
670.3602	0.2	SO ₂
670.4242	0.3	A-CH ₃ OH
672.5657	0.2	SO ₂
672.8362	0.1	A-CH ₃ OH
672.9037	0.3	E-CH ₃ OH
673.4172	0.3	E-CH ₃ OH
673.7472	1.4	A-CH ₃ OH
674.0107	2.4	C ¹⁷ O
674.8113	1.1	o-H ₂ CO
674.9913 ^b	1.4	A-CH ₃ OH + E-CH ₃ OH
675.0558	0.2	H ₂ CS
675.1353	0.5	E-CH ₃ OH
675.6138	0.5	A-CH ₃ OH
675.7748	0.8	E-CH ₃ OH
676.2143	0.3	A-CH ₃ OH
676.4618	0.1	SO ₂
676.7523	0.3	A-CH ₃ OH

676.8298	0.3	A-CH ₃ OH
677.0138	0.3	E-CH ₃ OH
677.7113	0.4	E-CH ₃ OH
678.2528	0.2	E-CH ₃ OH
678.7688	0.2	Ghost
678.7864	1.6	A-CH ₃ OH
680.0429	0.6	CN
680.2599	0.8	CN
681.5310	-0.1	Ghost
681.9919	0.4	A-CH ₃ OH
685.4375	1.0	CS
685.5050	0.6	E-CH ₃ OH
686.7325	0.7	A-CH ₃ OH
687.0220	0.1	H ₂ ³⁴ S
687.1515	0.2	H ₂ ³³ S
687.2270	0.8	A-CH ₃ OH
687.3040	2.3	p-H ₂ S
687.4571	0.4	SO
688.2021	0.3	SO
688.7286	0.3	SO
690.5551	0.2	H ¹³ CN
691.4706	64.4	CO
693.8787	0.4	H ¹³ CO ⁺
697.1083	0.1	Ghost
697.1448	0.2	E-CH ₃ OH
698.5458	0.6	CCH
698.6083	0.6	CCH
701.3709 ^b	1.3	o-H ₂ CO + E-CH ₃ OH
704.2609	0.2	Ghost
704.4134	0.2	CH ₃ OCH ₃
704.9400	0.5	Ghost
705.1840	0.3	E-CH ₃ OH
705.4000	0.2	Ghost
705.9605	0.4	Ghost
706.6255	0.3	Ghost
707.3180	0.4	Ghost
707.7905	0.4	E-CH ₃ OH
708.4735 ^b	0.5	o-H ₂ S
	0.0	+ H ₂ ³³ S
708.7085	0.4	Ghost

708.8741	3.2	HCN
709.2771	0.3	Ghost
713.3422	10.0	HCO ⁺
713.9837	0.9	E-CH ₃ OH
716.9402	0.5	p-H ₂ CO
718.1618	0.3	A-CH ₃ OH
718.4378	0.9	E-CH ₃ OH
719.6653	1.1	A-CH ₃ OH
719.7293	1.0	Ghost
719.9548	1.5	Ghost
720.0118	0.9	E-CH ₃ OH
720.4418	1.2	A-CH ₃ OH
721.0118	0.2	E-CH ₃ OH
723.0404	0.4	E-CH ₃ OH
723.6219	0.4	A-CH ₃ OH
724.1224	0.7	E-CH ₃ OH
724.3489	0.4	A-CH ₃ OH
725.0954	0.9	Ghost
716.9412	0.6	p-H ₂ CO

Band 2b

Frequency (GHz)	T _A (K)	Species
718.1623	0.3	A-CH ₃ OH
718.4378	1.0	E-CH ₃ OH
719.6668	1.2	A-CH ₃ OH
720.4433	1.4	A-CH ₃ OH
721.0093	0.3	E-CH ₃ OH
723.0429	0.5	E-CH ₃ OH
723.2824	0.3	E-CH ₃ OH
723.6199	0.5	A-CH ₃ OH
724.1219	0.9	E-CH ₃ OH
724.3409	0.2	A-CH ₃ OH
725.1089	0.3	HNC
725.1279	0.3	A-CH ₃ OH
725.3169	0.2	E-CH ₃ OH
726.0540	0.2	E-CH ₃ OH
726.2100	0.4	p-H ₂ CO
726.9025	0.3	E-CH ₃ OH
728.0535	0.3	o-H ₂ CO

728.5860	0.3	p-H ₂ CO
728.5960	0.2	p-H ₂ CO
728.8650	1.5	A-CH ₃ OH
729.2120	0.5	o-H ₂ CO
729.7260	0.4	o-H ₂ CO
730.5006	0.4	SO
730.5206	0.4	A-CH ₃ OH
731.1416	0.3	SO
731.5981	0.3	SO
732.4336	0.6	A-CH ₃ OH
732.7761	0.2	¹³ C ¹⁸ O
734.2706	0.4	H ₂ ³⁴ S
734.3286	0.8	CS
734.8952	0.6	A-CH ₃ OH
735.6762	0.6	A-CH ₃ OH
736.0317	4.3	o-H ₂ S
737.3407	0.4	p-H ₂ CO
737.6272	0.2	Ghost
741.2263	0.2	E-CH ₃ OH
742.2408	0.2	H ₂ CS
745.2119	1.8	N ₂ H ⁺
747.3035	0.3	p-H ₂ S
749.0735	0.8	o-H ₂ CO
751.5560	0.4	E-CH ₃ OH
751.6766	0.3	NO
752.0321	7.9	p-H ₂ O
752.1076	0.6	E-CH ₃ OH
752.1366	0.4	E-CH ₃ OH
752.1716	0.3	E-CH ₃ OH
752.3111	0.3	E-CH ₃ OH
753.4161	0.2	HDO
753.8671	0.1	E-CH ₃ OH
754.2226	0.2	E-CH ₃ OH
762.6378	0.9	E-CH ₃ OH
763.8823	0.3	E-CH ₃ OH
763.9533	0.9	A-CH ₃ OH
764.5828	-0.5	Ghost
764.8119	0.2	E-CH ₃ OH
765.5134	0.2	E-CH ₃ OH
765.9404	0.2	o-H ₂ S
766.0309	0.3	E-CH ₃ OH

766.3974	0.4	E-CH ₃ OH
766.6489	0.5	E-CH ₃ OH
766.7124	1.2	A-CH ₃ OH
766.7624	0.8	E-CH ₃ OH
766.8114	0.4	E-CH ₃ OH
766.9094	0.5	E-CH ₃ OH
766.9614	0.5	E-CH ₃ OH
766.9844	0.5	E-CH ₃ OH
768.2529	5.6	C ¹⁸ O
768.5404	0.2	E-CH ₃ OH
770.8855	0.4	E-CH ₃ OH
770.8980	0.9	o-H ₂ CO
771.1825	27.1	¹³ CO
771.5770	0.4	A-CH ₃ OH
772.4425	0.2	A-CH ₃ OH
772.4545	0.6	E-CH ₃ OH
773.2611	0.2	A-CH ₃ OH
773.4226	0.3	A-CH ₃ OH
773.5136	0.3	SO
773.8896	0.2	E-CH ₃ OH
773.9481	0.2	A-CH ₃ OH
774.0666	0.2	SO
774.3331	0.3	E-CH ₃ OH
774.4541	0.3	SO
775.5996	0.4	E-CH ₃ OH
779.0072	0.5	A-CH ₃ OH
779.0322	0.4	E-CH ₃ OH
779.3822	1.3	A-CH ₃ OH
780.5672	0.3	H ¹³ CO ⁺
783.0028	0.5	A-CH ₃ OH
783.1993	0.6	CS
784.1793	0.3	A-CH ₃ OH
785.8058	0.3	CCH
785.8679	0.2	CCH
786.2829 ^b	1.5	C ¹⁷ O + p-H ₂ CO
790.9360	0.7	Ghost
793.3410	0.4	CN
793.5480	0.3	CN
794.5211	0.2	Ghost
794.8206	0.2	Ghost
797.4306	1.7	HCN

798.3106	0.2	p-H ₂ CO
----------	-----	---------------------

Band 3a

Frequency (GHz)	T _A (K)	Species
802.2430	0.3	E-CH ₃ OH
802.2810	0.3	o-H ₂ CO
802.4590	7.1	HCO ⁺
803.1130	0.3	o-H ₂ CO
806.6501	59.4	CO
807.8661	0.6	A-CH ₃ OH
809.3431	6.8	[Cl]
811.4452	0.6	E-CH ₃ OH
812.5522	0.9	A-CH ₃ OH
813.5442	0.2	A-CH ₃ OH
815.0723	0.8	E-CH ₃ OH
815.6943	0.1	HNC
816.0153	0.2	E-CH ₃ OH
816.4953	0.2	SO
816.9743	0.2	SO
817.3143	0.2	SO
818.6674	0.2	E-CH ₃ OH
819.4844	0.3	A-CH ₃ OH
820.5024	0.2	A-CH ₃ OH
820.7644	0.4	E-CH ₃ OH
821.4774	0.2	A-CH ₃ OH
821.7014	0.2	A-CH ₃ OH
821.8694	0.2	E-CH ₃ OH
822.5475	0.3	E-CH ₃ OH
823.0845	0.6	o-H ₂ CO
824.3525	0.2	E-CH ₃ OH
824.7255	0.2	E-CH ₃ OH
825.2795	0.3	E-CH ₃ OH
827.4516	0.2	A-CH ₃ OH
829.8906	0.7	A-CH ₃ OH
830.3506	1.0	A-CH ₃ OH
831.0487	0.3	A-CH ₃ OH
832.0627	0.5	CS
832.7567	0.4	A-CH ₃ OH
834.6517	0.2	E-CH ₃ OH

834.7517	0.1	E-CH ₃ OH
834.8397	0.2	E-CH ₃ OH
834.9017	0.1	E-CH ₃ OH
834.9577	0.2	E-CH ₃ OH
835.0037	0.1	E-CH ₃ OH
835.1358	3.0	CH ⁺
838.3088	0.8	N ₂ H ⁺
840.2779	0.6	o-H ₂ CO
851.4161	0.7	A-CH ₃ OH
851.9151	0.3	NO
853.5112	0.3	E-CH ₃ OH
855.1542	0.3	p-H ₂ CO
857.9613	0.7	A-CH ₃ OH

Band 3b

Frequency (GHz)	T _A (K)	Species
860.4618	0.5	E-CH ₃ OH
863.3639	0.6	E-CH ₃ OH
863.4269	0.2	E-CH ₃ OH
867.3250	0.3	A-CH ₃ OH
869.0370	0.5	E-CH ₃ OH
869.9821	0.3	A-CH ₃ OH
870.1091	0.2	E-CH ₃ OH
870.2811	0.2	p-H ₂ CO
873.0361	0.2	CCH
873.7811	0.1	o-H ₂ CO
875.3692	0.2	o-H ₂ CO
876.6462	0.1	o-H ₂ CO
877.9232	3.4	C ¹⁸ O
878.2273	0.7	A-CH ₃ OH
879.0153	0.2	A-CH ₃ OH
880.9043	0.3	CS
881.2703	21.6	¹³ CO
881.4223	0.3	A-CH ₃ OH
881.7833	0.8	A-CH ₃ OH
885.9664	1.2	HCN
890.1265	0.3	E-CH ₃ OH
891.5586	5.5	HCO ⁺
893.6387	-0.7	HDO

894.6146	0.5	A-CH ₃ OH
896.8077	0.3	o-H ₂ CO
898.5247	0.9	C ¹⁷ O
898.9777	0.2	Ghost
900.9658	0.1	E-CH ₃ OH
902.9388	0.5	A-CH ₃ OH
902.9838	0.2	SO
905.3959	0.2	E-CH ₃ OH
905.3959	0.2	E-CH ₃ OH
906.5939	0.2	CN
906.8029	0.2	CN
907.4303	0.2	NH ₂
909.5120	0.3	o-H ₂ CO
909.7400	0.4	E-CH ₃ OH
910.8110	0.2	E-CH ₃ OH
911.6440	0.5	E-CH ₃ OH
912.1100	0.8	E-CH ₃ OH
916.1771	0.5	p-H ₂ O
916.6502	0.3	E-CH ₃ OH
917.2702	0.4	E-CH ₃ OH
917.4082	0.2	E-CH ₃ OH
921.7973	59.5	CO
921.9873	0.5	E-CH ₃ OH
923.5853	0.3	p-H ₂ CO
926.5564	0.5	A-CH ₃ OH
926.8944	0.3	A-CH ₃ OH
929.7315	0.3	CS
930.2035	0.3	A-CH ₃ OH
931.3885	0.4	N ₂ H ⁺
933.6945	0.6	A-CH ₃ OH
937.4826	0.4	A-CH ₃ OH
947.4759	0.3	A-CH ₃ OH
952.5422	-0.3	NH ₂
952.5740	-0.8	NH ₂
952.6268	-0.3	NH ₂

Band 4a

Frequency (GHz)	T _A (K)	Species
960.4732	0.6	E-CH ₃ OH

965.4513	0.4	E-CH ₃ OH
974.4895	0.7	HCN
974.6895	0.3	A-CH ₃ OH
974.8795	0.5	A-CH ₃ OH
980.0316	0.4	A-CH ₃ OH
980.6376	4.3	HCO ⁺
986.1018	0.6	A-CH ₃ OH
987.5618	2.2	C ¹⁸ O
987.9298	8.5	p-H ₂ O
991.3259	17.6	¹³ CO
991.5839	0.5	A-CH ₃ OH
993.1019	1.7	o-H ₂ S
1002.7782	0.8	p-H ₂ S
1006.1242	0.4	E-CH ₃ OH
1008.8183	0.6	E-CH ₃ OH
1010.7323	0.6	C ¹⁷ O
1013.5664	0.4	E-CH ₃ OH
1023.1986	0.6	A-CH ₃ OH
1036.6990	1.1	SO ₂
1036.9070	66.9	CO
1039.0150	0.5	A-CH ₃ OH
1057.1194	0.5	E-CH ₃ OH

Band 4b

Frequency (GHz)	T _A (K)	Species
1057.1239	0.5	E-CH ₃ OH
1062.9821	1.0	HCN
1069.6982	2.8	HCO ⁺
1072.8303	1.0	o-H ₂ S
1092.4668	0.4	A-CH ₃ OH
1097.1589	1.4	C ¹⁸ O
1097.3689	3.4	o-H ₂ O
1101.3450	12.5	¹³ CO
1101.6990	-0.7	p-H ₂ ¹⁸ O
1105.3691	0.4	E-CH ₃ OH
1113.3472	4.0	p-H ₂ O

Band 5a

Frequency (GHz)	T_A (K)	Species
1113.3477	3.5	p-H ₂ O
1119.8339	0.4	A-CH ₃ OH
1122.9060	0.3	C ¹⁷ O
1151.4506	0.6	HCN
1151.7555	0.9	A-CH ₃ OH
1151.9826	51.0	CO
1152.9207	0.6	A-CH ₃ OH
1153.1267	4.4	o-H ₂ O
1153.5527	0.6	E-CH ₃ OH
1158.7328	1.7	HCO ⁺
1162.7149 ^b	0.6	A-CH ₃ OH + E-CH ₃ OH
1162.9129	4.4	o-H ₂ O
1168.1190	0.5	A-CH ₃ OH
1168.4524	-1.1	p-NH ₃
1196.0197	0.5	o-H ₂ S
1206.7279	0.7	C ¹⁸ O
1207.6540	0.5	p-H ₂ O
1211.3260	6.8	¹³ CO
1214.8529	-1.0	o-NH ₃
1215.2457	-1.3	p-NH ₃
1228.7924	1.3	p-H ₂ O
1232.4685	-1.2	HF

Band 5b

1228.7922	1.7	p-H ₂ O
1232.4692	-1.2	HF
1239.9125	0.4	HCN
1247.7406	0.8	HCO ⁺
1267.0091	44.6	CO

Band 6a

1496.9192	42.0	CO
-----------	------	----

Band 6b

1611.7859	37.3	CO
-----------	------	----

1669.9169	7.7	o-H ₂ O
-----------	-----	--------------------

Band 7a

1726.5976	26.9	CO
-----------	------	----

Band 7b

1841.3367	20.1	CO
-----------	------	----

1900.5261	69.5	[CII]
-----------	------	-------

Table 4
Gaussian fits to lines above 5σ

[CI]						
Transition $2s+1L_{J,L+S}$	Frequency MHz	T_A (K)	V_{lsr} (km s $^{-1}$)	V_{FWHM} (km s $^{-1}$)	$\int T_A dV$ (K km s $^{-1}$)	E_u (K)
$^3P_1 \rightarrow ^3P_0$	492161.28	5.2	7.6	4.7	26.1	23.62
$^3P_2 \rightarrow ^3P_1$	809342.91	6.9	7.2	4.2	30.8	62.46
[CII]						
Transition $2s+1L_{J,L+S}$	Frequency MHz	T_A (K)	V_{lsr} (km s $^{-1}$)	V_{FWHM} (km s $^{-1}$)	$\int T_A dV$ (K km s $^{-1}$)	E_u (K)
$^2P_{3/2} \rightarrow ^2P_{1/2}$	1900527.55	69.1	8.6	3.8	279.8	91.21
CCH						
Transition N_{J,F_1}	Frequency MHz	T_A (K)	V_{lsr} (km s $^{-1}$)	V_{FWHM} (km s $^{-1}$)	$\int T_A dV$ (K km s $^{-1}$)	E_u (K)
$6_{6,5,7} \rightarrow 5_{5,5,6}$	523972.07	2.2	6.6	4.5	10.7	88.02
$6_{5,5,6} \rightarrow 5_{4,5,5}$	524034.40	1.9	6.7	4.0	8.1	88.04
$7_{7,5,8} \rightarrow 6_{6,5,7}$	611267.06	1.2	6.8	5.2	6.4	117.36
$7_{6,5,6} \rightarrow 6_{5,5,5}$	611329.64	1.0	7.0	4.9	5.0	117.38
$8_{8,5,9} \rightarrow 7_{7,5,8}$	698544.47	0.6	7.4	5.9	3.7	150.88
$8_{7,5,7} \rightarrow 7_{6,5,6}$	698607.43	0.5	7.0	5.2	2.8	150.91
$9_{9,5,10} \rightarrow 8_{8,5,9}$	785801.64	0.3	7.9	8.2	2.3	188.59
$9_{8,5,8} \rightarrow 8_{7,5,7}$	785864.19	0.2	7.0	5.8	1.3	188.62
CH						
Transition N_{K,J,F_1}	Frequency MHz	T_A (K)	V_{lsr} (km s $^{-1}$)	V_{FWHM} (km s $^{-1}$)	$\int T_A dV$ (K km s $^{-1}$)	E_u (K)
$1_{1,1,5,1} \rightarrow 1_{-1,0,5,1}$	532721.73	2.4	7.1	4.2	10.8	25.73
$1_{1,1,5,1} \rightarrow 1_{-1,0,5,0}$	532791.46	1.0	8.4	4.8	4.9	25.73
$1_{-1,1,5,2} \rightarrow 1_{1,0,5,1}$	536759.12	2.2	8.2	4.0	9.2	25.73
$1_{-1,1,5,1} \rightarrow 1_{1,0,5,1}$	536779.69	0.6	8.3	3.8	2.2	25.76
$1_{-1,1,5,1} \rightarrow 1_{1,0,5,0}$	536793.54	1.0	8.3	4.1	4.2	25.76
CH $^+$						
Transition J	Frequency MHz	T_A (K)	V_{lsr} (km s $^{-1}$)	V_{FWHM} (km s $^{-1}$)	$\int T_A dV$ (K km s $^{-1}$)	E_u (K)

$1 \rightarrow 0$	835135.84	4.0	8.3	4.8	20.4	40.08	
A-CH ₃ OH							
Transition J $+K, v_t^{\pi}$	Frequency MHz	T_A (K)	V_{lsr} (km s ⁻¹)	V_{FWHM} (km s ⁻¹)	$\int T_A dV$ (K km s ⁻¹)	E_u (K)	
$3_{2,0^+} \rightarrow 3_{1,0^-}$	480269.83	0.7	6.7	3.7	2.7	51.64	
$2_{2,0^+} \rightarrow 2_{1,0^-}$	481505.55	0.7	6.1	3.3	2.4	44.67	
$10_{0,0^+} \rightarrow 9_{0,0^+}$	483141.47	1.5	6.6	4.3	6.9	127.6	
$10_{2,0^-} \rightarrow 9_{2,0^-}$	483388.95	0.3	6.8	4.9	1.4	165.35	
$10_{3,0^+} \rightarrow 9_{3,0^+}$	483553.40	0.2	5.5	6.4	1.7	177.46	
$10_{3,0^-} \rightarrow 9_{3,0^-}$	483566.43	0.3	6.5	3.9	1.2	177.46	
$10_{2,0^+} \rightarrow 9_{2,0^+}$	483762.05	0.2	6.6	5.7	1.4	165.4	
$2_{2,0^-} \rightarrow 2_{1,0^+}$	484005.49	0.7	6.5	4.2	3.0	44.67	
$3_{2,0^-} \rightarrow 3_{1,0^+}$	485263.94	0.8	6.6	4.0	3.5	51.64	
$4_{2,0^-} \rightarrow 4_{1,0^+}$	486941.55	0.9	6.5	4.1	3.7	60.92	
$10_{1,0^-} \rightarrow 9_{1,0^-}$	487532.70	0.6	6.5	4.4	2.9	143.28	
$5_{2,0^-} \rightarrow 5_{1,0^+}$	489037.53	0.8	6.6	4.1	3.5	72.53	
$6_{2,0^-} \rightarrow 6_{1,0^+}$	491551.87	0.7	6.3	4.1	2.9	86.46	
$4_{1,0^+} \rightarrow 3_{0,0^+}$	492279.27	2.0	6.7	4.2	8.8	37.55	
$5_{3,0^+} \rightarrow 4_{2,0^+}$	493699.96	1.3	6.5	3.7	5.1	84.62	
$5_{3,0^-} \rightarrow 4_{2,0^-}$	493734.65	1.4	6.4	3.7	5.3	84.62	
$7_{2,0^-} \rightarrow 7_{1,0^+}$	494482.35	0.6	6.5	4.3	2.6	102.7	
$8_{2,0^-} \rightarrow 8_{1,0^+}$	497829.07	0.4	6.4	4.3	2.0	121.27	
$9_{2,0^-} \rightarrow 9_{1,0^+}$	501589.39	0.4	6.7	4.0	1.5	142.15	
$10_{2,0^-} \rightarrow 10_{1,0^+}$	505762.88	0.3	6.4	4.5	1.3	165.35	
$11_{2,0^-} \rightarrow 11_{1,0^+}$	510345.79	0.2	6.4	4.7	1.0	190.86	
$16_{0,0^+} \rightarrow 15_{1,0^+}$	515170.91	0.2	6.6	4.9	1.1	315.21	
$11_{1,0^+} \rightarrow 10_{1,0^+}$	527054.34	0.4	6.5	3.9	1.6	166.37	
$11_{0,0^+} \rightarrow 10_{0,0^+}$	531320.09	1.2	6.6	4.3	5.4	153.1	
$11_{2,0^-} \rightarrow 10_{2,0^-}$	531636.16	0.2	7.1	6.9	1.7	190.87	
$11_{4,0^-} \rightarrow 10_{4,0^-}$	531869.53	0.4	7.5	6.2	2.3	233.52	
$11_{3,0^-} \rightarrow 10_{3,0^-}$	531893.14	0.3	6.9	4.8	1.4	202.98	
$11_{2,0^+} \rightarrow 10_{2,0^+}$	532133.99	0.3	6.2	4.1	1.1	190.94	
$11_{1,0^-} \rightarrow 10_{1,0^-}$	536192.13	0.6	6.4	3.7	2.4	169.01	
$5_{1,0^+} \rightarrow 4_{0,0^+}$	538571.19	2.1	6.7	4.4	9.7	49.06	
$6_{3,0^+} \rightarrow 5_{2,0^+}$	542002.05	1.2	6.4	3.7	4.7	98.55	
$6_{3,0^-} \rightarrow 5_{2,0^-}$	542082.94	1.2	6.5	3.7	4.7	98.55	
$12_{1,0^+} \rightarrow 11_{1,0^+}$	574869.74	0.3	6.3	4.2	1.4	193.96	
$2_{2,0^-} \rightarrow 1_{1,0^-}$	579085.75	1.3	6.5	3.7	5.2	44.67	

$12_{0,0}^+ \rightarrow 11_{0,0}^+$	579460.65	0.9	6.5	4.4	4.0	180.91
$2_{2,0}^+ \rightarrow 1_{1,0}^+$	579922.27	1.3	6.5	4.1	5.7	44.67
$12_{3,0}^+ \rightarrow 11_{3,0}^+$	580176.81	0.2	6.6	4.2	0.8	230.83
$12_{3,0}^- \rightarrow 11_{3,0}^-$	580212.19	0.2	7.3	5.3	1.1	230.83
$12_{2,0}^+ \rightarrow 11_{2,0}^+$	580503.31	0.2	6.3	4.5	0.9	218.8
$6_{1,0}^+ \rightarrow 5_{0,0}^+$	584450.72	2.5	6.6	4.3	11.3	62.87
$12_{1,0}^- \rightarrow 11_{1,0}^-$	584823.31	0.4	6.6	5.3	2.5	197.08
$7_{3,0}^+ \rightarrow 6_{2,0}^+$	590278.73	1.0	6.5	3.9	4.3	114.79
$7_{3,0}^- \rightarrow 6_{2,0}^-$	590441.53	1.0	6.4	3.8	4.1	114.79
$13_{1,0}^+ \rightarrow 12_{1,0}^+$	622660.02	0.3	6.4	4.3	1.4	223.85
$3_{2,0}^- \rightarrow 2_{1,0}^-$	626627.34	1.4	6.5	3.9	5.5	51.64
$13_{0,0}^+ \rightarrow 12_{0,0}^+$	627559.43	0.6	6.5	5.4	3.4	211.03
$13_{2,0}^- \rightarrow 12_{2,0}^-$	628052.23	0.2	6.8	6.0	1.2	248.84
$13_{3,0}^+ \rightarrow 12_{3,0}^+$	628471.51	0.2	6.2	6.3	1.3	260.99
$13_{4,0}^- \rightarrow 12_{4,0}^-$	628513.72	0.2	6.3	3.5	0.7	291.53
$13_{3,0}^- \rightarrow 12_{3,0}^-$	628524.83	0.2	7.1	5.3	1.1	261
$13_{2,0}^+ \rightarrow 12_{2,0}^+$	628868.08	0.2	7.5	5.1	1.1	248.98
$3_{2,0}^+ \rightarrow 2_{1,0}^+$	629141.49	1.4	6.5	4.1	6.2	51.64
$7_{1,0}^+ \rightarrow 6_{0,0}^+$	629922.01	1.6	6.7	4.6	7.9	78.97
$13_{1,0}^- \rightarrow 12_{1,0}^-$	633424.48	0.4	6.3	4.9	2.1	227.48
$7_{4,0}^- \rightarrow 7_{3,0}^+$	636336.97	0.3	7.2	4.1	1.2	145.33
$4_{4,0}^- \rightarrow 4_{3,0}^+$	636422.01	0.5	6.0	2.8	1.5	103.56
$3_{2,0}^- \rightarrow 2_{1,0}^-$	626627.67	1.1	6.3	4.0	4.8	51.64
$13_{0,0}^+ \rightarrow 12_{0,0}^+$	627560.25	0.5	6.1	3.9	2.0	211.03
$3_{2,0}^+ \rightarrow 2_{1,0}^+$	629141.29	1.0	6.6	4.2	4.2	51.64
$7_{1,0}^+ \rightarrow 6_{0,0}^+$	629921.68	1.1	6.8	5.0	5.9	78.97
$13_{1,0}^- \rightarrow 12_{1,0}^-$	633425.22	0.2	6.0	5.2	1.3	227.48
$7_{4,0}^- \rightarrow 7_{3,0}^+$	636335.86	0.3	7.7	4.4	1.4	145.33
$6_{4,0}^+ \rightarrow 6_{3,0}^-$	636365.90	0.3	6.1	4.4	1.6	129.09
$5_{4,0}^- \rightarrow 5_{3,0}^+$	636395.60	0.3	6.1	4.6	1.6	115.16
$4_{4,0}^+ \rightarrow 4_{3,0}^-$	636420.70	0.3	6.6	3.5	1.0	103.56
$8_{3,0}^+ \rightarrow 7_{2,0}^+$	638524.78	0.9	6.4	4.4	4.3	133.36
$8_{3,0}^- \rightarrow 7_{2,0}^-$	638818.88	0.9	6.5	4.4	4.0	133.36
$14_{1,0}^+ \rightarrow 13_{1,0}^+$	670424.18	0.2	6.3	6.8	1.6	256.02
$4_{2,0}^- \rightarrow 3_{1,0}^-$	673747.18	1.3	6.5	4.2	5.8	60.92
$8_{1,0}^+ \rightarrow 7_{0,0}^+$	674991.12	1.3	6.8	4.5	6.2	97.38
$14_{0,0}^+ \rightarrow 13_{0,0}^+$	675613.75	0.5	6.5	5.5	2.8	243.45
$4_{2,0}^+ \rightarrow 3_{1,0}^+$	678786.36	1.4	6.5	3.9	5.9	60.93
$14_{1,0}^- \rightarrow 13_{1,0}^-$	681991.47	0.3	6.3	6.9	2.2	260.21
$9_{3,0}^+ \rightarrow 8_{2,0}^+$	686733.14	0.7	6.3	4.0	2.8	154.25
$9_{3,0}^- \rightarrow 8_{2,0}^-$	687225.61	0.7	6.6	4.7	3.6	154.25

$9_{1,0^+} \rightarrow 8_{0,0^+}$	719665.76	1.0	6.6	5.2	5.7	118.08
$5_{2,0^-} \rightarrow 4_{1,0^-}$	720442.77	1.1	6.5	3.9	4.6	72.53
$15_{0,0^+} \rightarrow 14_{0,0^+}$	723621.75	0.4	6.0	4.8	1.8	278.18
$9_{1,0^+} \rightarrow 8_{0,0^+}$	719665.58	1.1	6.7	4.6	5.4	118.08
$5_{2,0^-} \rightarrow 4_{1,0^-}$	720442.56	1.3	6.5	4.1	5.7	72.53
$15_{0,0^+} \rightarrow 14_{0,0^+}$	723620.68	0.4	6.4	6.1	2.8	278.18
$5_{2,0^+} \rightarrow 4_{1,0^+}$	728863.72	1.4	6.5	4.3	6.3	72.53
$15_{1,0^-} \rightarrow 14_{1,0^-}$	730520.33	0.3	6.7	5.1	1.5	295.27
$10_{3,0^+} \rightarrow 9_{2,0^+}$	734895.06	0.5	6.5	5.1	2.8	177.46
$10_{3,0^-} \rightarrow 9_{2,0^-}$	735674.32	0.6	6.5	5.0	3.0	177.46
$10_{1,0^+} \rightarrow 9_{0,0^+}$	763953.80	0.8	6.8	5.5	4.5	141.08
$6_{2,0^-} \rightarrow 5_{1,0^-}$	766711.66	1.0	6.5	3.8	4.0	86.46
$16_{1,0^-} \rightarrow 15_{1,0^-}$	779006.31	0.4	7.9	4.2	1.9	332.65
$6_{2,0^+} \rightarrow 5_{1,0^+}$	779381.81	1.2	6.4	4.3	5.3	86.46
$11_{3,0^+} \rightarrow 10_{2,0^+}$	783002.74	0.4	6.6	4.1	1.9	202.98
$11_{3,0^-} \rightarrow 10_{2,0^-}$	784178.53	0.4	6.6	4.8	1.8	202.99
$11_{1,0^+} \rightarrow 10_{0,0^+}$	807866.57	0.6	6.8	5.2	3.1	166.37
$7_{2,0^-} \rightarrow 6_{1,0^-}$	812551.63	0.8	6.5	4.4	3.8	102.7
$4_{4,0^-} \rightarrow 3_{3,0^-}$	829891.72	0.7	6.9	4.6	3.1	103.56
$7_{2,0^+} \rightarrow 6_{1,0^+}$	830351.20	0.9	6.3	4.2	4.0	102.72
$12_{3,0^+} \rightarrow 11_{2,0^+}$	831048.06	0.3	5.9	4.4	1.4	230.83
$12_{3,0^-} \rightarrow 11_{2,0^-}$	832755.31	0.3	6.4	5.3	1.8	230.83
$12_{1,0^+} \rightarrow 11_{0,0^+}$	851415.12	0.6	7.0	4.7	3.0	193.96
$8_{2,0^-} \rightarrow 7_{1,0^-}$	857960.16	0.6	6.6	3.8	2.4	121.27
$5_{4,0^+} \rightarrow 4_{3,0^+}$	878227.11	0.6	6.8	4.5	2.7	115.16
$13_{3,0^+} \rightarrow 12_{2,0^+}$	879015.02	0.3	6.3	5.9	1.6	260.99
$13_{3,0^-} \rightarrow 12_{2,0^-}$	881420.97	0.3	6.9	6.6	1.8	261
$8_{2,0^+} \rightarrow 7_{1,0^+}$	881783.47	0.7	6.5	4.5	3.6	121.29
$13_{1,0^+} \rightarrow 12_{0,0^+}$	894614.92	0.4	6.8	4.7	1.9	223.84
$13_{1,0^-} \rightarrow 12_{0,0^-}$	894614.92	0.4	6.8	4.7	1.9	223.84
$9_{2,0^-} \rightarrow 8_{1,0^-}$	902936.66	0.4	6.4	5.3	2.5	142.15
$6_{4,0^+} \rightarrow 5_{3,0^+}$	926555.20	0.4	7.0	5.3	2.5	129.09
$9_{2,0^+} \rightarrow 8_{1,0^+}$	933694.55	0.6	6.5	4.6	2.7	142.19
$14_{1,0^+} \rightarrow 13_{0,0^+}$	937479.55	0.3	6.6	5.8	2.0	256.02
$7_{4,0^-} \rightarrow 6_{3,0^-}$	974878.74	0.4	6.4	6.4	2.9	145.33
$10_{2,0^+} \rightarrow 9_{1,0^+}$	986100.37	0.5	6.2	5.1	3.0	165.4
$8_{4,0^+} \rightarrow 7_{3,0^+}$	1023196.7	0.5	7.2	4.4	2.2	163.9

3

E-CH₃OH

Transition $J_{\pm K, v_t}$	Frequency MHz	T_A (K)	V_{lsr} (km s ⁻¹)	V_{FWHM} (km s ⁻¹)	$\int T_A dV$ (K km s ⁻¹)	E_u (K)
$10_{0,0} \rightarrow 9_{0,0}$	482283.13	0.7	6.4	3.8	2.8	132.71
$10_{-1,0} \rightarrow 9_{-1,0}$	482959.74	1.4	6.4	3.9	5.7	125.25
$10_{1,0} \rightarrow 9_{1,0}$	483687.10	0.5	6.5	3.9	2.2	140.83
$10_{2,0} \rightarrow 9_{2,0}$	484023.82	0.6	6.6	4.5	3.0	142.08
$10_{-2,0} \rightarrow 9_{-2,0}$	484072.13	0.3	6.8	5.0	1.6	145.73
$7_{0,0} \rightarrow 6_{-1,0}$	495173.84	1.2	6.6	3.9	4.8	70.18
$7_{1,0} \rightarrow 6_{0,0}$	504294.53	1.2	6.4	3.6	4.7	248.24
$11_{1,0} \rightarrow 10_{2,0}$	506153.78	0.2	6.6	5.1	1.0	166.37
$10_{2,0} \rightarrow 9_{1,0}$	509564.94	0.7	6.8	5.2	3.9	142.08
$2_{-2,0} \rightarrow 1_{-1,0}$	520179.58	1.1	6.7	4.1	5.0	24.96
$14_{-1,0} \rightarrow 13_{0,0}$	523275.25	0.3	6.5	4.9	1.4	241.04
$8_{3,0} \rightarrow 8_{2,0}$	530123.52	0.3	6.9	5.4	1.7	123.38
$11_{0,0} \rightarrow 10_{0,0}$	530184.87	0.5	6.6	4.6	2.5	158.15
$7_{3,0} \rightarrow 7_{2,0}$	530316.84	0.3	6.6	4.9	1.8	104.81
$6_{3,0} \rightarrow 6_{2,0}$	530455.52	0.4	6.5	4.1	1.9	88.56
$5_{3,0} \rightarrow 5_{2,0}$	530549.77	0.4	6.7	4.6	2.2	74.63
$4_{3,0} \rightarrow 4_{2,0}$	530611.06	0.4	6.6	4.3	2.0	63.03
$3_{3,0} \rightarrow 3_{2,0}$	530647.07	0.4	7.1	5.0	2.1	53.74
$11_{-1,0} \rightarrow 10_{-1,0}$	531080.10	1.1	6.5	4.3	4.9	150.74
$11_{1,0} \rightarrow 10_{1,0}$	532032.12	0.4	6.6	5.2	2.2	166.37
$11_{2,0} \rightarrow 10_{2,0}$	532467.35	0.5	6.4	4.6	2.7	167.63
$11_{-2,0} \rightarrow 10_{-2,0}$	532567.79	0.3	6.4	5.2	1.7	171.29
$8_{0,0} \rightarrow 7_{-1,0}$	543076.99	1.1	6.6	4.5	5.2	88.72
$8_{1,0} \rightarrow 7_{0,0}$	553147.29	0.9	6.4	3.6	3.6	96.73
$11_{2,0} \rightarrow 10_{1,0}$	558345.87	0.4	6.3	4.3	1.9	167.63
$11_{2,0} \rightarrow 10_{1,0}$	558345.39	0.5	6.6	4.5	2.3	167.63
$3_{-2,0} \rightarrow 2_{-1,0}$	568566.84	1.2	6.6	4.3	5.6	31.93
$15_{-1,0} \rightarrow 14_{0,0}$	572900.17	0.2	6.2	5.0	1.2	275.74
$12_{0,0} \rightarrow 11_{0,0}$	578007.58	0.4	6.4	4.6	1.9	185.89
$12_{-1,0} \rightarrow 11_{-1,0}$	579151.93	0.7	6.5	4.4	3.5	178.53
$12_{1,0} \rightarrow 11_{1,0}$	580369.39	0.3	6.6	4.5	1.5	194.22
$12_{2,0} \rightarrow 11_{2,0}$	580903.85	0.4	6.4	4.9	2.2	195.51
$12_{-2,0} \rightarrow 11_{-2,0}$	581092.64	0.3	6.5	4.8	1.3	199.18
$9_{0,0} \rightarrow 8_{-1,0}$	590791.90	0.8	6.5	4.1	3.7	109.56
$9_{1,0} \rightarrow 8_{0,0}$	602234.23	0.8	6.4	4.0	3.4	117.62
$12_{2,0} \rightarrow 11_{1,0}$	607217.09	0.3	6.4	5.2	1.7	195.51
$4_{-2,0} \rightarrow 3_{-1,0}$	616980.70	1.2	6.6	4.1	5.1	41.22
$16_{-1,0} \rightarrow 15_{0,0}$	622775.50	0.2	6.1	5.0	1.0	312.73
$13_{0,0} \rightarrow 12_{0,0}$	625750.66	0.3	6.4	5.4	1.7	215.92

$13_{-1,0} \rightarrow 12_{-1,0}$	627171.60	0.6	6.5	4.9	3.0	208.64
$13_{1,0} \rightarrow 12_{1,0}$	628698.28	0.2	6.1	5.0	1.1	224.39
$13_{3,0} \rightarrow 12_{3,0}$	628817.62	0.2	6.3	4.0	0.8	251.06
$13_{2,0} \rightarrow 12_{2,0}$	629322.36	0.4	6.7	5.0	2.0	225.71
$13_{-2,0} \rightarrow 12_{-2,0}$	629653.22	0.2	6.3	7.8	1.9	229.4
$13_{-1,0} \rightarrow 12_{-1,0}$	627171.35	0.5	6.6	4.4	2.3	208.64
$13_{2,0} \rightarrow 12_{2,0}$	629321.48	0.3	7.1	6.0	1.6	225.71
$13_{-2,0} \rightarrow 12_{-2,0}$	629651.72	0.2	7.0	5.2	1.1	229.4
$10_{0,0} \rightarrow 9_{-1,0}$	638280.27	0.7	6.7	4.4	3.1	132.71
$10_{1,0} \rightarrow 9_{0,0}$	651618.53	0.6	6.5	4.6	2.9	140.83
$13_{2,0} \rightarrow 12_{1,0}$	656166.61	0.6	8.1	6.4	3.8	225.71
$5_{-2,0} \rightarrow 4_{-1,0}$	665443.13	1.2	6.7	4.3	5.2	52.83
$14_{0,0} \rightarrow 13_{0,0}$	673416.97	0.3	6.6	4.9	1.4	248.24
$14_{-1,0} \rightarrow 13_{-1,0}$	675135.73	0.4	6.5	6.0	2.8	241.04
$3_{3,0} \rightarrow 2_{2,0}$	675773.95	0.7	6.8	4.9	3.6	53.74
$14_{1,0} \rightarrow 13_{1,0}$	677011.82	0.2	7.5	8.3	2.1	256.88
$14_{2,0} \rightarrow 13_{2,0}$	677711.91	0.3	6.1	4.9	1.7	258.24
$11_{0,0} \rightarrow 10_{-1,0}$	685505.14	0.5	7.0	5.9	3.2	158.15
$6_{-2,0} \rightarrow 5_{-1,0}$	713983.43	0.9	6.6	4.1	3.9	66.76
$6_{-2,0} \rightarrow 5_{-1,0}$	713983.43	0.9	6.6	4.1	3.9	66.76
$4_{-4,0} \rightarrow 3_{-3,0}$	718436.93	0.8	6.7	4.0	3.5	103.22
$15_{-1,0} \rightarrow 14_{-1,0}$	723040.58	0.4	6.9	5.4	2.0	275.74
$4_{3,0} \rightarrow 3_{2,0}$	724122.89	0.6	6.5	5.7	3.4	63.03
$4_{3,0} \rightarrow 3_{2,0}$	724122.10	0.8	6.8	5.3	4.2	63.03
$12_{0,0} \rightarrow 11_{-1,0}$	732433.68	0.4	6.4	5.1	2.2	185.89
$12_{1,0} \rightarrow 11_{0,0}$	751552.50	0.4	6.4	5.8	2.3	194.22
$7_{-2,0} \rightarrow 6_{-1,0}$	762636.47	0.7	6.7	4.4	3.4	83.02
$9_{-3,0} \rightarrow 9_{-2,0}$	766028.92	0.3	6.7	5.2	1.4	159.27
$8_{-3,0} \rightarrow 8_{-2,0}$	766396.97	0.4	6.6	5.9	2.3	138.38
$7_{-3,0} \rightarrow 7_{-2,0}$	766648.47	0.4	6.6	4.5	1.9	119.81
$5_{-4,0} \rightarrow 4_{-3,0}$	766761.68	0.8	6.6	3.3	2.9	114.82
$6_{-3,0} \rightarrow 6_{-2,0}$	766811.56	0.4	6.6	2.6	1.1	103.56
$5_{-3,0} \rightarrow 5_{-2,0}$	766908.51	0.4	6.8	4.2	1.9	89.63
$4_{-3,0} \rightarrow 4_{-2,0}$	766961.54	0.5	6.4	3.4	1.6	78.03
$3_{-3,0} \rightarrow 3_{-2,0}$	766983.75	0.4	6.4	3.1	1.2	68.74
$5_{3,0} \rightarrow 4_{2,0}$	772453.48	0.5	7.2	7.1	4.0	74.63
$13_{0,0} \rightarrow 12_{-1,0}$	779030.27	0.4	7.2	6.0	2.2	215.92
$8_{-2,0} \rightarrow 7_{-1,0}$	811444.68	0.5	7.0	6.0	3.4	101.6
$6_{-4,0} \rightarrow 5_{-3,0}$	815071.72	0.7	6.6	4.3	3.1	128.75
$6_{3,0} \rightarrow 5_{2,0}$	820764.66	0.4	6.2	4.4	1.8	88.56
$9_{-2,0} \rightarrow 8_{-1,0}$	860459.44	0.4	7.0	5.5	2.4	122.5

$7_{-4,0} \rightarrow 6_{-3,0}$	863365.78	0.5	6.7	5.2	2.9	145
$7_{3,0} \rightarrow 6_{2,0}$	869039.06	0.5	6.6	5.2	2.6	104.81
$10_{-2,0} \rightarrow 9_{-1,0}$	909738.07	0.3	6.9	4.7	1.6	145.73
$8_{-4,0} \rightarrow 7_{-3,0}$	911643.69	0.4	6.5	4.5	2.1	163.56
$3_{-3,0} \rightarrow 2_{-2,0}$	912109.65	0.7	6.6	5.1	3.5	68.74
$8_{3,0} \rightarrow 7_{2,0}$	917269.03	0.4	7.3	4.9	1.9	123.38
$4_{-3,0} \rightarrow 3_{-2,0}$	960473.04	0.6	6.4	5.3	3.1	78.03

CN, v=0

Transition N_{J,F_1}	Frequency MHz	T_A (K)	V_{lsr} (km s ⁻¹)	V_{FWHM} (km s ⁻¹)	$\int T_A dV$ (K km s ⁻¹)	E_u (K)
$5_{4,5,5,5} \rightarrow 4_{3,5,4,5}$	566729.48	1.3	7.3	5.3	7.3	81.59
$5_{5,5,5,5} \rightarrow 4_{4,5,4,5}$	566946.10	1.6	7.6	5.6	9.8	81.64
$6_{5,5,6,5} \rightarrow 5_{4,5,5,5}$	680046.29	0.5	7.5	5.4	3.0	114.23
$6_{6,5,6,5} \rightarrow 5_{5,5,5,5}$	680263.15	0.7	7.5	5.4	4.1	114.29
$7_{6,5,7,5} \rightarrow 6_{5,5,6,5}$	793337.05	0.3	7.3	6.9	2.2	152.38
$7_{7,5,7,5} \rightarrow 6_{6,5,6,5}$	793552.12	0.3	7.6	6.4	1.8	152.38

CO

	Transition J	Frequency MHz	T_A (K)	V_{lsr} (km s ⁻¹)	V_{FWHM} (km s ⁻¹)	$\int T_A dV$ (K km s ⁻¹)	E_u (K)
Main	$5 \rightarrow 4$	576267.41	52.5	7.3	6.3	352.5	82.98
Wing	$5 \rightarrow 4$	576267.63	7.7	7.2	19.1	156.7	82.98
Main	$6 \rightarrow 5$	691472.71	48.2	7.2	5.8	299.0	116.16
Wing	$6 \rightarrow 5$	691472.71	11.9	7.2	17.6	222.7	116.16
Main	$7 \rightarrow 6$	806653.11	46.6	6.5	5.0	248.5	154.88
Wing	$7 \rightarrow 6$	806651.38	7.8	7.2	22.4	185.5	154.88
Main	$8 \rightarrow 7$	921801.29	45.2	6.5	5.1	244.5	199.11
Wing	$8 \rightarrow 7$	921799.21	7.3	7.2	23.8	184.5	199.11
Main	$9 \rightarrow 8$	1036911.45	45.8	7.3	6.0	292.2	248.88
Wing	$9 \rightarrow 8$	1036911.85	11.7	7.2	18.0	223.7	248.88
Main	$10 \rightarrow 9$	1151987.56	39.3	6.5	4.6	194.1	304.17
Wing	$10 \rightarrow 9$	1151987.37	5.5	6.5	23.0	134.4	304.17
Main	$11 \rightarrow 10$	1267014.10	31.2	7.1	5.0	166.0	364.97
Wing	$11 \rightarrow 10$	1267016.60	10.8	6.5	15.0	173.1	367.97
Main	$13 \rightarrow 12$	1496920.46	29.8	7.5	4.8	152.8	503.14
Wing	$13 \rightarrow 12$	1496925.41	8.7	6.5	18.2	167.9	503.14
Main	$14 \rightarrow 13$	1611790.99	28.5	7.5	4.9	148.6	580.5
Wing	$14 \rightarrow 13$	1611792.67	4.9	7.2	21.9	114.6	580.5
Main	$15 \rightarrow 14$	1726597.84	20.4	7.8	3.5	75.5	663.36
Wing	$15 \rightarrow 14$	1726601.59	6.2	7.2	14.0	92.3	663.36

Main	16 → 15	1841340.61	14.0	7.8	4.0	59.4	751.73
Wing	16 → 15	1841344.53	4.0	7.2	15.0	63.2	751.73

¹³CO

Transition J	Frequency MHz	T _A (K)	V _{lsr} (km s ⁻¹)	V _{FWHM} (km s ⁻¹)	∫T _A dV (K km s ⁻¹)	E _u (K)
5 → 4	550925.82	30.9	7.3	4.8	157.6	79.33
6 → 5	661066.67	30.8	7.3	4.7	155.2	111.05
7 → 6	771182.86	28.0	7.5	5.1	152.0	148.06
8 → 7	881271.54	22.6	7.4	4.7	112.0	190.36
9 → 8	991327.01	17.5	7.7	4.7	87.8	237.94
10 → 9	1101346.80	13.1	7.8	4.6	64.4	290.79
11 → 10	1211327.07	6.7	7.6	4.3	31.0	348.93

C¹⁸O

Transition J	Frequency MHz	T _A (K)	V _{lsr} (km s ⁻¹)	V _{FWHM} (km s ⁻¹)	∫T _A dV (K km s ⁻¹)	E _u (K)
5 → 4	548831.12	8.5	6.8	4.1	36.4	79.02
6 → 5	658553.65	8.0	6.9	3.7	31.5	110.63
7 → 6	768252.15	5.8	7.0	4.1	25.4	147.5
8 → 7	877922.54	3.5	6.9	5.0	18.7	189.64
9 → 8	987559.09	2.2	7.6	5.9	13.8	237.03
10 → 9	1097163.80	1.5	6.8	3.2	5.1	289.69

C¹⁷O

Transition J	Frequency MHz	T _A (K)	V _{lsr} (km s ⁻¹)	V _{FWHM} (km s ⁻¹)	∫T _A dV (K km s ⁻¹)	E _u (K)
5 → 4	561713.01	3.0	6.7	3.7	11.9	80.88
6 → 5	674009.48	2.4	6.6	3.7	9.3	113.23
7 → 6	786282.9 ^b	—	6.5	4.5	7.6	150.96
8 → 7	898523.38	0.9	7.0	4.1	4.0	194.09
9 → 8	1010731.41	0.4	7.2	3.5	1.5	242.59
10 → 9	1122902.89	0.2	7.4	4.2	1.1	296.49

¹³C¹⁸O

Transition J	Frequency MHz	T _A (K)	V _{lsr} (km s ⁻¹)	V _{FWHM} (km s ⁻¹)	∫T _A dV (K km s ⁻¹)	E _u (K)
5 → 4	523484.35	0.1	6.9	4.1	0.6	75.37
6 → 5	628141.57	0.1	6.6	2.6	0.3	105.52

CS,v=0

	Transition J	Frequency MHz	T_A (K)	V_{lsr} (km s ⁻¹)	V_{FWHM} (km s ⁻¹)	$\int T_A dV$ (K km s ⁻¹)	E_u (K)
Main	10 \rightarrow 9	489750.85	4.1	7.3	4.3	18.8	129.29
Wing	10 \rightarrow 9	489750.92	0.6	6.7	7.8	4.6	129.29
Main	11 \rightarrow 10	538688.84	3.3	7.2	4.7	16.5	155.15
Wing	11 \rightarrow 10	538688.92	0.3	7.0	16.9	4.5	155.15
Main	12 \rightarrow 11	587616.41	2.2	7.1	4.9	11.2	183.35
Wing	12 \rightarrow 11	587619.04	0.2	6.5	12.9	2.4	183.35
Main	13 \rightarrow 12	636532.25	1.0	7.2	5.3	5.8	213.9
Wing	13 \rightarrow 12	636531.41	0.2	8.0	15.0	3.9	213.9
Main	14 \rightarrow 13	685435.93	1.0	7.0	6.0	6.6	246.79
Wing	14 \rightarrow 13	–	–	–	–	–	246.79
Main	15 \rightarrow 14	734325.78	0.6	6.7	5.1	3.1	282.04
Wing	15 \rightarrow 14	734327.70	0.2	6.5	20.4	4.8	282.04
Main	16 \rightarrow 15	783201.36	0.3	7.2	5.0	1.4	319.62
Wing	16 \rightarrow 15	783203.40	0.3	7.0	10.3	2.9	319.62
Main	17 \rightarrow 16	832061.55	0.4	6.6	6.1	2.9	359.56
Wing	17 \rightarrow 16	–	–	–	–	–	359.56
Main	18 \rightarrow 17	880903.85	0.3	7.2	9.0	2.9	401.83
Wing	18 \rightarrow 17	–	–	–	–	–	401.83

¹³CS

	Transition J	Frequency MHz	T_A (K)	V_{lsr} (km s ⁻¹)	V_{FWHM} (km s ⁻¹)	$\int T_A dV$ (K km s ⁻¹)	E_u (K)
	11 \rightarrow 10	508535.83	0.1	7.1	6.1	0.5	146.46

C³⁴S

	Transition J	Frequency MHz	T_A (K)	V_{lsr} (km s ⁻¹)	V_{FWHM} (km s ⁻¹)	$\int T_A dV$ (K km s ⁻¹)	E_u (K)
	10 \rightarrow 9	481916.67	0.3	6.8	4.6	1.4	127.23
	11 \rightarrow 10	530071.15	0.2	7.5	5.3	1.0	152.67
	12 \rightarrow 11	578215.88	0.2	7.6	7.3	1.3	180.42

DCN,v=0

	Transition N_k	Frequency MHz	T_A (K)	V_{lsr} (km s ⁻¹)	V_{FWHM} (km s ⁻¹)	$\int T_A dV$ (K km s ⁻¹)	E_u (K)
	7 ₀ \rightarrow 6 ₀	506825.63	0.2	6.9	5.2	1.0	97.3

DCO⁺

Transition J	Frequency MHz	T_A (K)	V_{lsr} (km s ⁻¹)	V_{FWHM} (km s ⁻¹)	$\int T_A dV$ (K km s ⁻¹)	E_u (K)
7 → 6	504200.27	0.2	7.1	4.4	0.8	96.80
8 → 7	576205.0 ^b	—	—	—	—	124.45
9 → 8	648195.15	0.2	6.1	2.1	0.4	155.56

o-H ₂ S						
Transition $J_{0,\Lambda}$	Frequency MHz	T_A (K)	V_{lsr} (km s ⁻¹)	V_{FWHM} (km s ⁻¹)	$\int T_A dV$ (K km s ⁻¹)	E_u (K)
2 _{2,1} → 2 _{1,2}	505565.22	1.5	7.0	5.0	8.2	59.59
3 _{1,2} → 3 _{0,3}	708470.60	0.4	6.9	7.5	3.5	116.99
2 _{1,2} → 1 _{0,1}	736034.21	4.5	7.4	5.9	27.9	35.32
3 _{0,3} → 2 _{1,2}	993107.06	1.7	5.8	6.3	11.4	82.99
2 _{2,1} → 1 _{1,0}	1072837.04	0.9	7.7	6.0	5.7	59.59

p-H ₂ S						
Transition $J_{0,\Lambda}$	Frequency MHz	T_A (K)	V_{lsr} (km s ⁻¹)	V_{FWHM} (km s ⁻¹)	$\int T_A dV$ (K km s ⁻¹)	E_u (K)
2 _{0,2} → 1 _{1,1}	687303.34	2.4	7.1	5.1	12.7	54.7
3 _{1,3} → 2 _{0,2}	1002777.30	0.6	7.4	5.6	3.8	102.82

H ₂ ³⁴ S						
Transition N_{K_a,K_c}	Frequency MHz	T_A (K)	V_{lsr} (km s ⁻¹)	V_{FWHM} (km s ⁻¹)	$\int T_A dV$ (K km s ⁻¹)	E_u (K)
2 _{1,2} → 1 _{0,1}	734269.67	0.3	6.9	4.1	1.3	55.01

H ₂ CS						
Transition J_{K_a,K_c}	Frequency MHz	T_A (K)	V_{lsr} (km s ⁻¹)	V_{FWHM} (km s ⁻¹)	$\int T_A dV$ (K km s ⁻¹)	E_u (K)
14 _{1,13} → 13 _{1,12}	487664.03	0.2	6.8	4.5	0.8	188.8
15 _{1,15} → 14 _{1,14}	506771.50	0.2	6.6	5.2	1.1	207.86
15 _{0,15} → 14 _{0,14}	513361.94	0.1	6.6	4.0	0.4	197.44
15 _{2,13} → 14 _{2,12}	516336.1 ^b	—	—	—	—	250.71
15 _{1,14} → 14 _{1,13}	522403.63	0.1	6.9	5.1	0.9	213.87
16 _{1,16} → 15 _{1,15}	540465.31	0.1	6.5	3.5	0.5	233.79
17 _{1,17} → 16 _{1,16}	574140.12	0.1	6.8	4.7	0.5	261.35

HF						
Transition J	Frequency MHz	T_A (K)	V_{lsr} (km s ⁻¹)	V_{FWHM} (km s ⁻¹)	$\int T_A dV$ (K km s ⁻¹)	E_u (K)
1 → 0	1232469.17	-1.1	8.7	3.2	-7.0	59.15

o-H ₂ CO						
Transition $J_{K_a K_c}$	Frequency MHz	T_A (K)	V_{lsr} (km s ⁻¹)	V_{FWHM} (km s ⁻¹)	$\int T_A dV$ (K km s ⁻¹)	E_u (K)
7 _{1,7} → 6 _{1,6}	491968.45	3.1	7.0	4.4	14.7	91.15
7 _{5,3} → 6 _{5,2}	509562.12 ^b	–	–	–	–	376.68
7 _{3,5} → 6 _{3,4}	510155.94	0.9	6.9	4.8	4.4	188.73
7 _{3,4} → 6 _{3,3}	510238.04	0.9	6.9	4.4	4.0	188.73
7 _{1,6} → 6 _{1,5}	525666.11	2.5	6.8	4.6	12.2	97.63
8 _{1,8} → 7 _{1,7}	561899.30	2.6	7.0	4.4	12.5	118.12
8 _{5,3} → 7 _{5,2}	582382.77	0.2	6.6	6.3	1.3	404.63
8 _{3,6} → 7 _{3,5}	583144.85	0.6	6.9	5.2	3.2	216.71
8 _{3,5} → 7 _{3,4}	583308.64	0.6	7.0	4.6	2.8	216.73
8 _{1,7} → 7 _{1,6}	600331.09	1.7	6.7	4.5	8.1	126.44
9 _{1,9} → 8 _{1,8}	631703.48	1.5	6.7	4.6	7.3	148.43
9 _{5,5} → 8 _{5,4}	655212.67	0.2	6.7	5.4	1.1	436.08
9 _{3,7} → 8 _{3,6}	656166.83	0.6	6.0	6.2	3.9	248.2
9 _{3,6} → 8 _{3,5}	656465.35	0.5	6.6	4.6	2.3	248.23
9 _{1,8} → 8 _{1,7}	674810.63	1.1	6.6	4.8	5.4	158.83
10 _{1,10} → 9 _{1,9}	701370.13	1.3	7.1	5.1	7.1	182.1
10 _{5,6} → 9 _{5,5}	728052.29	0.2	7.5	5.1	1.0	471.02
10 _{3,8} → 9 _{3,7}	729213.26	0.4	6.7	4.5	2.0	283.2
10 _{3,7} → 9 _{3,6}	729725.77	0.3	6.7	5.9	2.1	283.25
10 _{1,9} → 9 _{1,8}	749072.76	0.8	6.7	4.5	3.8	194.78
11 _{1,11} → 10 _{1,10}	770895.15	0.7	7.4	7.7	5.7	219.09
11 _{1,10} → 10 _{1,9}	823084.31	0.5	6.4	5.1	2.8	234.28
12 _{1,12} → 11 _{1,11}	840277.03	0.5	6.5	4.8	2.5	259.42
12 _{1,11} → 11 _{1,10}	896807.59	0.3	6.2	4.9	1.7	277.32
13 _{1,13} → 12 _{1,12}	909511.04	0.3	5.9	6.0	2.0	303.07

p-H ₂ CO						
Transition $J_{K_a K_c}$	Frequency MHz	T_A (K)	V_{lsr} (km s ⁻¹)	V_{FWHM} (km s ⁻¹)	$\int T_A dV$ (K km s ⁻¹)	E_u (K)
7 _{0,7} → 6 _{0,6}	505834.17	1.7	6.7	4.0	7.2	97.44
7 _{2,6} → 6 _{2,5}	509146.74	0.8	6.7	4.2	3.4	144.93

$7_{4,4} \rightarrow 6_{4,3}$	509830.59	0.2	6.4	4.2	1.0	286.17
$7_{2,5} \rightarrow 6_{2,4}$	513076.79	0.7	6.7	4.5	3.2	145.35
$8_{0,8} \rightarrow 7_{0,7}$	576709.19	1.1	6.6	4.2	4.9	125.12
$8_{2,7} \rightarrow 7_{2,6}$	581612.27	0.5	6.8	4.3	2.3	172.84
$8_{4,5} \rightarrow 7_{4,4}$	582723.54	0.2	6.7	5.7	1.2	314.14
$8_{2,6} \rightarrow 7_{2,5}$	587454.12	0.5	6.8	4.8	2.4	173.55
$9_{0,9} \rightarrow 8_{0,8}$	647082.69	0.9	6.6	4.1	3.7	156.18
$9_{2,8} \rightarrow 8_{2,7}$	653971.43	0.4	6.4	4.6	1.9	204.23
$9_{4,6} \rightarrow 8_{4,5}$	655640.45	0.2	6.8	6.0	1.2	345.6
$9_{2,7} \rightarrow 8_{2,6}$	662209.75	0.4	6.7	4.5	1.9	205.33
$10_{0,10} \rightarrow 9_{0,9}$	716939.12	0.4	6.7	5.6	2.4	190.58
$10_{2,9} \rightarrow 9_{2,8}$	726209.22	0.3	6.6	6.5	2.0	239.08
$10_{2,8} \rightarrow 9_{2,7}$	737342.68	0.3	7.0	5.3	1.7	380.57
$11_{0,11} \rightarrow 10_{0,10}$	786282.9 ^b	–	6.5	4.5	7.6	228.32

o-H₂O

	Transition $J_{K-1,K+1}$	Frequency MHz	T_A (K)	V_{lsr} (km s ⁻¹)	V_{FWHM} (km s ⁻¹)	$\int T_A dV$ (K km s ⁻¹)	E_u (K)
Main	$1_{1,0} \rightarrow 1_{0,1}$	556935.64	6.2	7.2	7.8	51.9	26.73
Wing	$1_{1,0} \rightarrow 1_{0,1}$	556939.86	1.4	4.9	34.3	52.1	26.73
Main	$5_{3,2} \rightarrow 4_{4,1}$	620704.48	0.5	5.3	2.0	1.1	697.84
Wing	$5_{3,2} \rightarrow 4_{4,1}$	620704.48	–	–	–	–	697.84
Main	$3_{1,2} \rightarrow 3_{0,3}$	1097364.47	1.5	7.1	5.1	8.2	215.2
Wing	$3_{1,2} \rightarrow 3_{0,3}$	1097371.43	2.0	5.2	14.8	31.2	215.2
Main	$3_{1,2} \rightarrow 2_{2,1}$	1153127.12	1.6	6.9	5.3	8.9	215.203
Wing	$3_{1,2} \rightarrow 2_{2,1}$	1153133.21	2.6	5.3	19.2	53.7	215.2
Main	$3_{2,1} \rightarrow 3_{1,2}$	1162913.04	2.9	6.6	4.3	13.4	271.01
Wing	$3_{2,1} \rightarrow 3_{1,2}$	1162914.76	1.4	6.2	18.6	28.4	271.01

p-H₂CO

	Transition $J_{K-1,K+1}$	Frequency MHz	T_A (K)	V_{lsr} (km s ⁻¹)	V_{FWHM} (km s ⁻¹)	$\int T_A dV$ (K km s ⁻¹)	E_u (K)
Main	$2_{1,1} \rightarrow 2_{0,2}$	752033.42	5.5	6.9	5.8	33.6	136.94
Wing	$2_{1,1} \rightarrow 2_{0,2}$	752034.00	2.5	6.7	21.8	58.8	136.94
Main	$4_{2,2} \rightarrow 3_{3,1}$	916174.82	0.3	5.9	6.9	2.0	454.34
Wing	$4_{2,2} \rightarrow 3_{3,1}$	916174.82	–	–	–	–	454.34
Main	$2_{0,2} \rightarrow 1_{1,1}$	987927.13	6.1	6.9	7.5	48.6	100.85
Wing	$2_{0,2} \rightarrow 1_{1,1}$	987938.36	2.4	3.5	26.2	66.2	100.85
Main	$1_{1,1} \rightarrow 0_{0,0}$	1113349.92	1.9	5.1	4.5	9.1	53.43

Wing	$1_{1,1} \rightarrow 0_{0,0}$	1113352.60	1.8	4.4	22.3	42.8	53.43
Main	$4_{2,2} \rightarrow 4_{1,3}$	1207638.86	0.3	7.0	13.6	4.2	454.34
Wing	$4_{2,2} \rightarrow 4_{1,3}$	1207638.86	–	–	–	–	454.34
Main	$2_{2,0} \rightarrow 2_{1,1}$	1228791.19	1.2	6.4	5.4	7.2	195.91
Wing	$2_{2,0} \rightarrow 2_{1,1}$	1228791.19	–	–	–	–	195.91

o-H₂¹⁸O

Transition $J_{K-1,K+1,\nu}$	Frequency MHz	T_A (K)	V_{lsr} (km s ⁻¹)	V_{FWHM} (km s ⁻¹)	$\int T_A dV$ (K km s ⁻¹)	E_u (K)
$1_{1,0,0} \rightarrow 1_{0,1,0}$	547676.36	0.2	7.0	5.6	1.43	

HDO

Transition $J_{K-1,K+1}$	Frequency MHz	T_A (K)	V_{lsr} (km s ⁻¹)	V_{FWHM} (km s ⁻¹)	$\int T_A dV$ (K km s ⁻¹)	E_u (K)
$2_{0,2} \rightarrow 1_{1,1}$	490597.00	0.2	6.8	3.9	0.7	66.43
$1_{1,0} \rightarrow 1_{1,1}$	509293.66	0.3	6.3	3.4	1.0	46.76
$2_{1,1} \rightarrow 2_{0,2}$	599927.69	0.2	6.5	2.9	0.7	95.23

HCl

Transition N_J	Frequency MHz	T_A (K)	V_{lsr} (km s ⁻¹)	V_{FWHM} (km s ⁻¹)	$\int T_A dV$ (K km s ⁻¹)	E_u (K)
$1_{1,5} \rightarrow 0_{1,5}$	625901.60	2.1	7.8	4.4	9.9	30.04
$1_{2,5} \rightarrow 0_{1,5}$	625918.76	2.8	7.9	4.1	12.0	30.04
$1_{0,5} \rightarrow 0_{1,5}$	625932.01	1.4	7.9	4.7	7.0	30.04

H³⁷Cl

Transition N_J	Frequency MHz	T_A (K)	V_{lsr} (km s ⁻¹)	V_{FWHM} (km s ⁻¹)	$\int T_A dV$ (K km s ⁻¹)	E_u (K)
$1_{1,5} \rightarrow 0_{1,5}$	624962.48	1.0	8.3	3.1	3.1	29.99
$1_{2,5} \rightarrow 0_{1,5}$	624975.93	1.4	8.1	3.8	5.5	29.99
$1_{0,5} \rightarrow 1_{1,5}$	624986.44	0.6	8.8	5.4	3.6	29.99

HCN

	Transition J	Frequency MHz	T_A (K)	V_{lsr} (km s ⁻¹)	V_{FWHM} (km s ⁻¹)	$\int T_A dV$ (K km s ⁻¹)	E_u (K)
Main	6 → 5	531716.10	7.4	7.1	5.4	43.0	89.32
Wing	6 → 5	531718.60	0.5	6.0	25.3	14.0	89.32

Main	7 → 6	620303.70	5.1	7.2	5.3	28.4	119.09
Wing	7 → 6	620305.69	0.8	5.9	17.1	14.3	119.09
Main	8 → 7	708876.27	2.5	7.4	5.2	13.8	153.11
Wing	8 → 7	708878.31	0.9	6.2	16.0	15.0	153.11
Main	9 → 8	797432.27	0.9	7.6	4.9	4.9	191.38
Wing	9 → 8	797435.00	0.8	6.3	13.5	11.2	191.38
Main	10 → 9	885969.75	0.6	7.4	5.7	3.9	233.9
Wing	10 → 9	885973.43	0.6	6.3	16.0	10.2	233.9
Main	11 → 10	974486.55	0.6	6.5	5.5	3.5	280.67
Wing	11 → 10	–	–	–	–	–	280.67
Main	13 → 12	1151448.54	0.5	5.9	6.2	3.0	386.95
Wing	13 → 12	–	–	–	–	–	386.95

H¹³CN

Transition J	Frequency MHz	T _A (K)	V _{lsr} (km s ⁻¹)	V _{FWHM} (km s ⁻¹)	∫T _A dV (K km s ⁻¹)	E _u (K)
6 → 5	517969.24	0.4	7.3	5.0	2.1	87.01
7 → 6	604266.38	0.2	7.8	7.5	1.7	116.01

HNC

Transition J _{K_aK_c}	Frequency MHz	T _A (K)	V _{lsr} (km s ⁻¹)	V _{FWHM} (km s ⁻¹)	∫T _A dV (K km s ⁻¹)	E _u (K)
6 _{0,0} → 5 _{0,0}	543897.76	1.2	7.0	4.2	5.4	91.37
7 _{0,0} → 6 _{0,0}	634510.41	0.5	7.2	4.5	2.2	121.82

HCO⁺

Transition J	Frequency MHz	T _A (K)	V _{lsr} (km s ⁻¹)	V _{FWHM} (km s ⁻¹)	∫T _A dV (K km s ⁻¹)	E _u (K)
6 → 5	535061.20	15.3	7.2	5.5	90.3	89.88
7 → 6	624208.34	13.8	7.0	5.7	83.7	119.84
8 → 7	713341.48	10.5	6.9	5.3	59.4	154.08
9 → 8	802458.39	7.4	6.9	5.2	41.0	192.59
10 → 9	891558.14	5.6	6.7	5.2	31.2	235.38
11 → 10	980636.88	4.2	6.9	5.3	23.8	282.44
12 → 11	1069695.54	2.5	6.5	5.2	14.0	333.78
13 → 12	1158729.89	1.6	6.3	4.7	7.9	389.39
14 → 13	1247737.53	0.9	6.4	5.0	5.0	449.27

H¹³CO⁺

Transition J	Frequency MHz	T_A (K)	V_{lsr} (km s ⁻¹)	V_{FWHM} (km s ⁻¹)	$\int T_A dV$ (K km s ⁻¹)	E_u (K)
6 → 5	520460.32	1.1	6.7	3.9	4.6	87.43
7 → 6	607175.53	0.7	6.7	3.7	2.7	116.57
8 → 7	693877.57	0.4	6.4	3.4	1.6	149.87
9 → 8	780563.19	0.2	6.9	5.5	1.3	187.33

N₂H⁺

Transition J	Frequency MHz	T_A (K)	V_{lsr} (km s ⁻¹)	V_{FWHM} (km s ⁻¹)	$\int T_A dV$ (K km s ⁻¹)	E_u (K)
6 → 5	558967.76	2.7	6.3	0.1	7.2	93.9
7 → 6	652097.23	2.7	6.3	0.0	6.7	125.19
8 → 7	745211.80	1.6	6.3	0.1	3.7	160.96
9 → 8	838309.70	0.9	6.2	0.2	1.8	201.19
10 → 9	931388.75	0.5	6.0	0.3	1.3	245.89

NH₃

	Transition $N_{K,v}$	Frequency MHz	T_A (K)	V_{lsr} (km s ⁻¹)	V_{FWHM} (km s ⁻¹)	$\int T_A dV$ (K km s ⁻¹)	E_u (K)
Main	1 _{0,0} → 0 _{0,1}	572498.04	3.3	7.1	5.9	20.8	27.48
Wing	1 _{0,0} → 0 _{0,1}	572496.26	0.2	7.5	12.0	2.1	27.48
Absorption	2 _{1,1} → 1 _{1,0}	1215245.71	-0.7	6.5	5.1	-3.9	80.45

NO

	Transition $N_{\Lambda F_1 F_2}$	Frequency MHz	T_A (K)	V_{lsr} (km s ⁻¹)	V_{FWHM} (km s ⁻¹)	$\int T_A dV$ (K km s ⁻¹)	E_u (K)
	6 _{-1,5,5,5} → 5 _{1,4,5,4,5}	551187.85	0.3	6.7	4.6	1.5	84.15
	6 _{1,5,5,4,5} → 5 _{-1,4,5,3,5}	551533.80	0.3	7.1	4.8	1.4	84.25
	6 _{1,6,5,6,5} → 6 _{-1,5,5,5,5}	651433.16	0.3	6.8	5.8	1.7	115.42
	6 _{-1,6,5,5,5} → 6 _{1,5,5,4,5}	651773.27	0.4	6.9	4.3	1.7	115.53

SO

Transition N_J	Frequency MHz	T_A (K)	V_{lsr} (km s ⁻¹)	V_{FWHM} (km s ⁻¹)	$\int T_A dV$ (K km s ⁻¹)	E_u (K)
4 ₃ → 1 ₂	504676.68	0.1	6.8	3.8	0.5	28.68
12 ₁₁ → 11 ₁₀	514853.39	0.7	7.2	6.7	4.7	167.59
12 ₁₂ → 11 ₁₁	516335.63	0.6	7.1	7.6	5.1	174.22
12 ₁₃ → 11 ₁₂	517354.09	0.8	7.3	6.4	5.7	165.78
13 ₁₂ → 12 ₁₁	558087.15	0.4	7.3	5.9	2.4	194.37

$13_{13} \rightarrow 12_{12}$	559319.68	0.4	7.0	6.6	2.7	201.07
$13_{14} \rightarrow 12_{13}$	560178.46	0.5	7.1	5.7	2.7	192.66
$14_{13} \rightarrow 13_{12}$	601257.88	0.4	7.3	9.6	3.7	223.23
$14_{14} \rightarrow 13_{13}$	602291.95	0.3	7.5	9.0	3.2	229.97
$14_{15} \rightarrow 13_{14}$	603021.65	0.4	7.0	8.2	3.5	221.61
$5_4 \rightarrow 2_3$	611551.86	0.1	7.3	3.7	0.4	38.58
$15_{14} \rightarrow 14_{13}$	644377.53	0.3	7.7	9.0	3.3	254.15
$15_{15} \rightarrow 14_{14}$	645253.67	0.3	7.6	9.0	2.8	260.94
$15_{16} \rightarrow 14_{15}$	645874.95	0.3	7.5	10.5	3.8	252.6
$16_{15} \rightarrow 15_{14}$	687457.56	0.3	7.1	12.6	3.4	287.15
$16_{16} \rightarrow 15_{15}$	688204.39	0.2	7.1	10.5	2.7	293.97
$16_{17} \rightarrow 15_{16}$	688733.81	0.3	7.8	14.9	4.0	285.66
$17_{16} \rightarrow 16_{15}$	730500.26	0.3	7.2	7.5	2.2	322.2

SO₂

Transition $N_{K_a K_c}$	Frequency MHz	T_A (K)	V_{lsr} (km s ⁻¹)	V_{FWHM} (km s ⁻¹)	$\int T_A dV$ (K km s ⁻¹)	E_u (K)
$13_{3,11} \rightarrow 12_{2,10}$	484270.75	0.2	7.1	4.0	0.6	105.83
$7_{4,4} \rightarrow 6_{3,3}$	491933.52	0.1	7.7	5.4	0.8	65.01
$12_{3,9} \rightarrow 11_{2,10}$	494779.07	0.2	7.4	3.3	0.7	93.96

Superscript "b" means it is a blended line and excluded.

Table 5
LTE modeling results for species requiring one component fits

	$N \text{ (cm}^{-2}\text{)}$	$T_{\text{ex}} \text{ (K)}$	$V_{\text{FWHM}} \text{ (km s}^{-1}\text{)}$	$\Omega \text{ (}^{\circ}\text{)}$	$V_{\text{lsr}} \text{ (km s}^{-1}\text{)}$
[CI]	$1.0 \pm 0.2 \times 10^{18}$	48.3 ± 8.8	4.2	64.9 ± 14.7	7.8
[CII]	$1.4 \text{ to } 1.9 \times 10^{18}$	200.0 to 500.0	4.3	90.0	8.4
CCH	$8.9 \pm 2.1 \times 10^{14}$	36.5 ± 5.9	4.1 ± 0.1	65.7 ± 12.1	7.2 ± 0.0
CH	$1.8 \pm 0.4 \times 10^{14}$	37.7 ± 15.2	4.2 ± 0.3	69.8 ± 8.1	8.0 ± 0.0
CH ⁺	$2.9 \text{ to } 4.2 \times 10^{13}$	30.0 to 300.0	4.6	90.0	8.0
CN	$2.6 \pm 1.3 \times 10^{14}$	29.1 ± 3.9	4.3 ± 0.1	67.6 ± 7.8	7.6
¹³ CO	$1.4 \pm 0.4 \times 10^{17}$	88.8 ± 14.4	4.2 ± 0.7	79.6 ± 7.8	7.1
C ¹⁸ O	$3.5 \pm 0.5 \times 10^{16}$	61.9 ± 1.6	3.9 ± 0.0	69.3 ± 13.3	7.1
C ¹⁷ O	$1.4 \pm 0.4 \times 10^{16}$	53.3 ± 1.9	3.6	64.7 ± 19.9	7.2 ± 0.0
¹³ C ¹⁸ O	$8.1 \pm 1.6 \times 10^{14}$	54.3 ± 1.3	4.5	62.6 ± 12.0	7.1
DCN	$4.9 \pm 1.9 \times 10^{12}$	38.1 ± 5.4	6.1 ± 0.2	60.4 ± 15.4	7.0
DCO ⁺	$2.4 \pm 1.3 \times 10^{12}$	39.9 ± 2.3	3.0 ± 0.1	54.0 ± 15.3	6.7
H ₂ CS	$6.2 \pm 0.7 \times 10^{13}$	85.0 ± 2.8	4.5	68.0 ± 11.0	6.7
HCl	$1.6 \pm 0.6 \times 10^{14}$	32.2 ± 5.5	3.9 ± 0.1	52.5 ± 24.1	7.4
H ³⁷ Cl	$6.7 \pm 3.4 \times 10^{13}$	52.5 ± 15.6	3.7	53.3 ± 27.1	7.6
HNC	$2.4 \pm 0.3 \times 10^{13}$	28.2 ± 1.1	4.3 ± 0.1	67.2 ± 3.0	7.3
H ¹³ CO ⁺	$7.1 \pm 1.8 \times 10^{12}$	39.7 ± 1.3	3.8 ± 0.0	58.6 ± 14.4	7.0
N ₂ H ⁺	$1.6 \pm 0.5 \times 10^{13}$	46.6 ± 1.9	2.6 ± 0.0	57.9 ± 17.2	6.3
NO	$0.3 \text{ to } 1.1 \times 10^{16}$	20.0 to 200.0	5.8	90.0	7.2
SO ₂	$1.5 \pm 0.1 \times 10^{14}$	141.3 ± 8.4	6.7 ± 0.1	64.9 ± 9.6	7.5

Table 6

LTE modeling results for species requiring two component fits

	N_1 (cm $^{-2}$)	T_{ex1} (K)	Narrow Component				Broad Component				V_{lsr2} (km s $^{-1}$)
			V_{FWHM1} (km s $^{-1}$)	$\Omega_1(^{\circ})$	V_{lsr1} (km s $^{-1}$)	N_2 (cm $^{-2}$)	T_{ex2} (K)	V_{FWHM2} (km s $^{-1}$)	$\Omega_2(^{\circ})$		
CS	$6.5 \pm 1.9 \times 10^{14}$	36.5 ± 1.5	4.1	66.8 ± 10.8	7.2	$7.3 \pm 1.4 \times 10^{13}$	108.3 ± 2.4	9.5 ± 0.5	34.5 ± 8.2	7.0	
$^{13}\text{CS}^a$	$1.4 \pm 0.3 \times 10^{13}$	36.5	4.1	74.0 ± 13.6	7.2	$1.6 \pm 0.2 \times 10^{12}$	109.6 ± 1.3	9.5	34.5	7.0	
C^{34}S^a	$4.5 \pm 0.7 \times 10^{13}$	34.5	4.1	60.5 ± 8.9	7.2	$3.9 \pm 0.2 \times 10^{12}$	111.5 ± 3.5	9.5	34.5	7.0	
o-H $_2$ S	$1.0 \pm 0.2 \times 10^{15}$	24.5 ± 0.7	3.6	66.1 ± 14.1	7.0	$1.3 \pm 0.2 \times 10^{14}$	85.8 ± 18.3	8.8 ± 1.2	39.9 ± 8.1	7.2	
p-H $_2$ S	$9.4 \pm 1.5 \times 10^{14}$	24.3 ± 1.1	3.6	65.4 ± 13.5	7.0	$1.5 \pm 0.2 \times 10^{14}$	74.7 ± 9.9	7.4 ± 1.1	52.5 ± 10.5	7.1 ± 0.1	
$\text{H}_2^{34}\text{S}^a$	$3.2 \pm 0.6 \times 10^{13}$	25.1 ± 0.5	3.6	51.7 ± 7.7	7.0	$3.0 \pm 0.7 \times 10^{12}$	94.0 ± 15.1	9.0 ± 0.7	48.6 ± 10.0	7.2	
o-H $_2$ CO	$1.5 \pm 0.2 \times 10^{14}$	47.7 ± 4.3	4.0	69.3 ± 7.2	6.7	$3.8 \pm 0.6 \times 10^{13}$	153.6 ± 15.0	9.0 ± 0.3	47.7 ± 10.0	7.2 ± 0.2	
p-H $_2$ CO	$2.0 \pm 0.4 \times 10^{14}$	44.8 ± 3.0	4.0 ± 0.1	75.2 ± 10.7	6.7	$6.7 \pm 1.6 \times 10^{13}$	163.0 ± 27.2	9.0 ± 1.0	46.0 ± 9.3	7.3 ± 0.2	
HCN	$2.2 \pm 0.4 \times 10^{14}$	34.3 ± 5.0	4.4	64.4 ± 6.5	7.2	$4.8 \pm 0.1 \times 10^{13}$	66.8 ± 5.2	13.4 ± 0.6	41.1 ± 6.2	6.6 ± 0.1	
H^{13}CN	$5.1 \pm 0.7 \times 10^{12}$	30.5 ± 1.2	4.4	74.8 ± 7.4	7.2	$3.6 \pm 1.9 \times 10^{12}$	79.1 ± 7.8	11.0 ± 0.4	37.0 ± 10.8	6.6	
HCO^+	$7.7 \pm 0.7 \times 10^{13}$	68.9 ± 1.8	4.3	74.8 ± 8.2	7.0	$1.5 \pm 0.4 \times 10^{13}$	69.5 ± 4.9	12.0 ± 0.8	40.1 ± 12.1	7.1 ± 0.1	
NH_3 p & o	$1.4 \pm 0.3 \times 10^{14}$	20.0	4.2	80.3 ± 5.0	7.0	$8.4 \pm 5.4 \times 10^{13}$	35.8 ± 2.4	10.0	34.9 ± 11.2	7.2	
SO	$1.0 \pm 0.4 \times 10^{15}$	33.7 ± 5.0	3.8 ± 0.5	60.2 ± 17.8	6.8 ± 0.2	$2.1 \pm 1.1 \times 10^{14}$	121.8 ± 13.6	10.7 ± 0.5	34.8 ± 8.9	7.2 ± 0.3	

^a Calculation based on the main isotopologue

Table 7
The abundance of species with respect to H₂

Species	Narrow comp wrt H ₂	Broad comp wrt H ₂	Abundance enhancement factor
CCH	4.32×10^{-9}		
CN	1.26×10^{-9}		
C ¹⁷ O	6.80×10^{-8}		
¹³ C ¹⁸ O	3.93×10^{-9}		
DCN	2.38×10^{-11}		
HCl	7.77×10^{-10}		
H ³⁷ Cl	3.25×10^{-10}		
HNC	1.17×10^{-10}		
NO	3.40×10^{-8}		
H ¹³ CO ⁺	3.45×10^{-11}		
H ₂ CS	3.01×10^{-10}		
SO ₂	7.29×10^{-10}		
H ₂ S	9.42×10^{-9}	3.29×10^{-7}	35
H ₂ ³⁴ S	1.46×10^{-10}	3.41×10^{-9}	23
SO	4.86×10^{-9}	2.47×10^{-7}	51
¹³ CS	6.80×10^{-11}	1.88×10^{-9}	28
C ³⁴ S	2.19×10^{-10}	4.59×10^{-9}	21
NH ₃	6.80×10^{-10}	9.88×10^{-8}	145
H ₂ CO	1.70×10^{-9}	1.24×10^{-7}	73

Table 8
Column density upper limit for species in Orion-KL not detected in Orion-S

Species	$N_t, T_{ex}=40K$	$N_t, T_{ex}=80K$	E_u
$^{15}\text{NH}_3$	7.0×10^{11}	3.0×10^{12}	700
^{29}SiO	2.0×10^{12}	1.0×10^{12}	700
^{30}SiO	3.0×10^{12}	2.0×10^{12}	300
$\text{C}_2\text{H}_3\text{CN}$	N/A	N/A	300
$\text{C}_2\text{H}_5\text{CN}$	N/A	N/A	
$\text{C}_2\text{H}_5\text{OH}$	N/A	N/A	
C^{33}S	6.0×10^{12}	4.0×10^{12}	700
CH_2DOH	6.0×10^{13}	6.0×10^{13}	300
CH_2NH	7.0×10^{12}	2.0×10^{13}	300
$\text{CH}_3^{13}\text{CN}$	3.0×10^{14}	2.0×10^{13}	700
CH_3CN	7.0×10^{14}	5.0×10^{13}	700
$\text{CH}_3\text{CN}, v_8 = 1$	N/A		700
$^{13}\text{CH}_3\text{CN}$	4.0×10^{14}	2.0×10^{13}	700
CH_3OCHO	2.0×10^{15}	2.0×10^{15}	300
CH_3OD	N/A	N/A	700
$^{13}\text{CH}_3\text{OH}$	N/A	N/A	300
D_2O	5.0×10^{11}	2.0×10^{12}	300
H_2^{13}CO	1.5×10^{15}	1.5×10^{14}	700
H_2^{17}O	5.0×10^{11}	1.5×10^{12}	300
H_2CCO	1.5×10^{15}	2.0×10^{14}	700
$\text{H}_2\text{O}, v_2$	N/A	N/A	700
$\text{H}^{13}\text{CN}, v_2 = 1$	N/A	N/A	700
HC_3N	2.0×10^{17}	5.0×10^{14}	700
$\text{HC}_3\text{N}, v=0$	4.0×10^{17}	6.0×10^{14}	700
$\text{HCN}, v_2 = 1$	N/A	N/A	700
$\text{HCN}, v_2 = 2$	N/A	N/A	700
HD^{18}O	5.0×10^{11}	3.0×10^{12}	300
HDCO	7.0×10^{12}	9.0×10^{12}	300
HN^{13}C	8.0×10^{11}	1.0×10^{12}	300
HN^{13}CO	5.0×10^{12}	1.0×10^{13}	300
$\text{HNC}, v_2 = 1$	N/A	N/A	700
HNCO	5.0×10^{12}	1.0×10^{13}	300
NH_2CHO	3.0×10^{13}	3.0×10^{13}	700
NH_2D	4.0×10^{12}	8.0×10^{12}	300

Species	$N_l, T_{ex}=40K$	$N_l, T_{ex}=80K$	E_u
NH ₃ , v ₂	N/A	N/A	700
NS	1.5×10^{13}	1.0×10^{13}	300
O ₂	2.0×10^{17}	4.0×10^{17}	700
OCS	3.0×10^{17}	3.0×10^{15}	700
OD	1.0×10^{14}	1.5×10^{13}	700
OH	3.0×10^{15}	1.5×10^{14}	300
SiS	9.0×10^{14}	6.0×10^{13}	700
SO ₂ , v ₂ = 2	N/A	N/A	700
³³ SO	3.0×10^{13}	1.5×10^{13}	700
³⁴ SO	5.0×10^{13}	2.0×10^{13}	300
³³ SO ₂	2.0×10^{13}	4.0×10^{13}	300
³⁴ SO ₂	1.5×10^{13}	3.0×10^{13}	200

Table 9
Column density upper limit for unmodeled species in Orion-S

Species	$N_t, T_{ex}=40K$	$N_t, T_{ex}=80K$
CH_3OCH_3	1.5×10^{14}	3×10^{14}
CO^+	2×10^{12}	1.5×10^{12}
$H_2^{18}O$	2×10^{12}	3×10^{12}
$HC^{15}N$	1×10^{12}	2×10^{12}
HCS^+	2.5×10^{13}	1×10^{13}
NH_2	7×10^{12}	1×10^{13}
SH^+	4×10^{12}	7×10^{12}
SiO	1×10^{13}	4×10^{12}